Design and Synthesis of Novel Organic Probes towards Early-Stage Detection of Amyloid Fibrils & Their Mechanistic Role in Protein Misfolding Disease

A Thesis

Submitted in Partial Fulfillment of the

Requirements for the Degree of

Doctor of Philosophy

by

Aslam Uddin

Reg. ID: 20173509

Indian Institute of Science Education and Research (IISER), Pune

2023

Indian Institute of Science Education and Research (IISER), Pune

Certificate

It is hereby certified that the work described in this thesis entitled *"Design and Synthesis of Novel Organic Probes towards Early-Stage Detection of Amyloid Fibrils & Their Mechanistic Role in Protein Misfolding Disease"* submitted by *Mr. Aslam Uddin* was carried out by the candidate, under my supervision. The work presented here or any part of it has not been included in any other thesis submitted previously for the award of any degree or diploma from any other university or institution.

Partha Hazra

Date: 28th April, 2023

Prof. Partha Hazra
Research Supervisor
Email: p.hazra@iiserpune.ac.in
Contact No.: +91(20)25908077

Declaration

I declare that this written submission represents my ideas in my own words and wherever other's ideas have been included; I have adequately cited and referencedthe original sources. I also declare that I have adhered to all principles of academichonesty and integrity and have not misrepresented or fabricated or falsified any idea/ data/ fact/ source in my submission. I understand that violation of the abovewill cause for disciplinary action by the Institute and can also evoke penal action from the sources which have thus not been properly cited or from whom proper permission has not been taken when needed.

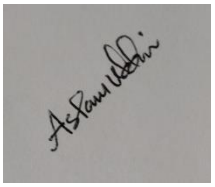

Date: 28th April, 2023

Aslam Uddin
Reg. Id 20173509

Table of Content

List of Abbreviations

CD	Circular Dichroism
DCM	Dichloromethane
DLS	Dynamic Light Scattering
min	Minutes
μM	Micromolar
mM	Millimolar
TCSPC	Time-correlated Single Photon Counting
ns	Nanosecond
ps	Picosecond
RTIL	Room Temperature Ionic Liquid
PB	Phosphate Buffer
UV	Ultraviolet
FE-SEM	Field Emission Scanning Electron Microscopy
TEM	Transmission electron microscopy
NMR	Nuclear Magnetic Resonance
RMSD	Root Mean Square Deviation

Synopsis

The main motivation of all the works containing in the thesis is design and synthesis of novel organic molecules for early-stage detection of amyloid fibrils and their mechanistic role in protein misfolding disease, such as Alzheimer's, Parkinson's disease and prion's disease. The early-stage species generated in the pathway of aggregation of Aβ-42 and α-synuclein known as main culprits for several neurological disorder, therefore systematic efforts at devising new fluorescent molecular probes and drug molecules are indispensable to estimate and modulate the mechanism of its formation.

Chapter 1. Introduction

In this chapter, we will give a brief introduction about the field which contains the information about some remarkable work that has been done in this field starting from the first observation of amyloid deposits nearly four centuries ago which is further culminated into the first atomic structures of the amyloid fibrils. And the predicament of the field in order to introspect what are the things are necessary to overcome the drawbacks. Ever since, abnormal aggregation of amyloidogenic proteins (like, Aβ42, amylin, α-synuclein, insulin) and deposition of these aggregates are believed to be associated with the several diseases known as amyloidosis. The pathway of aggregation involves three distinct phases, such as, oligomeric, elongation followed by plateau phase. Among them, the oligomeric phase of Aβ 42 and α-synuclein is involved in the generation of transient oligomeric species suspected for several neurological disorders including Alzheimer's, Parkinson's diseases. The aggregation process of proteins is associated with highly complicated interactive transient species. Over the past decade has seen great progress in the development techniques such as positron emission tomography (PET), single photon emission computed tomography (SPECT) and magnetic resonance imaging (MRI) for non-invasive detection of amyloid. But most of these techniques are expensive. Moreover, some of the techniques involve complicated data analysis and exposure to radioactivity. Recently, fluorescence-based techniques emerged as an efficient technique to understand the mechanism of its formation, and gained radical information about the possible therapeutics' routes of amyloidosis. Therefore, in the past few years, scientists have devoted much more efforts at devising new fluorescent molecular probes to estimate the mechanism of its formation, and gained radical information about the possible therapeutics' routes of amyloidosis. But such fluorescence probes face serious limitations because of self-quenching at high concentration of the probe; therefore, inappropriate for quantitative analysis and bio-imaging experiments. Hence, the smart biocompatible fluorescent probes are indispensable, which can overcome the drawbacks of conventional fluorescence probes. Additionally, establishing a potent scheme against aggregation of protein involved in several neurological disorders has been evaluated as a promising route to identify compounds that promote the aggregation process of protein. In the last two decades, this

perspective has guided a dramatic increase in the efforts, focused on developing potent drugs either for retardation or promotion of the self-assembly process of proteins.

Chapter 2. Sensing and Modulation of Amyloid fibrils by Photo-switchable Organic Dots

In this chapter, we have focused on developing promising photo switchable aggregation-induced emission (AIE) dots (DPAPMI, CPMI) and aggregation caused quenching (ACQ) dots (DMAPMI) based probes which can detect amyloid fibrils in terms of switching and enhancing its fluorescence emission. Overall, these organic dots enhance the aggregation rate of insulin by speeding up the microscopic processes, specifically, the secondary nucleation (with rate constant k_2) and the elongation process (with rate constant k_+). Moreover, the comparison of kinetic studies with ThT suggests that our organic dots can sense pre-fibrillar aggregates of insulin during aggregation process, which may be beneficial for early-stage detection of amyloid fibril. In summary, our study defines that these organic dots have quality for smart detection of amyloid fibrils which can overcome the drawbacks arising from conventional probes followed by detection of early pathways of aggregation and modulation of amyloid fibrils.

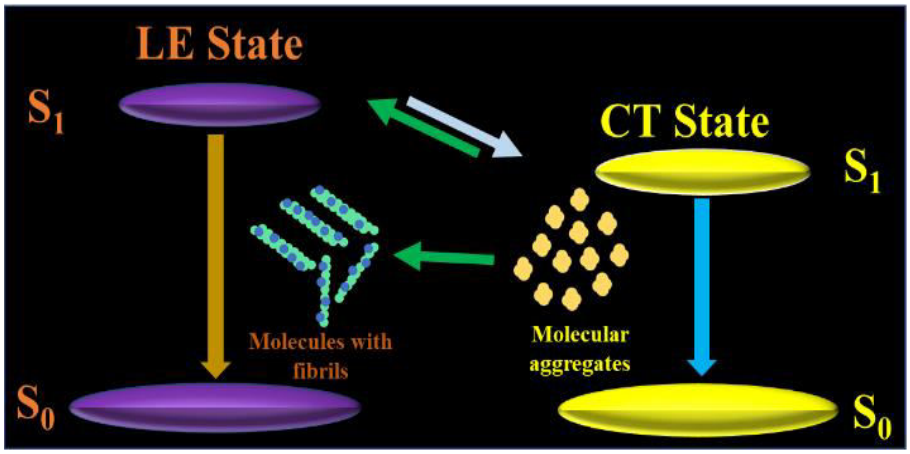

Chapter 3. Early-stage detection of α-synuclein aggregation using curcumin-based probe

Deposition of α-synuclein aggregates with characteristic of cross-β amyloid structure in dopaminergic neurons of substantia nigra of the midbrain known as a main culprit for Parkinson's disease. Recent past, diverse study suggesting that small soluble oligomeric intermediates, appear during the pathway of aggregation claimed to be toxic for neuronal cell death. From last two decades people have developed different kind fluorescent probes in order to detect α-synuclein aggregates but unfortunately most of the probes are insensitive towards soluble oligomeric intermediates. Therefore, improved fluorescent probe is urgently required for early-stage detection

of α-synuclein. In continuation of this efforts, we have synthesized curcumin-based derivative which have the potential to detect the oligomeric phase of alpha-synuclein.

Chapter 4. Development of a Systematic Strategy towards Promotion of α-Synuclein Aggregation Using 2-Hydroxyisophthalamide-Based Systems

In this chapter we focused on establishing a potent scheme against a-synuclein aggregation involved in Parkinson's disease has been evaluated as a promising route to identify compounds that either inhibit or promotes the aggregation process of a-synuclein. In the last two decades, this perspective has guided a dramatic increase in the efforts, focused on developing potent drugs either for retardation or promotion of the self-assembly process of α-synuclein. To address this issue, by using a chemical kinetics platform, we developed a strategy that enabled a progressively detailed analysis of the molecular events leading to protein aggregation at a microscopic level in the presence of recently synthesized 2-hydroxyisophthalamide class of small organic molecules based on their binding affinity. Furthermore, qualitatively we have developed a strategy of disintegration of a-synuclein fibrils in the presence of these organic molecules. Finally, we have shown that these organic molecules effectively suppress the toxicity of α-synuclein oligomers in neuron cells.

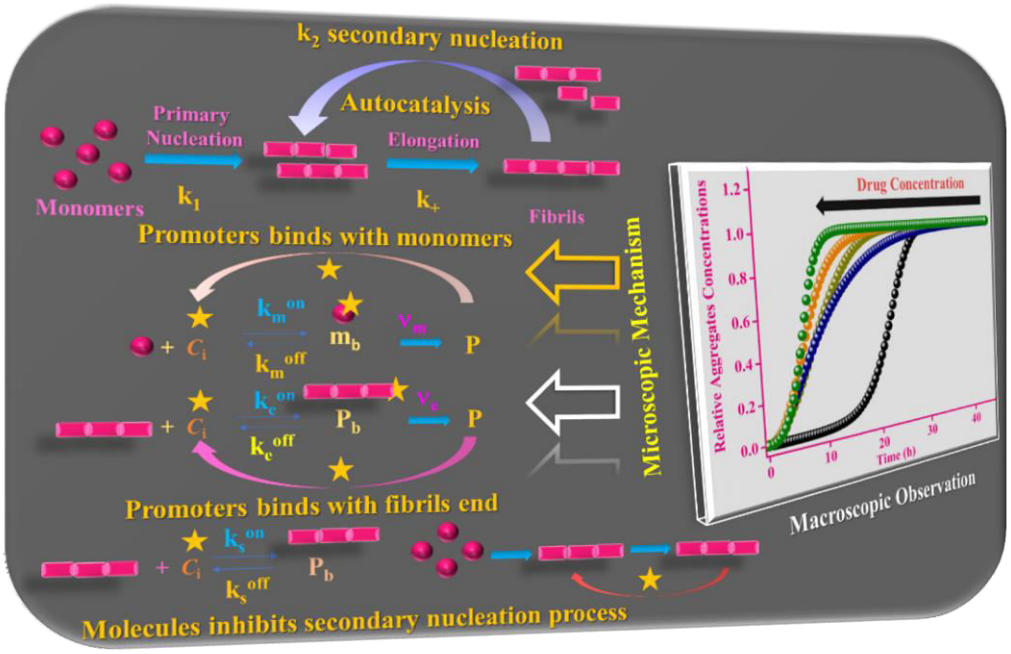

List of Publications

1. **Aslam Uddin.**; Roy, B.; Jose, G. P.; Hossain, S. S.; Hazra, P., Sensing and modulation of amyloid fibrils by photo-switchable organic dots. *Nanoscale* **2020,** *12* (32), 16805-16818.

2.**Aslam Uddin;** Javid Malla; Harish Kumar; Manisha Kumari; Suman Sinha; Virender Kumar Sharma; Yashwant Kumar; Pinaki Talukdar; Mayurika Lahiri; Tushar Kanti Maiti; Partha Hazra; Development of a systematic strategy towards promotion of α-synuclein aggregation Using 2- hydroxyisophthalamide-based systems. *Biochemistry* **2022,** *61* (21), 2267-2279.

Right and Permission

Figure 1.1 Reproduced with permission from *Nature Reviews Molecular Cell Biology*,2018, **19**, 755–773: Copyright 2018: Springer Nature Limited.

Figure 1.5 Reproduced with permission from *Proceedings of the National Academy of Sciences* **2020,** *117* (39), 24251-24257.

Chapter 1

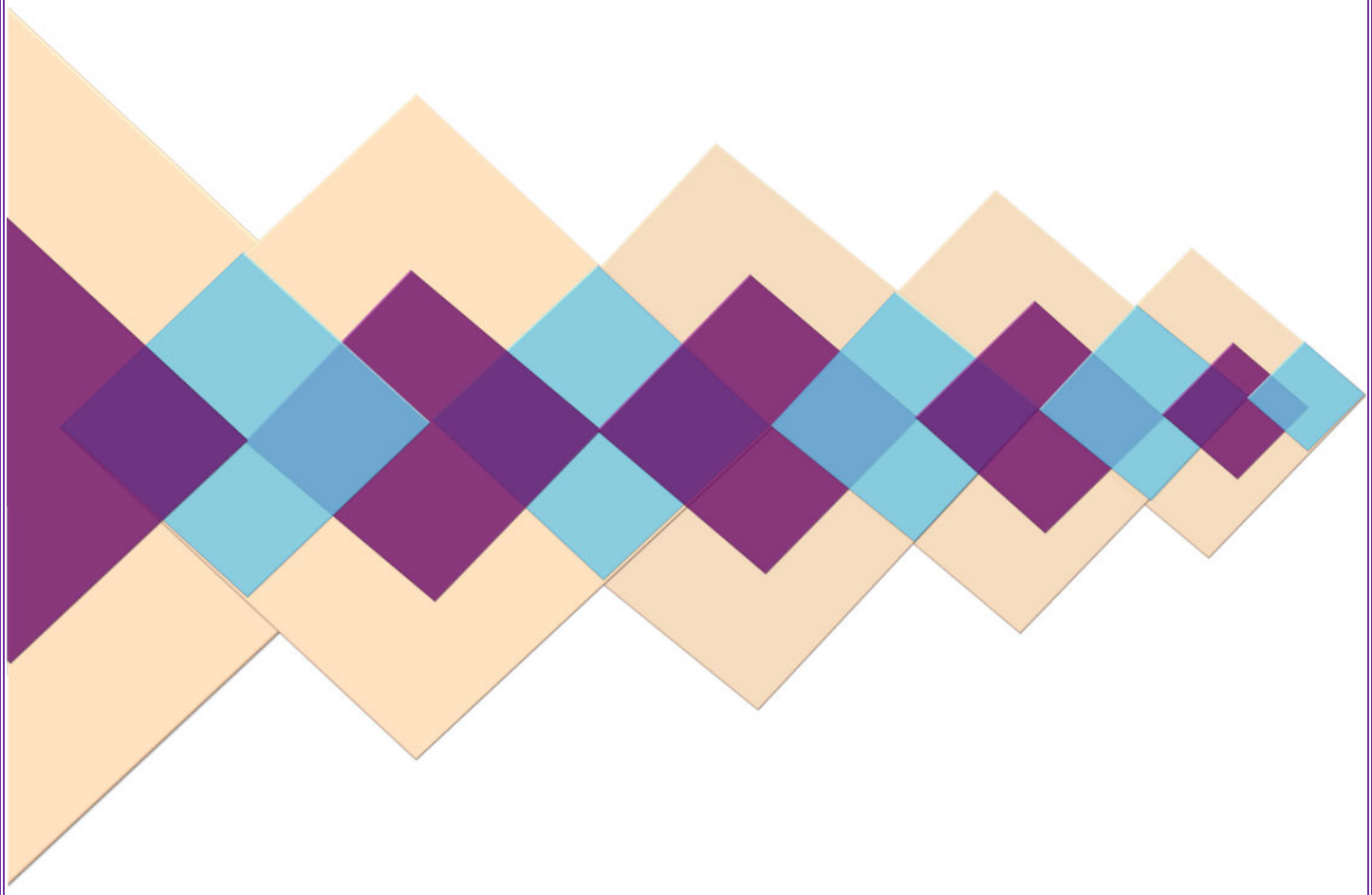

History of Amyloid

History of Amyloid

1.1 Introduction

Deposition into amyloid plaques leading from misfolding of amyloidogenic protein is the hallmark of amyloid disease[1-5]. This abnormal deposition of the amyloid fibrils, known as the leading cause of amyloidosis which is linked with many chronic disease that can be related with aging, such as Alzheimer's disease, Parkinson's disease, Type II diabetes etc[1]. Therefore, from the first discovery of amyloid deposits happened nearly four centuries ago that motivated scientists to devote their attention to understanding the problems[6]. However, in the last two years fibril's structure have been set on in near atomic details because of some remarkable methods to creates fibrils in-vitro as well as breakthroughs in (Cryo-EM) and solid-state N.M.R spectroscopy (ss N.M.R). There are almost around 50 different proteins or peptides prone to self-assembly into amyloid fibrils associated with human disease[7]. These precursors with a distinct primary sequences are known to self-assemble into amyloid fibrils that accumulate into extracellular plaques and intracellular inclusions associated with disease[8-9]. Emerging evidence has been shown that intracellular incorporation of amyloid with cellular physiology, such as disrupting transport of proteins and RNA[10] and by sequestering chaperones and proteasomes[11]. Plaques from different phenotypic forms of the same disease can also accumulate different proteins[12] and non-protein components[13-14] to varying extents, potentially providing clues to the different phenotypes observed within an amyloid disease. Sharing a common underlying architecture is the trademark of amyloid fibrils, where the β-strands within each protofilament align perpendicularly to the long axis of the fibril, termed as a cross-β amyloid fold decided by characteristic around 4.7-4.8 Å repeat running down the fibril axis[15], which possesses an extraordinary strength[16]. Here we will discuss the history containing the information about understanding of the amyloid fold and the discussion of the amyloid fibril structure, motivated by recent literature reports of the fibrils of proteins which are associated with human disease. We will also discuss the type of disease associated with this fibril and their effect on modern civilization and the predicament of the field to introspect the things which are important to do.

History of Amyloid

1.2 History of Amyloid

It was 17th century where amyloid was first described as lardaceous liver and white stone-containing spleen[6], the term amyloid derived from amylum and amylon (Latin and Greeks words for starch), respectively, and coined ~200 years later by Virchow on the basis of his discovery that these deposits stained positively with iodine[6, 17]. After 5 years Kekule discovered that this plaque is predominantly protein based with carbohydrates, being ubiquitously associated with these deposits[18]. In the discovery of light microscopy, integrated with the finding that amyloid deposits exhibit the unique tinctorial property of red-green birefringence in the presence of Congo red 35 which revealed that amyloid is formed from highly organized protein subunits[19]. Concurrently, the development of X-ray fibre diffraction studies showed that amyloid fibrils could be the outcome of normally globular, soluble proteins by denaturing them in vitro[20] leading to synthetic materials that could replace wool[40.] In 1968 Sandy Geddes, Bill Aiken and their colleagues revealed the egg stalk of the lacewing fly by using X-ray fibre has a distinct ~ 4.7 Å repeating features down the fibril's axis, which they named cross-β[21]. This innovative work established a structural fingerprint for amyloid which exhibits that amyloid is not simply associated with disease but can also perform physiological functions in an organism[22-25].

History of Amyloid

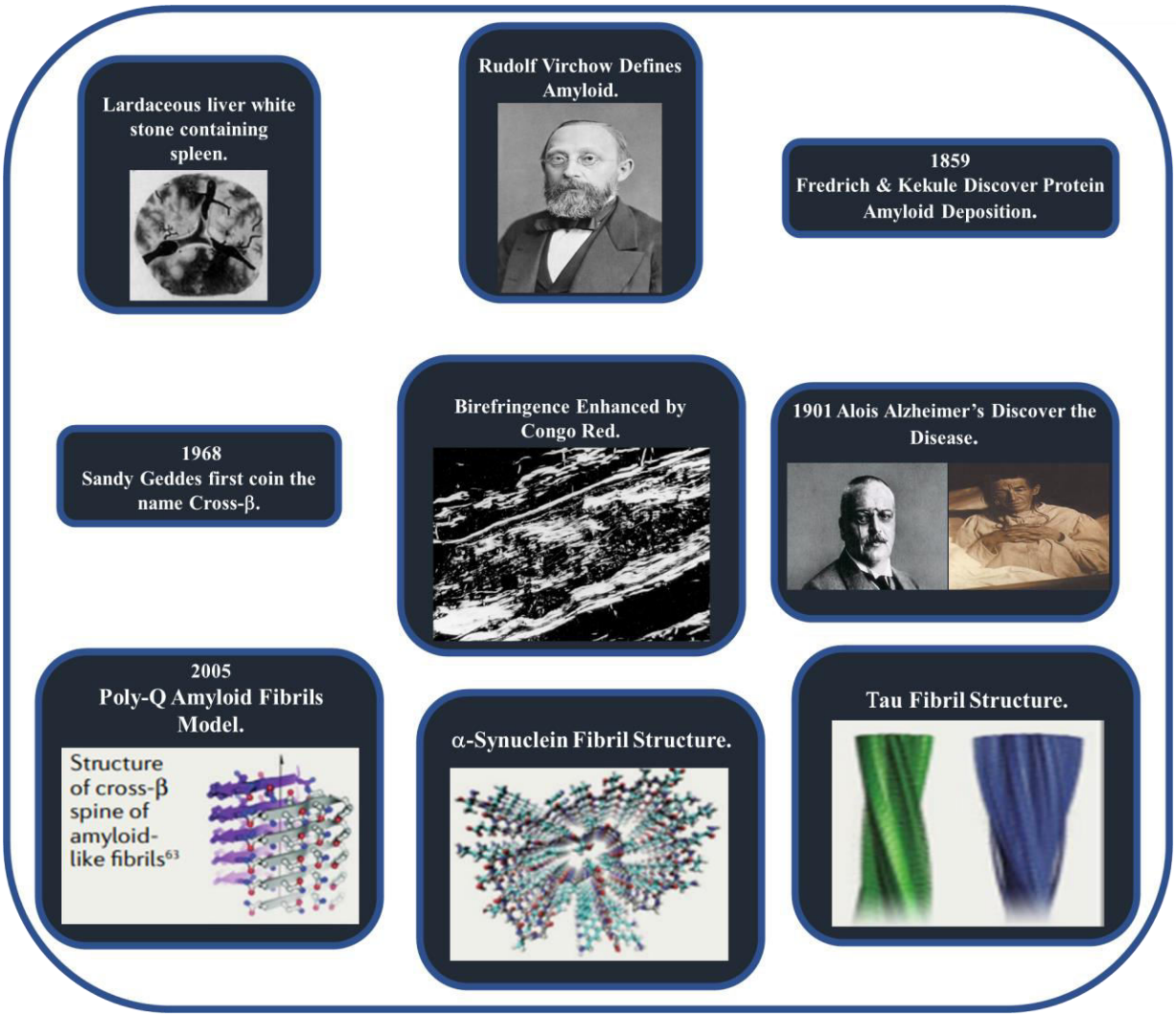

Figure 1.1. Progression of amyloid structures research over close to 400 years that has culminated in the first atomic structures of amyloid fibrils[22].

After 50 years since Geddes et al. named the termed cross-β[21], crucial information about the structure of amyloid fibrils has been watering the scientific world, with dazzling information coming from studies of fibrils formed form shorts peptides using X-Ray fibre diffraction[26], X-Ray crystallography[27-28] and ss-NMR[29-33], cry-ET[14, 34-35] and cryo-EM[36-39]. The excellent ability of self-assembly of synthetic peptides and naturally occurring amyloidogenic peptides, has sparked useful development of different techniques. The collective efforts of these techniques demystify the amyloid fold and assist us to visualize the beautiful structure formed by amyloidogenic proteins or peptides. These structures enlighten us about the motif of cross

−β structure, and combining these the data analysis from super resolution microscopy, cryo-electron tomography and ss-NMR creating an idealogue for integrative structural biology that allow us to see the structure of amyloid fibrils on multiple scales, from individual subunits and their arrangement of fibrils deposition driven by cellular consequence and deposit into plaque and tangles.

1.3 Disease Associated with Amyloid Fibrils Deposition

It was 1901 when Alois Alzheimer first reported the case of AD in his patient named Auguste Deter[40-41]. Since this work which included the post-mortem visualization of congo-red positive plaques in the brain, scientists have devoted their attention to find the possible route to cure the disease. Recently more than 50 diseases associated with amyloidogenic proteins have been identified, which leads to a greater number of diseases related to the sequence of the precursor and the site of amyloid deposition[2, 42]. These diseases included neurodegenerative disorders, involving the aggregation of Aβ[43] and Tau[44]. Apart this there many diseases involving in aggregation of protein such prion disease (PrP)[45], Huntington disease (huntingtin[46]), PD (α-synuclein[47]) and amyotrophic lateral sclerosis (ALS; superoxide dismutase (SOD), TAR DNA binding protein[48] (TDP 43), type II diabetes involves the aggregation of amylin (known as islet amyloid polypeptide (IAPP)[49]). Amyloid polypeptide in the islets of Langerhans; in AL amyloidosis, antibody light chains are deposited in the kidney and hearts[50] and in dialysis-related amyloidosis, β2 macroglobulin (b2m) associated with the amyloid plaques in the osteoarticular tissue[51]. There are also debates between amyloid diseases, such as patients with type II diabetes have higher risk of AD[52]. The non-amyloid component (NAC) of α-synuclein has been found in the patient with AD[53].

1.4 Types of Techniques

From the past decade scientist have come out with the progressive development about imaging probes for non-invasive detection of Aβ based on the role of Aβ accumulation in AD diagnosis, mainly relying on techniques such as positron emission tomography (PET)[54], single photon emission computed tomography (SPECT)[55] and magnetic resonance imaging (MRI)[56]. Particularly, various probes involved in PET have shown good efficacy for imaging Aβ in AD brains including florbetapir (18F) and flutemetamol[57]. But unfortunately, these probes are

highly costly[58], narrow isotope availability and short-lived isotopes of PET probes and the radioactivity of SPECT have confined it for clinical useability[59]. Recently most of the available PET imaging requires expensive instruments, highly skilled personnel, time-consuming data analysis and unavoidable radiation exposure[59]. Therefore, alternative technologies which are relatively cheaper and easy to handle have attracted burgeoning interest. Apart from these the optical imaging especially near-infrared fluorescence (NIRF) imaging is highly efficient compared to PET, SPECT and MRI because it is real-time, inexpensive, not radioactive and high resolution both in-vivo and ex-vivo[60]. Moreover, NIRF imaging instruments are relatively inexpensive compared to PET. Specifically NIRF probes are favorable for the detection of Aβ in-vivo because emission wavelengths in the NIR range (650-900 nm) are distinct from the autofluorescence of biological matter which is useful for in-vivo applications. Therefore, from the last two decades scientists have devoted their attention to developing Aβ fluorescent probes and use to detect Aβ in vitro and in vivo[61]. The current research about the technical developments indicates that the Aβ fluorescence imaging is an efficient technique which in future could be feasible and widely used for clinical purposes.

1.5 Positron Emission Tomography (PET)

Positron emission tomography (PET) is a technique specifically used to measure the metabolic activity of the cells of the body and tissues which is the combination of nuclear medicine and biochemical analysis.[62] Most of the time PET helps to visualize the biochemical process taking place in the body such as the metabolism (the process by which cells change food into energy). PET is a kind of nuclear medicine procedure that means that a very little amount of a radioactive substance, called a radiopharmaceutical, is used during the procedure to assist in the examination of the tissue under study.[63] PET is mostly used in conjunction with other diagnostic tests, such as computed tomography (CT) or magnetic resonance imaging (MRI) to provide more definitive information regarding cancerous tumors and other lesions[64].

The main principle of how PET functions is a scanning device (a machine with a large hole at its center) to detect photons emitted by radionuclide in the organ on tissue being examined[65]. Mostly the radionuclides used in PET scans are made by attaching a radioactive atom to chemical substances which are particular organs or tissue during its metabolic process[66].

Generally, PET scans are used for the detection of cancer and diagnose dementia conditions that involve deterioration of mental function[67].

1.6 Single Photon Emission Computed Tomography (SPECT)

Single photon emission computed tomography (SPECT) scan is an imaging technique that track the flows of a blood on tissue and organs.[68] It can be useful to diagnose seizures, stroke and infections and tumors in the spine[69]. The work principle of SPECT imaging is nuclear imaging scan that coupled with integrates computed tomography (CT) and a radioactive tracer. Initially the tracer is injected into the bloodstream which is radiolabeled meaning it emits gamma rays which can be detected by the CT scanner. The computer that collects the information by the gamma ray and displays it on the CT cross-sections which added bac together to form 3D image of your brain. Typically, the radioisotopes used in SPECT to labeled tracers are iodine-123, technetium-99 m, xenon -133, thallium-201 and fluorine-18. The principle of SPECT is slightly differed from a PET scan in that tracers stays in your blood stream rather than being absorbed by surrounding tissues. Moreover, SPECT is relatively cheaper and more readily available than higher resolution PET scan.

1.7 Magnetic Resonance Imaging (MRI)

Magnetic Resonance Imaging (MRI) is basically known as a non-invasive imaging technique which constructs three dimensional detailed anatomical images, frequently used for diagnosis, detection and treatment monitoring.[70] This technique is one of the sophisticated technologies of modern age which excites and detects the change in the direction of the rotational axis of protons found in the water that makes up living tissues. The working principle of MRIs employs powerful magnets which produce a strong magnetic field that forces protons in the body to align with the field. In the presence of radiofrequency pulsed the current is then pulsed through the patient and the protons are stimulated and spin out of equilibrium straining against the pull of magnetic field. But when the radio frequency pulse turnoff MRI sensor starts detecting the energy released by protons realigned with the magnetic field. The time-lapse between realignment with the magnetic field as well as the amount of energy released depend on the environment and the chemical nature of the molecules. MRI scanner is mostly used for imaging

the non-bony parts or soft tissue of the body whose working principle is slightly differ from computed tomography (CT), in that they are free from damaging ionizing radiation of x-rays.

1.8 Types of Fluorescent Probes

In continuation of these efforts people have developed different kinds of probes like charge transfer (CT)[71], molecular rotor[72] and aggregation induced emission (AIE) based probes[73]. The quality of charge transfer probes lies on the fact that quality it switches it fluorescence emission upon binding with amyloid fibrils, where molecular rotor-based probes enhanced it fluorescence emission upon binding with amyloid fibrils because of the restriction of intramolecular rotation inside the fibrillar grooves. But AIE based probes have a quality of detecting amyloid fibrils in terms of disaggregation induced fluorescence switching.

1.9 Molecular Rotor Based Probes

Molecular rotors are a smart class of fluorophores, specially categorized by their ability to undergo twisted intramolecular charge transfer (TICT).[74-75] The typical features of this class of probes basically consists of three parts: an electron-donating unit, an electron-accepting unit and a pi-conjugated linking moiety, which allows electron transfer to occur in the planar conformation. The strong electrostatic forces upon irradiation cause twisted conformation around the σ-bond in the linker region. This nonplanar arrangement leads to a lower excited energy which is associated with either a red-shifted fluorescence emission or can undergo a non-radiative torsional relaxation pathway depending on the molecular structure of the rotor.[76] This TICT property is highly sensitive to their environment. Because of this excellent quality of these probes (Figure 1.2) serving as a potential marker for amyloid detection since the last two decades.[77-79]

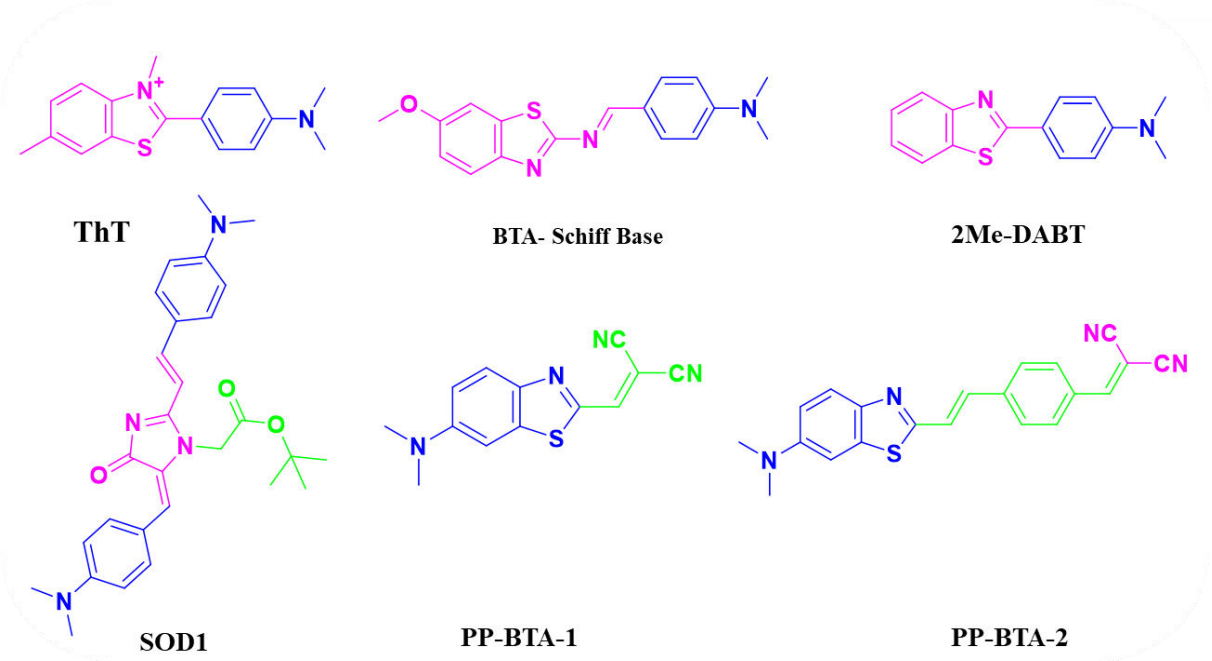

Figure 1. 2. Types of molecular rotor-based probes.[78]

1.10 AIE (Aggregation Induce Emission) Based Probes

AIE is a class of luminogens that are emissive as a molecular species but highly luminescent as aggregates. The name of this class of probes was first coined by Tang et al.in 2001.[80] The principal mechanism of AIE-active luminogen has been rationalized such a fashion that its exhibits no emission when it is molecularly dispersed, and become emissive when it forms aggregates because of restricted intramolecular motions including rotations, vibration through which it dissipates excited state energy by boosting the nonradiative decay.[81] Upon aggregation, the RIM (Restricted intra-molecular) process is getting activated by stopping the radiation less consumption of the excitation energy which populates the radiative decay channels. Because of this unique quality of this class of probes (Figure 1.3) made it an excellent marker for amyloid detections**.**

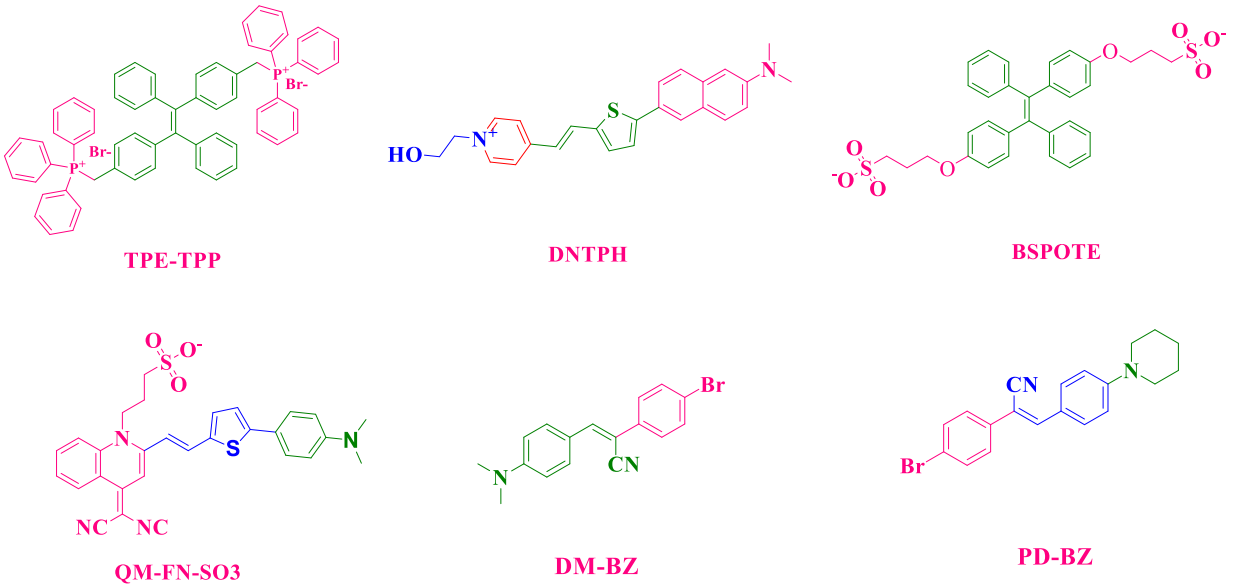

Figure 1.3. Aggregation induced emission-based probes.[73, 82-84]

1.11 ICT (Intramolecular Charge Transfer) Based Probes

Intramolecular charge transfer (ICT) is a class of fluorescent probes used for several technological applications, including organic light emitting diodes (OLEDs), dye-sensitized solar cells and nonlinear optical (NLO) materials.[85] In a D-A a donor to the accept or moiety through a pi-electron bridge, C-T takes place by a mechanism called through space charge transfer. In the case of π conjugated organic molecules made of electron donor (D) and acceptor (A) subunits, the process has attracted a burgeoning interest due to massive technological implications. Because of this extraordinary quality these kinds of probes emerged as a potential marker of amyloid.[73 82, 86]

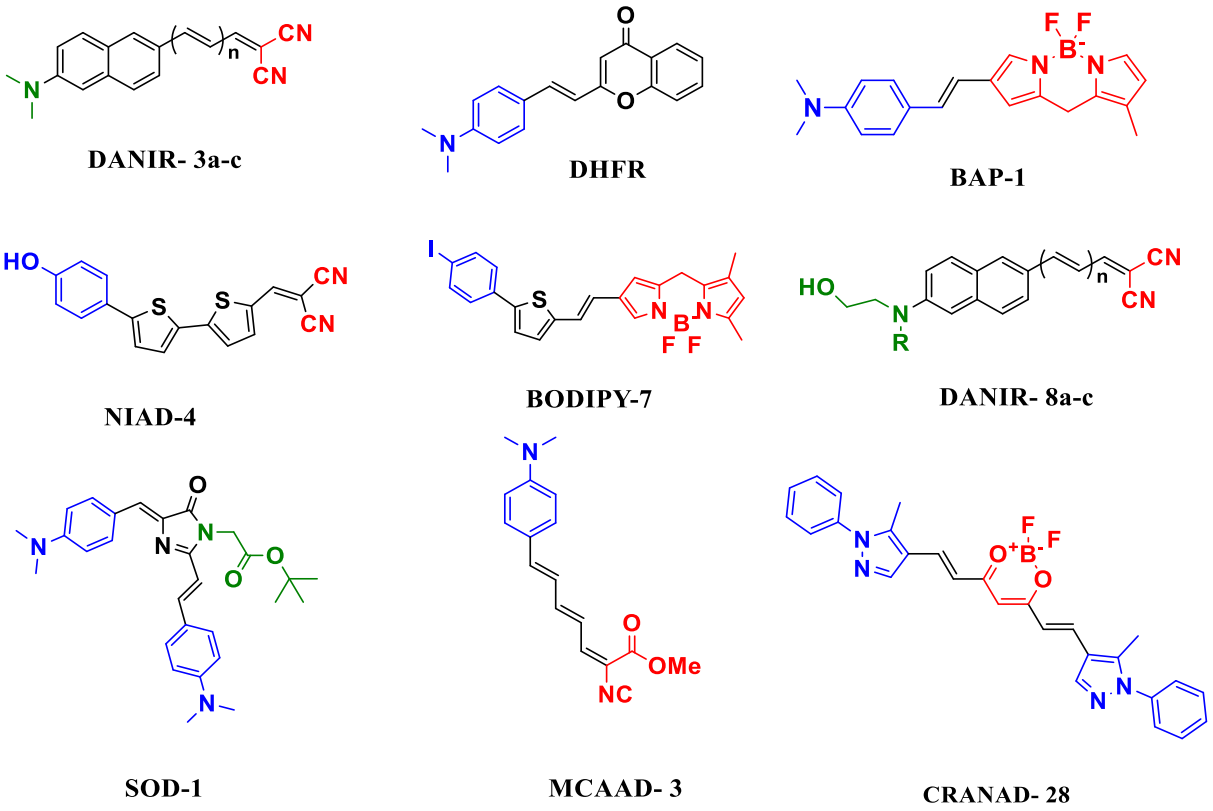

Figure 1.4. Intramolecular charge transfer probes[78, 87].

1.12 Mechanism of Protein Aggregation

The general process of amyloid fibrils formation is the aggregation of monomeric protein via common nucleation growth mechanism where monomeric precursor protein initially unfolded or partially folded.[88] Occasionally the native protein itself initiates the aggregation process. At first the assembly of fibrils lead to the formation of oligomers which are dynamic, transient heterogeneous and of unknown and possibly diverse structure. After that oligomers further associate to produce higher-order aggregates. These critical nucleus formed prior to the initiation of polymerization known as kinetically most unstable species and the probability of nucleate formation mostly determines the length of the lag time of amyloid assembly and the possible age of the disease.[89] During the course of self-assembly, the individual precursor undergoes a structural transformation to form β-sheet rich secondary structure.[38] Once the fibrils

form cross-β structure they can fragment to produce new fibril ends which recruit monomers, shortening the length of lag time and causing an exponential fibrils growth. Other processes like secondary nucleation in which the small oligomers catalyzed the pre-existing fibril and enhance the rate of fibril formation. Therefore, understanding the combined nature and estimate the rate of fibril assembly is vital for elucidation of fibril formation mechanisms both in vitro and in vivo environments. But because of the complexity associated with aggregation networks the analysis of aggregation kinetic data is a hectic job. Therefore, describing a framework using quantitative kinetic assays and global fitting to evaluate and support a molecular mechanism for aggregation reaction which is compatible with experimental kinetic data. Furthermore, misfolding of amyloidogenic peptides and proteins and its deposition into amyloid fibrils has a route in many phenomena, ranging from the functional machinery in biology to the production of novel nanomaterials. The main interest in this process has come from the perception–this protein-aggregation is directly connected to a range of human conditions from Alzheimer's disease to type 2 diabetes. Recently, inhibition and promotion of protein aggregation into amyloid fibrils thus represents a vital scheme for the development of efficient drugs against protein misfolding disease.

Generally, the inhibition strategies mainly concentrate either on blocking the production of aggregation or on disintegration of amyloid fibrils. However recent trials have instead focused on altering or delaying the aggregation process itself that solely achieved using compounds which bind noncovalently to different types of protein species during the course of aggregation for example small drug like molecules, molecular chaperons, antibodies and nanoparticles. Similarly, it was also found that the aggregation reaction is a complex nonlinear process where aggregating proteins can simultaneously act as the reactants, products and intermediates and catalyst of the reaction[90]. In Spite of this urgency, the fundamental physical principles controlling the regulation of protein aggregation into amyloid fibrils remain unclear. Specifically, it remains challenging to develop a quantitative relation between drug binding to different aggregating species and the resulting impact.

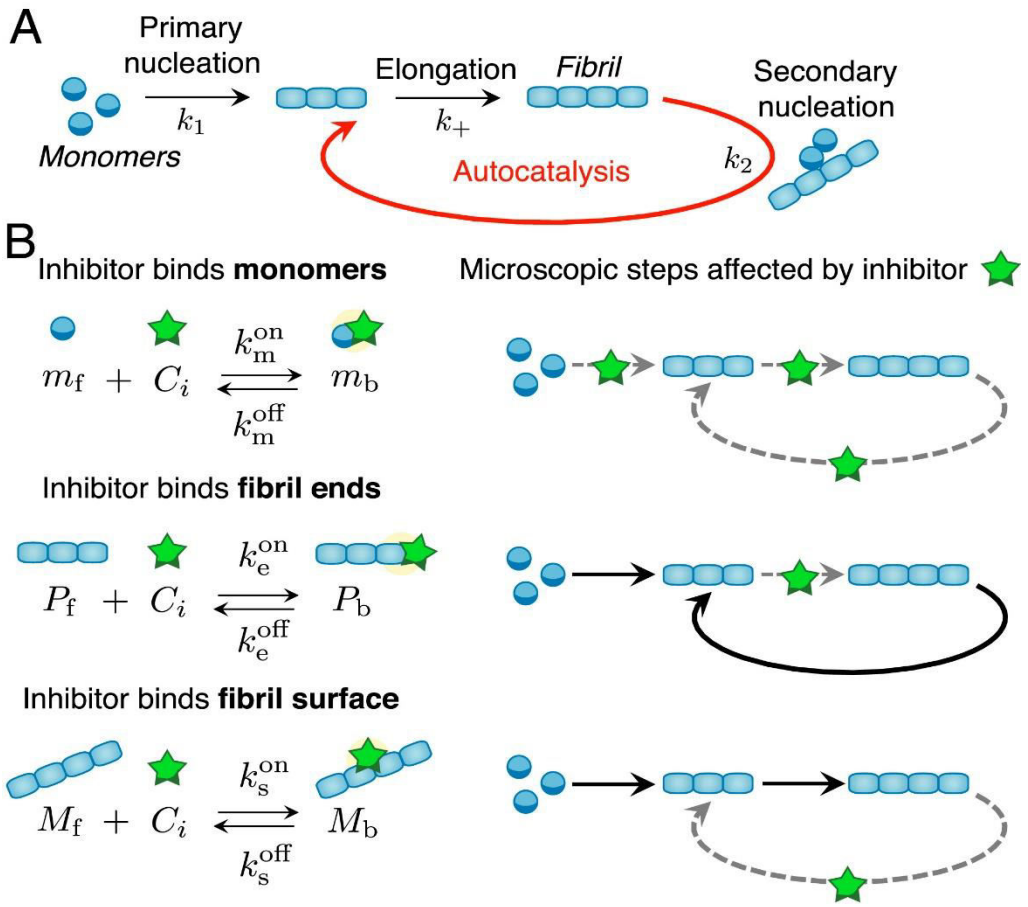

Figure 4. Microscopic mechanisms of protein aggregation and possible inhibition pathways. in the presence of drug molecules[90]. A) Schematic representation of the microscopic steps of protein aggregation into fibrils (B, Left) Potential target species during protein aggregation and associated binding rate. (B, Right) Schematic diagrams showing the microscopic steps that are targeted by the inhibitor.

1.13 Motivation of The Thesis

In the previous sections, we have extensively discussed the history of amyloid and the disease associated with it and the possible techniques scientists have developed to understand the process.

Where we observed the great progression in the development of the techniques to understand and combat the process such as positron emission tomography (PET), single photon emission computed tomography (SPECT) and magnetic resonance imaging (MRI) for non-invasive detection of amyloid. But most of these techniques are expensive. Moreover, some of the techniques involve complicated data analysis and exposure to radioactivity. Recently, fluorescence-based techniques emerged as an efficient technique to understand the mechanism of its formation, and gained radical information about the possible therapeutics' routes of amyloidosis. Therefore, in the past few years, scientists have devoted much more efforts at devising new fluorescent molecular probe stop estimate the mechanism of its formation, and gained radical information about the possible therapeutics' routes of amyloidosis. But such fluorescence probes face serious limitations because of self-quenching at high concentration of the probe; therefore, inappropriate for quantitative analysis and bio-imaging experiments. Hence, the smart biocompatible fluorescent probes are indispensable, which can overcome the drawbacks of conventional fluorescence probes. Additionally, establishing a potent scheme against aggregation of protein involved in several neurological disorders has been evaluated as a promising route to identify compounds that promote the aggregation process of protein. In the last two decades, this perspective has guided a dramatic increase in the efforts, focused on developing potent drugs either for retardation or promotion of the self-assembly process of proteins. In this thesis, we are going to focus on developing the systematic scheme on designing and synthesis of novel organic probes which can detect the aggregating species of proteins such as insulin and a-synuclein, and help us to gained radical information to develop the possible therapeutics routes of amyloidosis. Then, we are going to show a potent strategy against α-synuclein aggregation using newly design 2-hydroxyphthalimide-based systems that enabled a progressively detailed analysis of the molecular events leading to protein aggregation at a microscopic level followed by effective suppression of the toxicity of α-synuclein oligomers in neuron cells.

1.14 References

1. Hardy, J.; Selkoe, D. J., The Amyloid Hypothesis of Alzheimer's Disease: Progress and Problems on the Road to Therapeutics. *Science* **2002,** *297* (5580), 353-356.
2. Eisenberg, D.; Jucker, M., The Amyloid State of Proteins in Human Diseases. *Cell* **2012,** *148* (6), 1188-1203.

History of Amyloid

3. Ross, C. A.; Poirier, M. A., Protein aggregation and neurodegenerative disease. *Nature Medicine* **2004,** *10* (7), S10-S17.
4. Silveira, J. R.; Raymond, G. J.; Hughson, A. G.; Race, R. E.; Sim, V. L.; Hayes, S. F.; Caughey, B., The most infectious prion protein particles. *Nature* **2005,** *437* (7056), 257-261.
5. Montojo, M.; Aganzo, M.; González, N., Huntington's Disease and Diabetes: Chronological Sequence of its Association. *J Huntingtons Dis* **2017,** *6*, 179-188.
6. Sipe, J. D.; Cohen, A. S., Review: history of the amyloid fibril. *Journal of structural biology* **2000,** *130* (2-3), 88-98.
7. Sipe, J. D.; Benson, M. D.; Buxbaum, J. N.; Ikeda, S. I.; Merlini, G.; Saraiva, M. J.; Westermark, P., Amyloid fibril proteins and amyloidosis: chemical identification and clinical classification International Society of Amyloidosis 2016 Nomenclature Guidelines. *Amyloid : the international journal of experimental and clinical investigation : the official journal of the International Society of Amyloidosis* **2016,** *23* (4), 209-213.
8. Sloane, P. D.; Zimmerman, S.; Suchindran, C.; Reed, P.; Wang, L.; Boustani, M.; Sudha, S., The public health impact of Alzheimer's disease, 2000-2050: potential implication of treatment advances. *Annual review of public health* **2002,** *23*, 213-31.
9. Geula, C.; Wu, C. K.; Saroff, D.; Lorenzo, A.; Yuan, M.; Yankner, B. A., Aging renders the brain vulnerable to amyloid beta-protein neurotoxicity. *Nat Med* **1998,** *4* (7), 827-31.
10. Woerner, A. C.; Frottin, F.; Hornburg, D.; Feng, L. R.; Meissner, F.; Patra, M.; Tatzelt, J.; Mann, M.; Winklhofer, K. F.; Hartl, F. U.; Hipp, M. S., Cytoplasmic protein aggregates interfere with nucleocytoplasmic transport of protein and RNA. *Science* **2016,** *351* (6269), 173-6.
11. Guo, Q.; Lehmer, C.; Martínez-Sánchez, A.; Rudack, T.; Beck, F.; Hartmann, H.; Pérez-Berlanga, M.; Frottin, F.; Hipp, M. S.; Hartl, F. U.; Edbauer, D.; Baumeister, W.; Fernández-Busnadiego, R., In Situ Structure of Neuronal C9orf72 Poly-GA Aggregates Reveals Proteasome Recruitment. *Cell* **2018,** *172* (4), 696-705.e12.
12. Drummond, E.; Nayak, S.; Faustin, A.; Pires, G.; Hickman, R. A.; Askenazi, M.; Cohen, M.; Haldiman, T.; Kim, C.; Han, X.; Shao, Y.; Safar, J. G.; Ueberheide, B.; Wisniewski, T., Proteomic differences in amyloid plaques in rapidly progressive and sporadic Alzheimer's disease. *Acta neuropathologica* **2017,** *133* (6), 933-954.
13. Stewart, K. L.; Hughes, E.; Yates, E. A.; Akien, G. R.; Huang, T.-Y.; Lima, M. A.; Rudd, T. R.; Guerrini, M.; Hung, S.-C.; Radford, S. E.; Middleton, D. A., Atomic Details of the Interactions of Glycosaminoglycans with Amyloid-β Fibrils. *Journal of the American Chemical Society* **2016,** *138* (27), 8328-8331.
14. Kollmer, M.; Meinhardt, K.; Haupt, C.; Liberta, F.; Wulff, M.; Linder, J.; Handl, L.; Heinrich, L.; Loos, C.; Schmidt, M.; Syrovets, T.; Simmet, T.; Westermark, P.; Westermark, G. T.; Horn, U.; Schmidt, V.; Walther, P.; Fändrich, M., Electron tomography reveals the fibril structure and lipid interactions in amyloid deposits. *Proc Natl Acad Sci U S A* **2016,** *113* (20), 5604-9.
15. Smith, J. F.; Knowles, T. P. J.; Dobson, C. M.; MacPhee, C. E.; Welland, M. E., Characterization of the nanoscale properties of individual amyloid fibrils. *Proceedings of the National Academy of Sciences* **2006,** *103* (43), 15806-15811.
16. Taylor, A. I. P.; Staniforth, R. A., General Principles Underpinning Amyloid Structure. *Front Neurosci* **2022,** *16*, 878869-878869.
17. Virchow, R., Zur Cellulose —Frage. *Archiv für pathologische Anatomie und Physiologie und für klinische Medicin* **1854,** *6* (3), 416-426.

18. Nishitsuji, K.; Saito, H.; Uchimura, K., Enzymatic remodeling of heparan sulfate: a therapeutic strategy for systemic and localized amyloidoses? *Neural Regen Res* **2016,** *11* (3), 408-409.
19. Puchtler, H.; Sweat, F.; Levine, M., ON THE BINDING OF CONGO RED BY AMYLOID. *Journal of Histochemistry & Cytochemistry* **1962,** *10* (3), 355-364.
20. Astbury, W. T.; Street, A.; Bragg, W. H., X-ray studies of the structure of hair, wool, and related fibres.- I. General. *Philosophical Transactions of the Royal Society of London. Series A, Containing Papers of a Mathematical or Physical Character* **1931,** *230* (681-693), 75-101.
21. Geddes, A. J.; Parker, K. D.; Atkins, E. D. T.; Beighton, E., "Cross-β" conformation in proteins. *Journal of Molecular Biology* **1968,** *32* (2), 343-358.
22. Iadanza, M. G.; Jackson, M. P.; Hewitt, E. W.; Ranson, N. A.; Radford, S. E., A new era for understanding amyloid structures and disease. *Nature Reviews Molecular Cell Biology* **2018,** *19* (12), 755-773.
23. Hewetson, A.; Do, H. Q.; Myers, C.; Muthusubramanian, A.; Sutton, R. B.; Wylie, B. J.; Cornwall, G. A. Functional Amyloids in Reproduction *Biomolecules* [Online], 2017.
24. Romero, D.; Kolter, R., Functional amyloids in bacteria. *International microbiology : the official journal of the Spanish Society for Microbiology* **2014,** *17* (2), 65-73.
25. Pham, C. L.; Kwan, A. H.; Sunde, M., Functional amyloid: widespread in Nature, diverse in purpose. *Essays in biochemistry* **2014,** *56*, 207-19.
26. Vadukul, D. M.; Al-Hilaly, Y. K.; Serpell, L. C., Methods for Structural Analysis of Amyloid Fibrils in Misfolding Diseases. In *Protein Misfolding Diseases: Methods and Protocols*, Gomes, C. M., Ed. Springer New York: New York, NY, 2019; pp 109-122.
27. Eanes, E. D.; Glenner, G. G., X-RAY DIFFRACTION STUDIES ON AMYLOID FILAMENTS. *Journal of Histochemistry & Cytochemistry* **1968,** *16* (11), 673-677.
28. Sawaya, M. R.; Sambashivan, S.; Nelson, R.; Ivanova, M. I.; Sievers, S. A.; Apostol, M. I.; Thompson, M. J.; Balbirnie, M.; Wiltzius, J. J. W.; McFarlane, H. T.; Madsen, A. Ø.; Riekel, C.; Eisenberg, D., Atomic structures of amyloid cross-β spines reveal varied steric zippers. *Nature* **2007,** *447* (7143), 453-457.
29. Colvin, M. T.; Silvers, R.; Frohm, B.; Su, Y.; Linse, S.; Griffin, R. G., High Resolution Structural Characterization of Aβ42 Amyloid Fibrils by Magic Angle Spinning NMR. *Journal of the American Chemical Society* **2015,** *137* (23), 7509-7518.
30. Antzutkin, O. N.; Leapman, R. D.; Balbach, J. J.; Tycko, R., Supramolecular structural constraints on Alzheimer's beta-amyloid fibrils from electron microscopy and solid-state nuclear magnetic resonance. *Biochemistry* **2002,** *41* (51), 15436-50.
31. Chan, J. C. C.; Oyler, N. A.; Yau, W.-M.; Tycko, R., Parallel beta-sheets and polar zippers in amyloid fibrils formed by residues 10-39 of the yeast prion protein Ure2p. *Biochemistry* **2005,** *44* (31), 10669-10680.
32. Qiang, W.; Yau, W. M.; Lu, J. X.; Collinge, J.; Tycko, R., Structural variation in amyloid-β fibrils from Alzheimer's disease clinical subtypes. *Nature* **2017,** *541* (7636), 217-221.
33. Qiang, W.; Yau, W.-M.; Luo, Y.; Mattson, M. P.; Tycko, R., Antiparallel β-sheet architecture in Iowa-mutant β-amyloid fibrils. *Proceedings of the National Academy of Sciences* **2012,** *109* (12), 4443-4448.
34. Han, S.; Kollmer, M.; Markx, D.; Claus, S.; Walther, P.; Fändrich, M., Amyloid plaque structure and cell surface interactions of β-amyloid fibrils revealed by electron tomography. *Sci Rep* **2017,** *7*, 43577.

35. Bäuerlein, F. J. B.; Saha, I.; Mishra, A.; Kalemanov, M.; Martínez-Sánchez, A.; Klein, R.; Dudanova, I.; Hipp, M. S.; Hartl, F. U.; Baumeister, W.; Fernández-Busnadiego, R., In Situ Architecture and Cellular Interactions of PolyQ Inclusions. *Cell* **2017,** *171* (1), 179-187.e10.
36. Gremer, L.; Schölzel, D.; Schenk, C.; Reinartz, E.; Labahn, J., Fibril structure of amyloid-β(1-42) by cryo-electron microscopy. **2017,** *358* (6359), 116-119.
37. Fitzpatrick, A. W. P.; Falcon, B.; He, S.; Murzin, A. G.; Murshudov, G.; Garringer, H. J.; Crowther, R. A.; Ghetti, B.; Goedert, M.; Scheres, S. H. W., Cryo-EM structures of tau filaments from Alzheimer's disease. *Nature* **2017,** *547* (7662), 185-190.
38. Fitzpatrick, A. W. P.; Debelouchina, G. T.; Bayro, M. J.; Clare, D. K.; Caporini, M. A.; Bajaj, V. S.; Jaroniec, C. P.; Wang, L.; Ladizhansky, V.; Müller, S. A.; MacPhee, C. E.; Waudby, C. A.; Mott, H. R.; De Simone, A.; Knowles, T. P. J.; Saibil, H. R.; Vendruscolo, M.; Orlova, E. V.; Griffin, R. G.; Dobson, C. M., Atomic structure and hierarchical assembly of a cross-β amyloid fibril. *Proceedings of the National Academy of Sciences* **2013,** *110* (14), 5468-5473.
39. Jiménez, J. L.; Guijarro, J. I.; Orlova, E.; Zurdo, J.; Dobson, C. M.; Sunde, M.; Saibil, H. R., Cryo-electron microscopy structure of an SH3 amyloid fibril and model of the molecular packing. *The EMBO journal* **1999,** *18* (4), 815-21.
40. Hippius, H.; Neundörfer, G., The discovery of Alzheimer's disease. *Dialogues Clin Neurosci* **2003,** *5* (1), 101-108.
41. Alcendor, D. J., Interactions between Amyloid-B Proteins and Human Brain Pericytes: Implications for the Pathobiology of Alzheimer's Disease. *J Clin Med* **2020,** *9* (5), 1490.
42. Chiti, F.; Dobson, C. M., Protein Misfolding, Amyloid Formation, and Human Disease: A Summary of Progress Over the Last Decade. *Annual review of biochemistry* **2017,** *86*, 27-68.
43. Vassar, R.; Bennett, B. D.; Babu-Khan, S.; Kahn, S.; Mendiaz, E. A.; Denis, P.; Teplow, D. B.; Ross, S.; Amarante, P.; Loeloff, R.; Luo, Y.; Fisher, S.; Fuller, J.; Edenson, S.; Lile, J.; Jarosinski, M. A.; Biere, A. L.; Curran, E.; Burgess, T.; Louis, J. C.; Collins, F.; Treanor, J.; Rogers, G.; Citron, M., Beta-secretase cleavage of Alzheimer's amyloid precursor protein by the transmembrane aspartic protease BACE. *Science* **1999,** *286* (5440), 735-41.
44. Iqbal, K.; Liu, F.; Gong, C. X.; Grundke-Iqbal, I., Tau in Alzheimer disease and related tauopathies. *Current Alzheimer research* **2010,** *7* (8), 656-664.
45. Prusiner, S. B.; McKinley, M. P.; Bowman, K. A.; Bolton, D. C.; Bendheim, P. E.; Groth, D. F.; Glenner, G. G., Scrapie prions aggregate to form amyloid-like birefringent rods. *Cell* **1983,** *35* (2 Pt 1), 349-58.
46. Warby, S. C.; Montpetit, A.; Hayden, A. R.; Carroll, J. B.; Butland, S. L.; Visscher, H.; Collins, J. A.; Semaka, A.; Hudson, T. J.; Hayden, M. R., CAG expansion in the Huntington disease gene is associated with a specific and targetable predisposing haplogroup. *American journal of human genetics* **2009,** *84* (3), 351-66.
47. Chartier-Harlin, M. C.; Kachergus, J.; Roumier, C.; Mouroux, V.; Douay, X.; Lincoln, S.; Levecque, C.; Larvor, L.; Andrieux, J.; Hulihan, M.; Waucquier, N.; Defebvre, L.; Amouyel, P.; Farrer, M.; Destée, A., Alpha-synuclein locus duplication as a cause of familial Parkinson's disease. *Lancet (London, England)* **2004,** *364* (9440), 1167-9.
48. Valentine, J. S.; Doucette, P. A.; Zittin Potter, S., Copper-zinc superoxide dismutase and amyotrophic lateral sclerosis. *Annual review of biochemistry* **2005,** *74*, 563-93.
49. Westermark, P.; Andersson, A.; Westermark, G. T., Islet amyloid polypeptide, islet amyloid, and diabetes mellitus. *Physiological reviews* **2011,** *91* (3), 795-826.

50. Maceira, A. M.; Joshi, J.; Prasad, S. K.; Moon, J. C.; Perugini, E.; Harding, I.; Sheppard, M. N.; Poole-Wilson, P. A.; Hawkins, P. N.; Pennell, D. J., Cardiovascular Magnetic Resonance in Cardiac Amyloidosis. *Circulation* **2005,** *111* (2), 186-193.
51. Koch, K. M., Dialysis-related amyloidosis. *Kidney international* **1992,** *41* (5), 1416-29.
52. Li, X.; Song, D.; Leng, S. X., Link between type 2 diabetes and Alzheimer's disease: from epidemiology to mechanism and treatment. *Clinical interventions in aging* **2015,** *10*, 549-60.
53. Uéda, K.; Fukushima, H.; Masliah, E.; Xia, Y.; Iwai, A.; Yoshimoto, M.; Otero, D. A.; Kondo, J.; Ihara, Y.; Saitoh, T., Molecular cloning of cDNA encoding an unrecognized component of amyloid in Alzheimer disease. *Proc Natl Acad Sci U S A* **1993,** *90* (23), 11282-6.
54. Nai, Y.-H.; Shidahara, M.; Seki, C.; Watabe, H., Biomathematical screening of amyloid radiotracers with clinical usefulness index. *Alzheimers Dement (N Y)* **2017,** *3* (4), 542-552.
55. Ono, M.; Saji, H., SPECT Imaging Agents for Detecting Cerebral β-Amyloid Plaques. *Int J Mol Imaging* **2011,** *2011*, 543267.
56. Ogawa, S.; Lee, T. M.; Kay, A. R.; Tank, D. W., Brain magnetic resonance imaging with contrast dependent on blood oxygenation. *Proceedings of the National Academy of Sciences* **1990,** *87* (24), 9868-9872.
57. Leinonen, V.; Rinne, J. O.; Wong, D. F.; Wolk, D. A.; Trojanowski, J. Q.; Sherwin, P. F.; Smith, A.; Heurling, K.; Su, M.; Grachev, I. D., Diagnostic effectiveness of quantitative [^{18}F]flutemetamol PET imaging for detection of fibrillar amyloid β using cortical biopsy histopathology as the standard of truth in subjects with idiopathic normal pressure hydrocephalus. *Acta neuropathologica communications* **2014,** *2*, 46-46.
58. Vaquero, J. J.; Kinahan, P., Positron Emission Tomography: Current Challenges and Opportunities for Technological Advances in Clinical and Preclinical Imaging Systems. *Annu Rev Biomed Eng* **2015,** *17*, 385-414.
59. Xu, M. M.; Ren, W. M.; Tang, X. C.; Hu, Y. H.; Zhang, H. Y., Advances in development of fluorescent probes for detecting amyloid-β aggregates. *Acta Pharmacol Sin* **2016,** *37* (6), 719-30.
60. Zhou, M.; Wang, X.; Liu, Z.; Yu, L.; Hu, S.; Chen, L.; Zeng, W., Advances of molecular imaging probes for the diagnosis of Alzheimer's disease. *Curr Alzheimer Res* **2014,** *11* (3), 221-31.
61. Tong, H.; Lou, K.; Wang, W., Near-infrared fluorescent probes for imaging of amyloid plaques in Alzheimer′s disease. *Acta Pharm Sin B* **2015,** *5* (1), 25-33.
62. Shukla, A. K.; Kumar, U., Positron emission tomography: An overview. *J Med Phys* **2006,** *31* (1), 13-21.
63. Gomes Marin, J. F.; Nunes, R. F.; Coutinho, A. M.; Zaniboni, E. C.; Costa, L. B.; Barbosa, F. G.; Queiroz, M. A.; Cerri, G. G.; Buchpiguel, C. A., Theranostics in Nuclear Medicine: Emerging and Re-emerging Integrated Imaging and Therapies in the Era of Precision Oncology. *RadioGraphics* **2020,** *40* (6), 1715-1740.
64. Chung, W. J.; Chung, H. W.; Shin, M. J.; Lee, S. H.; Lee, M. H.; Lee, J. S.; Kim, M. J.; Lee, W. K., MRI to differentiate benign from malignant soft-tissue tumours of the extremities: a simplified systematic imaging approach using depth, size and heterogeneity of signal intensity. *Br J Radiol* **2012,** *85* (1018), e831-e836.
65. Berg, E.; Cherry, S. R., Innovations in Instrumentation for Positron Emission Tomography. *Semin Nucl Med* **2018,** *48* (4), 311-331.

66. Blokland, J. A. K.; Trindev, P.; Stokkel, M. P. M.; Pauwels, E. K. J., Positron emission tomography: a technical introduction for clinicians. *European Journal of Radiology* **2002,** *44* (1), 70-75.
67. Marcus, C.; Mena, E.; Subramaniam, R. M., Brain PET in the diagnosis of Alzheimer's disease. *Clin Nucl Med* **2014,** *39* (10), e413-e426.
68. O'Connor, M. K.; Kemp, B. J., Single-Photon Emission Computed Tomography/Computed Tomography: Basic Instrumentation and Innovations. *Semin Nucl Med* **2006,** *36* (4), 258-266.
69. Lu, F.-M.; Yuan, Z., PET/SPECT molecular imaging in clinical neuroscience: recent advances in the investigation of CNS diseases. *Quant Imaging Med Surg* **2015,** *5* (3), 433-447.
70. Guallart-Naval, T.; Algarín, José M.; Pellicer-Guridi, R.; Galve, F.; Vives-Gilabert, Y.; Bosch, R.; Pallás, E.; González, José M.; Rigla, Juan P.; Martínez, P.; Lloris, Francisco J.; Borreguero, J.; Marcos-Perucho, Á.; Negnevitsky, V.; Martí-Bonmatí, L.; Ríos, A.; Benlloch, J. M.; Alonso, J., Portable magnetic resonance imaging of patients indoors, outdoors and at home. *Scientific Reports* **2022,** *12* (1), 13147.
71. Cui, M.; Ono, M.; Watanabe, H.; Kimura, H.; Liu, B.; Saji, H., Smart Near-Infrared Fluorescence Probes with Donor–Acceptor Structure for in Vivo Detection of β-Amyloid Deposits. *Journal of the American Chemical Society* **2014,** *136* (9), 3388-3394.
72. Mora, A. K.; Nath, S., Ultrafast Dynamics of a Molecular Rotor-Based Bioprobe-PicoGreen: Understanding toward Fibril Sensing Mechanism. *The Journal of Physical Chemistry B* **2019,** *123* (41), 8767-8776.
73. Fu, W.; Yan, C.; Guo, Z.; Zhang, J.; Zhang, H.; Tian, H.; Zhu, W.-H., Rational Design of Near-Infrared Aggregation-Induced-Emission-Active Probes: In Situ Mapping of Amyloid-β Plaques with Ultrasensitivity and High-Fidelity. *Journal of the American Chemical Society* **2019,** *141* (7), 3171-3177.
74. Meech, S., Virtual Issue on Ultrafast Spectroscopy. *The Journal of Physical Chemistry B* **2021,** *125* (23), 6037-6039.
75. Liu, L.; Shao, Y.; Peng, J.; Huang, C.; Liu, H.; Zhang, L., Molecular Rotor-Based Fluorescent Probe for Selective Recognition of Hybrid G-Quadruplex and as a K+ Sensor. *Analytical Chemistry* **2014,** *86* (3), 1622-1631.
76. Drummen, G. P. C., Fluorescent Probes and Fluorescence (Microscopy) Techniques — Illuminating Biological and Biomedical Research. *Molecules* **2012,** *17*, 14067 - 14090.
77. Pei, S.; Li, J.; Zhang, C.; Zhang, G.; Zhou, Y.; Fan, L.; Wang, W.; Shuang, S.; Dong, C., TICT-Based Microenvironment-Sensitive Probe with Turn-on Red Emission for Human Serum Albumin Detection and for Targeting Lipid Droplet Imaging. *ACS Biomaterials Science & Engineering* **2022,** *8* (1), 253-260.
78. Xu, M.-m.; Ren, W.-m.; Tang, X.-c.; Hu, Y.-h.; Zhang, H.-y., Advances in development of fluorescent probes for detecting amyloid-β aggregates. *Acta Pharmacol Sin* **2016,** *37* (6), 719-730.
79. Needham, L.-M.; Weber, J.; Varela, J. A.; Fyfe, J. W. B.; Do, D. T.; Xu, C. K.; Tutton, L.; Cliffe, R.; Keenlyside, B.; Klenerman, D.; Dobson, C. M.; Hunter, C. A.; Müller, K. H.; O'Holleran, K.; Bohndiek, S. E.; Snaddon, T. N.; Lee, S. F., ThX – a next-generation probe for the early detection of amyloid aggregates. *Chemical Science* **2020,** *11* (18), 4578-4583.
80. Luo, J.; Xie, Z.; Lam, J. W. Y.; Cheng, L.; Chen, H.; Qiu, C.; Kwok, H. S.; Zhan, X.; Liu, Y.; Zhu, D.; Tang, B. Z., Aggregation-induced emission of 1-methyl-1,2,3,4,5-pentaphenylsilole. *Chemical Communications* **2001,** (18), 1740-1741.

81. Mei, J.; Leung, N. L. C.; Kwok, R. T. K.; Lam, J. W. Y.; Tang, B. Z., Aggregation-Induced Emission: Together We Shine, United We Soar! *Chemical Reviews* **2015,** *115* (21), 11718-11940.
82. Wang, Y.-L.; Fan, C.; Xin, B.; Zhang, J.-P.; Luo, T.; Chen, Z.-Q.; Zhou, Q.-Y.; Yu, Q.; Li, X.-N.; Huang, Z.-L.; Li, C.; Zhu, M.-Q.; Tang, B. Z., AIE-based super-resolution imaging probes for β-amyloid plaques in mouse brains. *Materials Chemistry Frontiers* **2018,** *2* (8), 1554-1562.
83. Das, A.; Gupta, A.; Hong, Y.; Carver, J. A.; Maiti, S., A Spectroscopic Marker for Structural Transitions Associated with Amyloid-β Aggregation. *Biochemistry* **2020,** *59* (19), 1813-1822.
84. Hong, Y.; Meng, L.; Chen, S.; Leung, C. W. T.; Da, L.-T.; Faisal, M.; Silva, D.-A.; Liu, J.; Lam, J. W. Y.; Huang, X.; Tang, B. Z., Monitoring and Inhibition of Insulin Fibrillation by a Small Organic Fluorogen with Aggregation-Induced Emission Characteristics. *Journal of the American Chemical Society* **2012,** *134* (3), 1680-1689.
85. Rania, Z.; Sahbi, A., Computational Study on Optoelectronic Properties of Donor-Acceptor Type Small π-Conjugated Molecules for Organic Light-Emitting Diodes (OLEDs) and Nonlinear Optical (NLO) Applications. In *Density Functional Theory*, Daniel, G.-M., Ed. IntechOpen: Rijeka, 2021; p Ch. 15.
86. Gour, N.; Kshtriya, V.; Gupta, S.; Koshti, B.; Singh, R.; Patel, D.; Joshi, K. B., Synthesis and Aggregation Studies of a Pyridothiazole-Based AIEE Probe and Its Application in Sensing Amyloid Fibrillation. *ACS Applied Bio Materials* **2019,** *2* (10), 4442-4455.
87. Liu, Y.; Wolstenholme, C. H.; Carter, G. C.; Liu, H.; Hu, H.; Grainger, L. S.; Miao, K.; Fares, M.; Hoelzel, C. A.; Yennawar, H. P.; Ning, G.; Du, M.; Bai, L.; Li, X.; Zhang, X., Modulation of Fluorescent Protein Chromophores To Detect Protein Aggregation with Turn-On Fluorescence. *Journal of the American Chemical Society* **2018,** *140* (24), 7381-7384.
88. Fink, A. L., Protein aggregation: folding aggregates, inclusion bodies and amyloid. *Folding and Design* **1998,** *3* (1), R9-R23.
89. Šarić, A.; Chebaro, Y. C.; Knowles, T. P. J.; Frenkel, D., Crucial role of nonspecific interactions in amyloid nucleation. *Proceedings of the National Academy of Sciences* **2014,** *111* (50), 17869-17874.
90. Michaels, T. C. T.; Šarić, A.; Meisl, G.; Heller, G. T.; Curk, S.; Arosio, P.; Linse, S.; Dobson, C. M.; Vendruscolo, M.; Knowles, T. P. J., Thermodynamic and kinetic design principles for amyloid-aggregation inhibitors. *Proceedings of the National Academy of Sciences* **2020,** *117* (39), 24251-24257.

Chapter 2

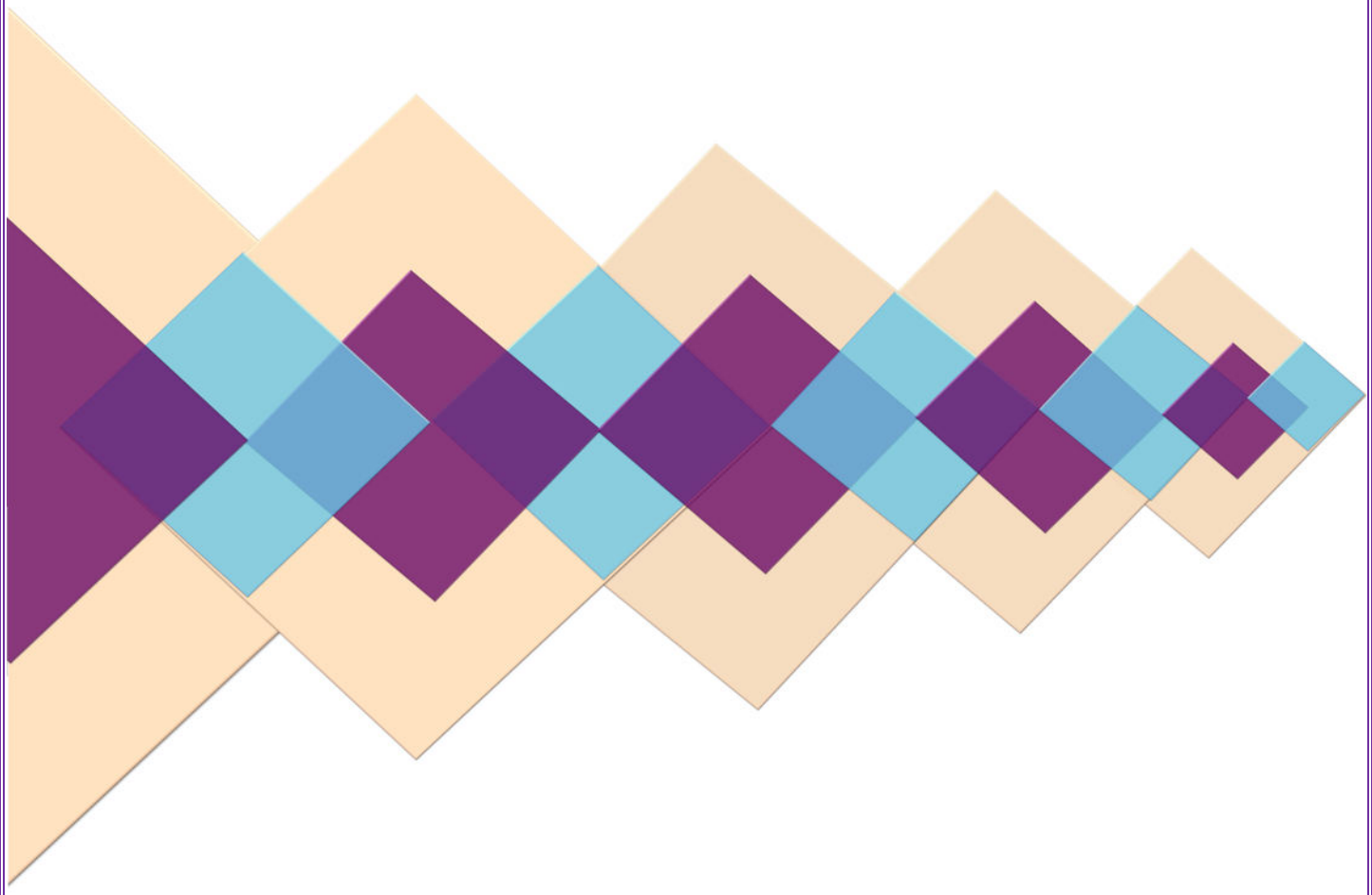

Sensing and Modulation of Amyloid Fibrils by Photo switchable Organic Dots

Sensing and Modulation of Amyloid Fibrils by Photo switchable Organic Dots

2.1 Introduction

Misfolding of amyloidogenic protein and the deposition of this protein agglomerates in different part of the human body, has the involvement in the pathology of amyloidosis, such as Alzheimer's disease, Parkinson's disease, Prion diseases, type II diabetes etc.[1-6] Certainly, i) the continuous rapid detection of amyloid fibrils formation, differentiation of transient species with distinct structural features and the attenuation of the single molecular resolution of oligomeric species and gaining the radical information on the structure and dynamics of amyloid fibrils formation are of significant diagnostics importance. In order to evaluate the amyloidogenesis of proteins, so far many efforts have been made for non-invasive detection of these aggregates mainly relying on techniques, such as magnetic resonance imaging (MRI),[7] positron emission tomography (PET),[8] single-photon emission computed tomography (SPECT)[9] etc., and most of these techniques used expensive instruments. Moreover, some of the techniques involve complicated data analysis and exposure to radioactive radiation.[10] Several biophysical techniques, such as circular dichroism (CD), light scattering, X-ray scattering, Fourier transform infrared (FTIR), and atomic force microscopy (AFM) have been used extensively to study amyloid fibrils in-vitro.[11] In addition to the above-mentioned techniques, fluorescence-based techniques are attracted burgeoning interest for both in-vivo and in-vitro detection of amyloid fibril because of its simplicity, cost-effectiveness, and high sensitivity. Several small organic molecules have been designed for the imaging of amyloid fibrils.[12-17] Sensors like curcumin, BODIPYs, p-FTAA, AS140-MFC have been developed for the detection of amyloid fibrils.[18-21] Most of the cases the detection is based on the enhancement of fluorescence intensity of the probes.[12, 22-27] Such enhancement of fluorescence is mainly due to the incorporation of fluorophore in complex fibrillar matrix, which leads to an increase in the frictional forces around the probe resulting in severe retardation in the torsional motion around rotating single bond. However, such intensity-based assessments are susceptible to self-quenching at higher concentrations of probe, making the fluorophore unsuitable for quantitative analysis.[28] Recently discovered aggregation-induced emission (AIE) based probes are able to circumvent the issue of conventional fluorescent probes, which arises at high concentration.[29] This is because AIE-based molecules generally "switch on" their fluorescence in the aggregated state.[30-32] Recently the development of such AIE-active molecules is of great interest in biological science[33-35], because of their efficient usefulness in bio-imaging

applications[35, 36] and protein fibril detection[28, 37, 38]. Typically, most of the cases AIE-based probes are non-emissive in buffer, but light up their fluorescence at a single wavelength upon binding with different species of aggregates during the fibrillation process of amyloidogenic protein.[32, 37, 39] However, few cases such single intensity-based probes exhibit undesirable false positive AIE signal due to initial aggregation before binding to the amyloid fibril.[39-41] In order to circumvent this problem, one needs an AIE based polarity sensitive probe, which exhibits AIE at_single wavelength and switches its fluorescence emission to another wavelength upon binding to the amyloid fibrils. In continuation of this effort, here we are going to present a series of donor acceptor-based charge transfer probe molecules, which forms AIE dots (DPAPMI, CPMI) and ACQ dots (DMAPMI) in buffer,[42] and able to sense insulin amyloid fibrils in terms of disaggregation induced fluorescence switching and fluorescence enhancement. This is the first report where we have shown the AIE based probes, DPAPMI and CPMI can exhibit large shift its emission maxima ~130 nm and ~80 nm, respectively, upon binding to the amyloid fibrils. The huge shift in emission maxima of these probe molecules makes them beneficial for imaging of amyloid fibrils**.** In addition, our comparative kinetic studies with thioflavin T (ThT) unveil that these organic dots are sensitive towards pre-fibrillar aggregates during aggregation process of insulin.

Very recently, several reports have demonstrated that oligomers of amyloidogenic proteins (like, Aβ 42 and alpha-synuclein, amylin) play a key role for several neurological disorder including Alzheimer's and Parkinson diseases.[43-45] Moreover, the oligomers of insulin interrupt the outgrowth and complexity of neuron-like PC12 cells.[46] Therefore, manipulating either the pathway of oligomerization or the pathway of oligomer to mature fibrils have advanced considerably in recent years. In continuation of this effort, significant approaches have been made to modulate the fibrillation process of amyloidogenic protein through intrinsic modification of monomeric structure, tuning the environment condition either by changing pH and ionic strength[47] or, peptides, nanoparticle and biopolymer etc.[46-54] However, the bigger size of the biopolymers and peptide experiences difficulty in crossing the blood-brain barriers; similarly, the inorganic nano-particles are toxic for cell.[48, 49] In order to resolve these problems, effective biocompatible molecules/species are necessary to resist the amyloidosis by reshaping the rate of fibrillation of the protein. In this context, we further examine how AIE and ACQ dots of our probe

molecules modulate the fibrillation rate of insulin, precisely the rate of formation of oligomer to mature fibrils. Our results showed that these organic dots accelerate the aggregation rate of insulin, especially, the oligomer to mature fibrils by speeding up the microscopic processes such as the secondary nucleation (with rate constant k_2) and the elongation process (with rate constant k_+). In summary, our study demonstrates these organic dots are suitable for the imaging, early-stage detection of amyloid fibril formation and the modulation of amyloid formation pathway.

2.2 Results and discussion

2.2.1 Characterization of the organic dots

The probe molecules DPAPMI, CPMI and DMAPMI were synthesized and characterized by our group.[42] The AIE dots of DPAPMI, CPMI was prepared in 90:10 water/THF mixture, and the resultant probe concentration of the solutions was 1 mg/ml. Then, the solutions were sonicated vigorously for 1h. The formation of AIE dots of these probe molecules confirmed by using scanning electron microscopy (Figure 2.1a, b, c**)** and DLS measurements (Figure 2.1d, e, f). On the contrary to DPAPMI and CPMI, DMAPMI forms ACQ dots at the same condition. The scanning electron microscopic study indicates that these probe molecules form spherical dots.

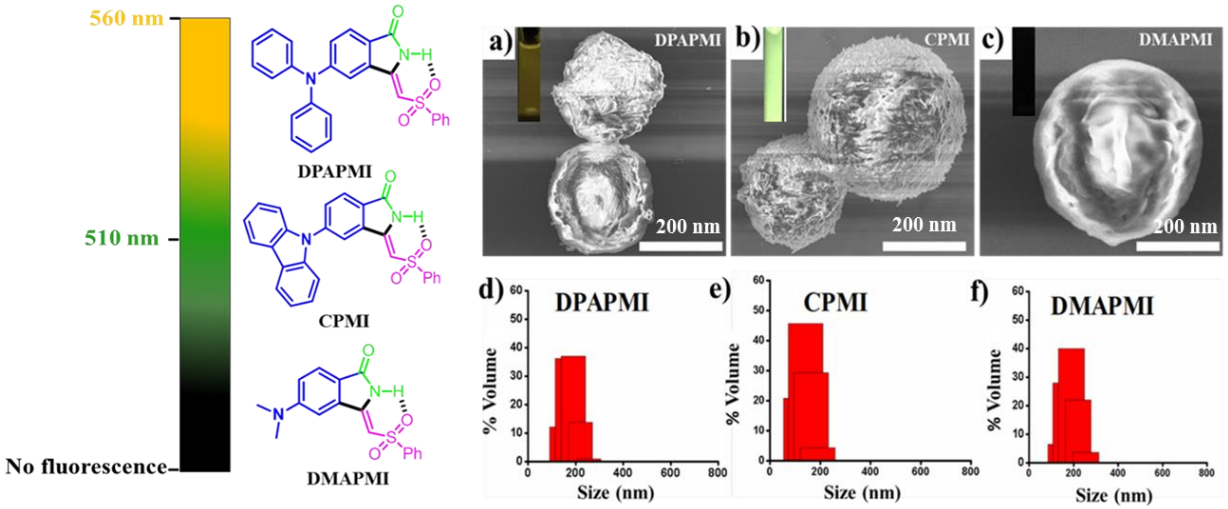

Figure 2.1 SEM images of the organic dots derived in 9:1 water/THF mixture. a) DPAPMI, b) CPMI, c) DMAPMI. Particle size distribution via dynamic light scattering (DLS) in water/THF mixture of d) DPAPMI, e) CPMI, f) DMAPMI.

Sensing and Modulation of Amyloid Fibrils by Photo switchable Organic Dots

2.2.2 In-vitro detection of insulin amyloid fibrils by the organic dots

The emission spectra of DPAPMI, DMAPMI and CPMI in aqueous solution (in Tris-HCl buffer of pH 7.4) and the presence of insulin fibril have been recorded, and the results are shown in Figure 2.2. Here it is necessary to mention that DPAPMI and CPMI in buffer form AIE dots and exhibit aggregation-induced emission (AIE) around 560 and 510 nm, respectively. The emission is attributed to the restriction of intramolecular rotation of charge-transfer (CT) state of the molecules in the aggregated state in the presence of poor solvent, such as water.[42] Interestingly, the emission spectrum of DPAPMI shows huge hypsochromic shift (130 nm) from 560 to 430 nm upon addition of insulin fibril along with significant enhancement of fluorescence intensity, thereby leading to change in color from orange to blue (Figure 2.2a**)**. Similarly, CPMI exhibits fluorescence color switch from green (~510 nm) to blue color (~420 nm) upon the addition of insulin amyloid fibrils (Figure 2.2b). Both the cases, the switching in emission color indicates that the molecules at low energy CT state reaches to high energy locally excites (LE) state upon addition of amyloid fibrils, in which biphenyl/carbazole rings are not properly oriented for effective charge transfer process to take place. Moreover, the hypsochromic shift in emission spectra manifests that the molecules prefer to go hydrophobic surface of insulin fibrils resulting in the disaggregation of AIE dots because of change in polarity around it. Time-resolved fluorescence measurement have been carried out to understand the effect of the excited-state dynamic of both the probes. The average decay time of the probe at the CT state (λ_{ex} = 375 nm, λ_{em} = 550 nm) of DPAPMI decrease upon addition of amyloid fibrils (Appendix 2.3, Appendix table 2.2 in Appendix), which may be an indication of disaggregation of the aggregated states of the molecules. On the other hand, an increase in the average lifetime at LE state (λ_{ex} = 375 nm, λ_{em} = 435 nm) of DPAPMI infers the stabilization of the molecules at the LE state in presence of fibrillar assembly (Figure 2.2d**,** Appendix Table 1,2 in Appendix**)**. Surprisingly, in the case of CPMI, we have observed increment in the lifetime at both LE (λ_{ex} = 375 nm, λ_{em} = 420 nm**)** and CT (λ_{ex} = 375 nm, λ_{em} = 510 nm**)** state (Figure 2.1e, Table 2.1a, b, and Appendix 2.4 in Appendix) indicating that both the states of CPMI are getting stabilized in the presence of insulin amyloid fibrils. In a nutshell, both DPAPMI and CPMI can be considered as 'fluorescence switching' probes for the detection of amyloid fibril. In particular, the huge shift in the emission spectra is helpful for

fluorescence imaging experiments due to the relatively reduced background noise, which may improve the detection limit significantly.

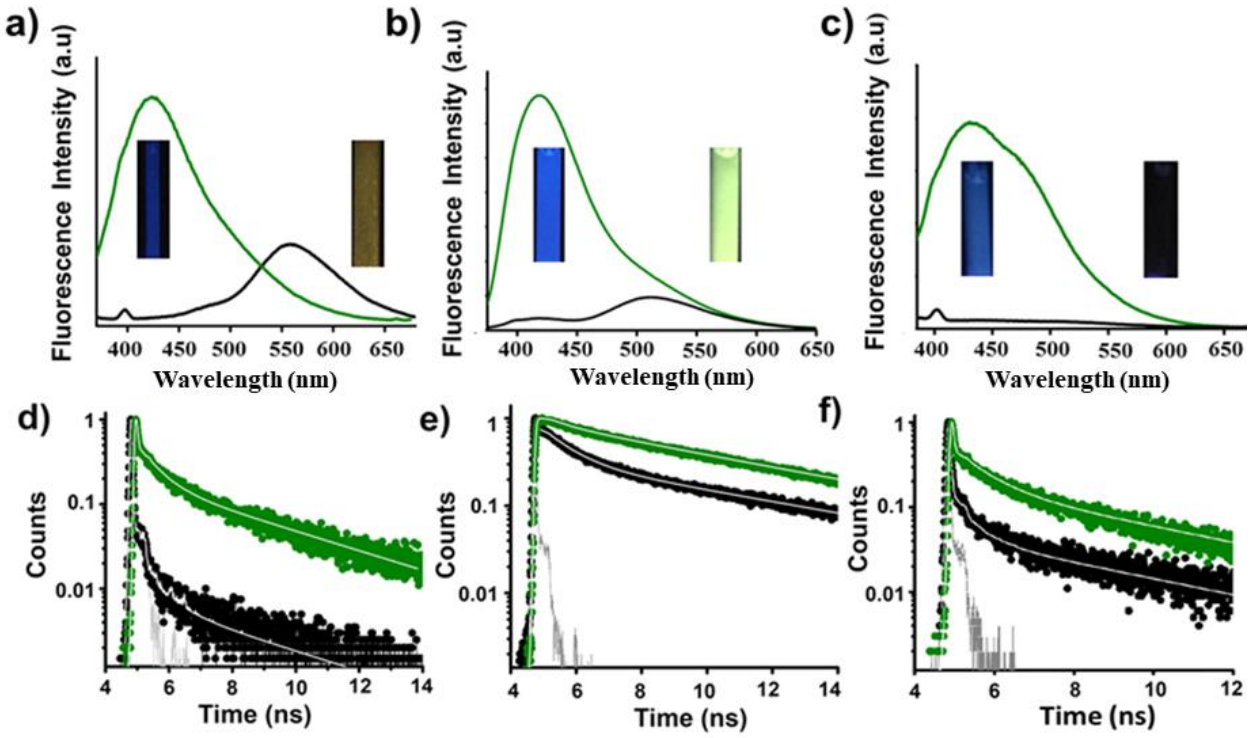

Figure 2.2 a), b), c) Emission spectra (λ_{ex} = 350 nm) of DPAPMI, DMAPMI and CPMI, respectively in the presence of 0 (black) and 50 μM (green) insulin fibrils. d), e), f) Emission transient decay of DPAPMI, DMAPMI (λ_{ex} = 375, λ_{col} = 435 nm), and CPMI (λ_{ex} = 375, λ_{col} = 420 nm), respectively in the absence (black) and presence (green) of insulin fibrils.

Contrary to DPAPMI and CPMI, DMAPMI exhibits fluorescence "turn on" property (Figure 2.2c) in the presence of amyloid fibril. Here it is pertinent to mention that DMAPMI exhibits negligible fluorescence in water due to aggregation caused quenching (ACQ) effect attributing to the smaller size of the dimethyl-amino (DMA) groups, which are not sufficient enough to disturb the π–π stacking interactions between the core PMI moieties in the aggregated state. The negligible fluorescence in water may be attributed to the highly efficient CT process in DMAPMI (compared to DPAPMI and CPMI) due to maximum overlap of donor-acceptor orbital,

as it is also evident from the minimum angle between the DMA and PMI cores observed in the crystal of DMAPMI.[42] As the CT state is highly stabilized in water, non-radiative decay pathway dominates, thereby leading to the negligible fluorescence in water. Now, upon interaction of aggregated fluorescent probe with hydrophobic amyloid fibril, the probes are disaggregated followed by their distribution over the hydrophobic binding sites of amyloid plaque surfaces, which results in the increase of fluorescence intensity of the probes. A significant increment in the average excited-state lifetime of the probe (Figure 2.2f) molecules also supports that the non-radiative decay path of the probe is getting prevented in the presence of amyloid fibril due to the interaction between molecule and amyloid fibril. Overall, DMAPMI acts as a fluorescence 'turn on' probe for the detection of amyloid fibril. In particular, 'turn on' fluorescence property of the probe is desirable due to low background noise and high sensitivity when binds to amyloid fibrillar assembly in the biological system.

2.2.3 d-STORM imaging of insulin amyloid fibrils stained with the organic dots.

In the pursue of visualization of amyloid fibrils surface in the presence of our organic dots, super-resolution microscopy was performed by using d-STORM (stochastic optical reconstructions microscopy) setup. The d-STORM technique has been proven to overcome the challenges of diffraction limit which generally faced by common light microscopy. Here, we observed the probe molecules (AIE/ACQ in buffer) forming spherical dots that exhibit bright fluorescence (Appendix 2.7). However, when incubated in the presence of insulin fibrils, several elongated features were noticed along with the spherical dots. The images were then digitally processed (recipe, Appendix 2.4.10) and compared with the corresponding raw images in Figure 2.3. Overall, d-STORM microscopy study suggests that our molecules can be useful for high resolution imaging of amyloid fibrils.

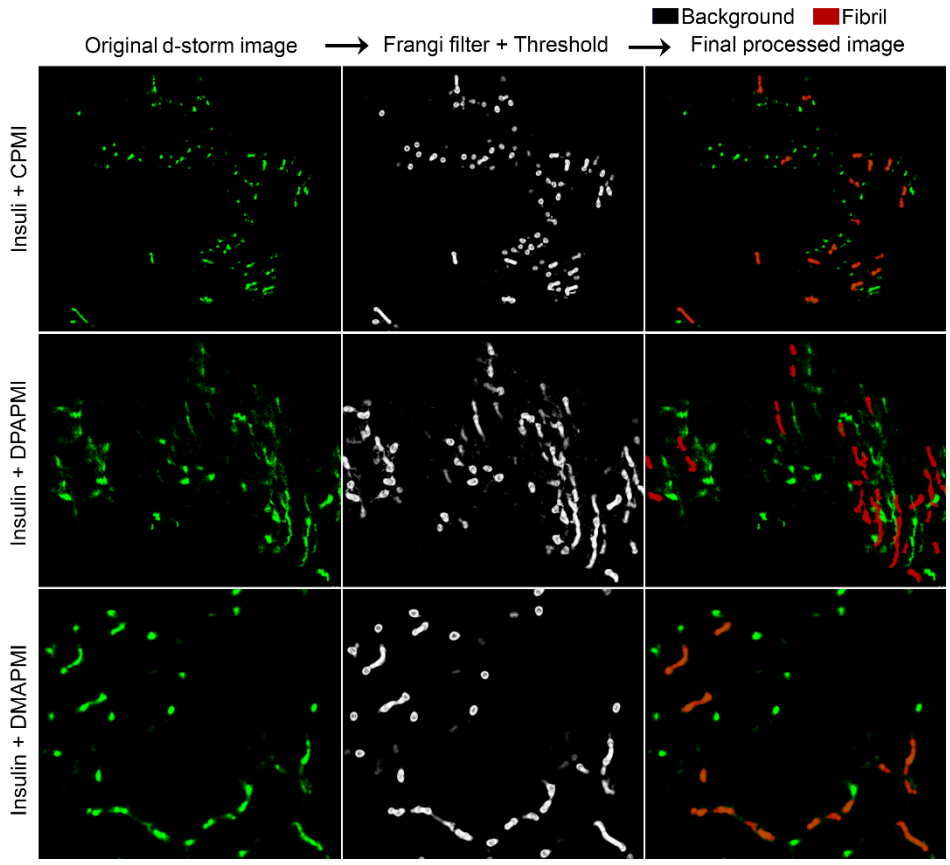

Figure 2.3 Original d-STORM super-resolution microscopic images of insulin fibrils stained with our probe molecules in comparison with post processed images. Processing steps were shown at the top of each vertical panel and sample ID was shown at the left side of corresponding original images.

2.2.4 Monitoring the disaggregation of the organic dots by FLIM

In order to confirm the disaggregation of AIE/ACQ dots at charge transfer state and the distribution of probe molecules on the surface of amyloid fibrils, we map the AIE/ACQ dots of our probe molecules in the presence and absence of amyloid fibrils using fluorescence lifetime imaging microscopy (FLIM). The FLIM images also show that the AIE/ACQ molecules form spherical dots in buffer solution at the specified molar concentration (Appendix 2.8). But addition of amyloid fibril renders the change of surface morphology of the resultant hybrid. This was shown in Figure 2.4, where a stepwise image analysis (recipe, SI†) were performed in order to identify the underlying insulin fiber matrix using Frangi filter, [R1] which is a very

powerful tool in identifying fibrous structure hidden in an image which otherwise difficult to see. The fluorescence lifetime histograms were achieved by graphing the lifetime distribution extracted from the images and was shown in Figure 2.5. A monomodal distribution of lifetime centered typically at ~6 ns was observed for the DPAPMI and CPMI samples (Figure 2.5a), 5c), respectively). Interestingly, the lifetime distribution shifted to a higher time-scale, typically ~7.5 ns, for both the samples in the presence of insulin fibrils (Figure 2.5b) and 5d), respectively). The shift in average lifetime towards the higher time-scale can be a result of change in the micro-heterogeneous environment around the probe molecule or stabilization of the LE state at the aggregated condition. In either case, the shift supports the binding of our probe molecules on the surface of fibrous matrix. In addition, the distribution width become narrower (with a small tail towards the lower lifetime window) upon cohabitation with the fibrils. As DMAPMI is very weakly fluorescent in buffer, we could not able to get proper FLIM image of DMAPMI. However, upon installation of insulin amyloid fibrils, we could able to get proper FLIM image, and FLIM image depicts that average lifetime distribution of DMAPMI is centered at ~10 ns (Appendix 2.9). In summary, the FLIM data infers that the AIE/ACQ dots of the probe molecules are getting disassemble and coated on the hydrophobic surface of the fibrillar matrix.

Sensing and Modulation of Amyloid Fibrils by Photo switchable Organic Dots

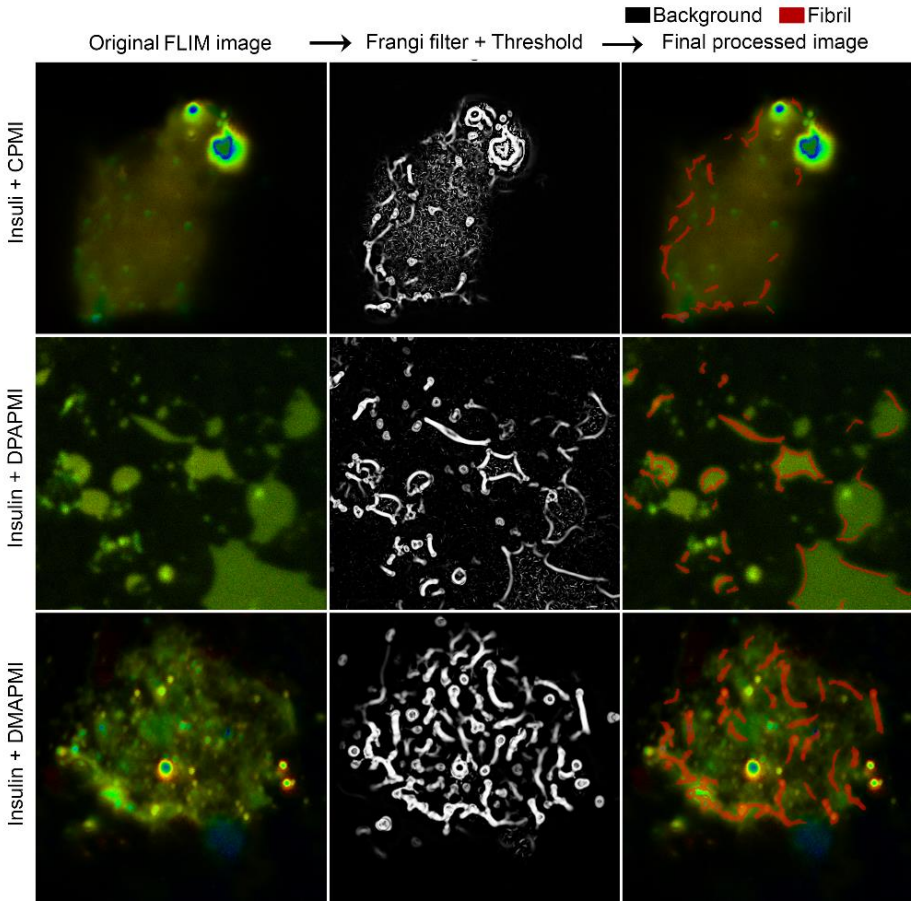

Figure 2.4 Original FLIM-Z stack (400×400 pixel) images (λ_{ex} = 405 nm, λ_{col} =430-700 nm) of insulin fibrils stained with our probe molecules in comparison with post processed images. Processing steps were shown at the top of each vertical panel and sample ID was shown at the left side of corresponding original images

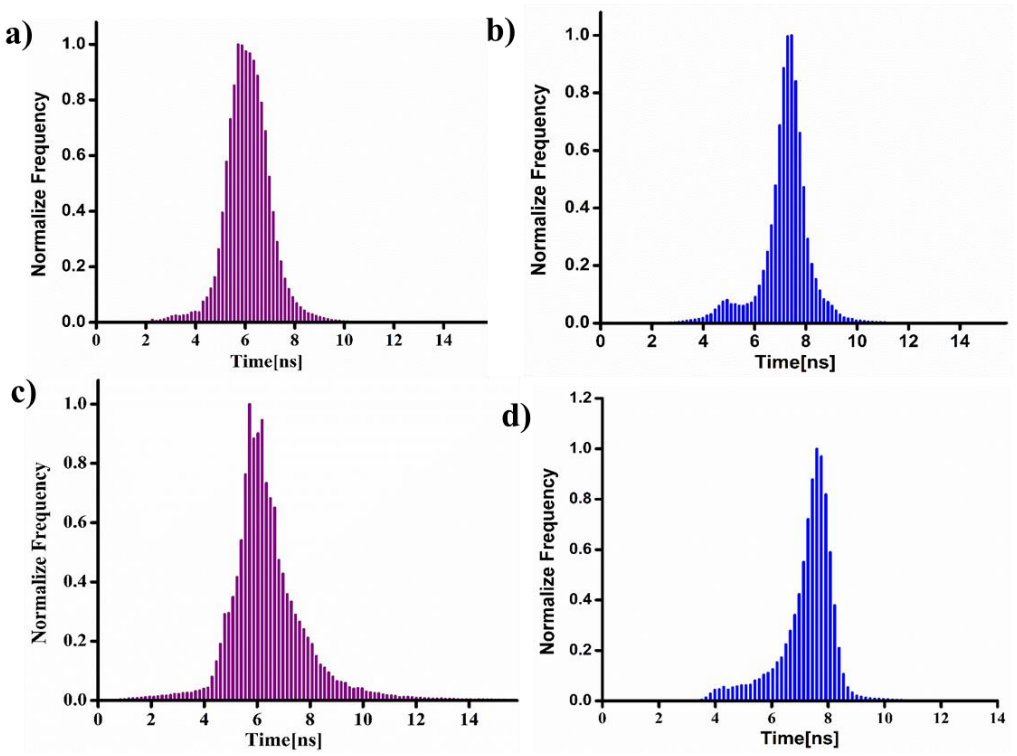

Figure 2.5 Lifetime distributions of fluorescents probes in the absence and presence of amyloid fibrils fibrils; a) DPAPMI in buffer, b) DPAPMI in fibrils, c) CPMI in buffer and d) CPMI in fibrils.

2.2.5 Effects of organic dots on the aggregation kinetics of the insulin

To investigate the effects of the organic dots on the insulin fibrillogenesis, we monitor the change in CD signal at 220 nm with respect to time in the absence and presence of probe molecules at pH 2 (Figure 2.6a, b). The native insulin at low pH shows alpha-helix in structure with two negatives cotton effects at 208 and 222 nm, and this secondary structure of insulin changes from alpha-helix to cross β-sheet upon incubation at 65° C over time, which is required for fibril formation.[50] The collected aggregation profiles of different concentrations of insulin are fitted globally using single rate law, where the microscopic rate constants are fixed, and only the independently measured initial concentrations are entered as initial conditions for the individual experiments. Then, we performed quantitative analysis of the aggregation profiles based on rate law derived from the master equation (equation 1) that associates the macroscopic time evolution of the quantity of fibrils (M(t)), which is the function of the rate constants (k_+, k_2, k_n in equation

1) related to the different microscopic events.[51] This approach using the chemical kinetic for the quantitative detection of the effects of organic dots on the aggregation process do not require prior knowledge of the elusive structure of toxic species of the aggregation-prone proteins.[52]

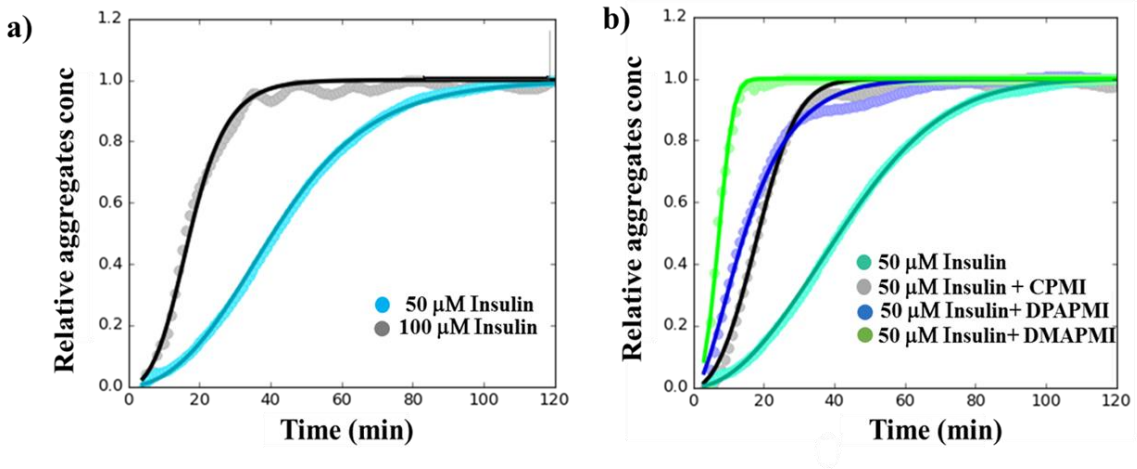

Figure 2.6 a) Kinetic aggregation study of insulin (at pH 2 and 65° C) monitored by far-UV CD at 220 nm ● 50 μM Insulin ● 100 μM Insulin. b) Kinetic aggregation study of insulin (at pH 2 and 65° C) monitored by far-UV CD at 220 nm ● 0 μM probes, ● 8 μM CPMI, ● 8 μM DPAPMI and ● 8 μM DMAPMI.

The analyses from the aggregation profile of 50 μM insulin in the presence of our organic dots suggest an appreciable modulation of the fibrillation process. A relative increment in the microscopic rate constant k_n (primary nucleation) and k_+ (elongation) in the case of DPAPMI, and prominent enhancement of k_2 (secondary nucleation) along with k_+ (elongation) in the case of CPMI and DMAPMI (Appendix 2.1, Figure 2.6b), has been observed. These results are coaxial with the classical nucleation-elongation model for fibrillation kinetics, but differ in the mode of action depending on the choice of our organic dots. While, the organic dots of DPAPMI catalyze the aggregation process through homogeneous nucleation, the other organic dots (CPMI and DMAPMI) do it through a heterogeneous nucleation pathway. It is worth to mention here that, though most of the mature fibrils are originated from the soluble oligomer through a primary nucleation (homogeneous) pathway commonly characterized by a sigmoidal growth dynamics[53], however, once the critical concentration of mature aggregates is reached, a competitive secondary nucleation (heterogeneous) can starts and soon overhauling the primary nucleation process, occasionally characterized an exponential growth of the fibrils.[54-56] Notably, many studies

speculate that the secondary nucleation process identified as the origin of toxic oligomer in the brain of patients suffering from Alzheimer's disease.[53] Therefore, it would be very interesting if one can understand and modulate the secondary nucleation process in addition to the primary nucleation process, which indeed is an additional rationale of our present study. Altogether, from this analysis we concluded that the nucleation and elongation process are getting speed up in presence of our organic dots upon binding to the oligomeric species, which provide a catalytic surface for incoming monomer leading to the promotion of the mature fibrils. The fibrillation was schematically shown in Figure 2.7.

Table 1 Microscopic rate constants in the presence and absence of our probe molecules.

Process **Rate constant**	**Primary nucleation** (k_n) $M^{-1} S^{-1}$	**Secondary nucleation** (k_2) $M^{-2} S^{-1}$	**Elongation** (k_+) $M^{-1} S^{-1}$
50 μM Insulin	0.646 ± 0.041	(4.17 ± 0.48) ×10^4	(2.54 ± 0.19) ×10^5
50 μM Insulin+ DPAPMI	2.47 ± 0	203 ± 0	(1.07 ± 0.36)×10^6
50 μM Insulin+ CPMI	0.668 ± 0.12	(2.77 ± 0.83) ×10^5	(7.16 ± 1.2) ×10^5
50 μM Insulin+ DMAPMI	1.03 ± 0.42	(8.80 ± 3.4)×10^5	(2.08 ± 1.7) ×10^6

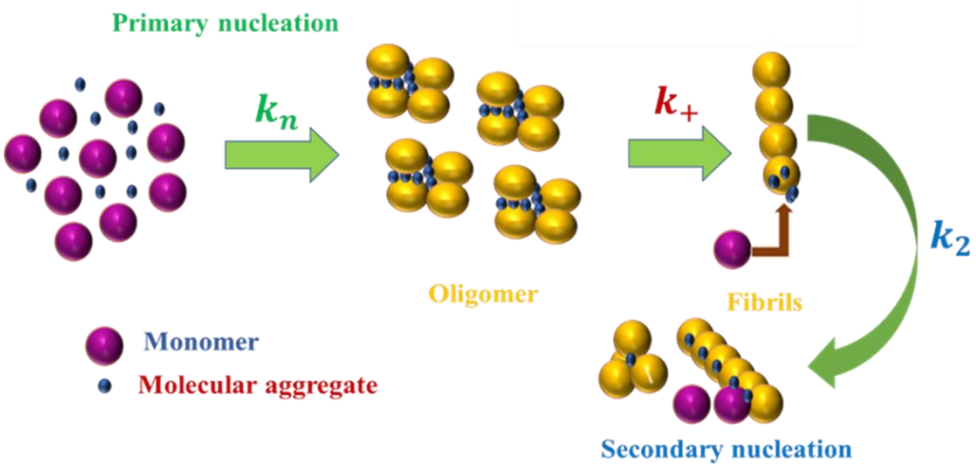

Figure 2.7 Schematic representation of the effect of probe molecules on aggregation mechanisms underlying the formation of amyloids from human insulin at pH 2.

2.2.6 Study of the morphological change of amyloid fibrils by the organic dots

To understand the effect of our organic dots on the morphology of insulin fibrils, we have carried out the AFM study of the insulin fibrils in the presence and absence of these organic dots at two different pH. The raw images are then subjected to several image processing steps (recipe, Appendix) in order to extract the useful information from the analysis. The comparison of the original image with that of final processed results are shown in the Figure 2.8 and 9 for pH 2 and 7.4, respectively. From the initial analysis of original AFM images of insulin fibrils formed at pH 2 suggests that, a higher-order aggregates are formed in the presence of our organic dots compared to the fibrils without any dots (left vertical panel, Figure 2.8). However, after processing the original images (right vertical panel, Figure 2. 8) we observed an increase in mean aspect ratio and eccentricity of the fibrils in the presence of our organic dots while the area fraction and roundness factor decrease concomitantly than the pure insulin. The results are tabulated in the table 2. To rationalize these evidential changes in the architecture of fibrils, we hypothesize that most of the organic dots partially disintegrate into individual molecule at lower pH and moves to the hydrophobic pockets of the fibrils (or a partially-folded intermediate due to unfolding of fibrils), rendering higher accessible surface area for the elongation process. The individual molecule diffuses throughout the surface and the grooves of the fibrillar channel stabilized via π–π and other non-covalent interaction such as, C=O···H-C, C-H···O=S, CH···, C=O···etc. Therefore, the lowering of area fraction and roundness factor along with the increase in aspect ratio and eccentricity, clearly suggests the promotion of fibril elongation at the same initial fibril concentration.

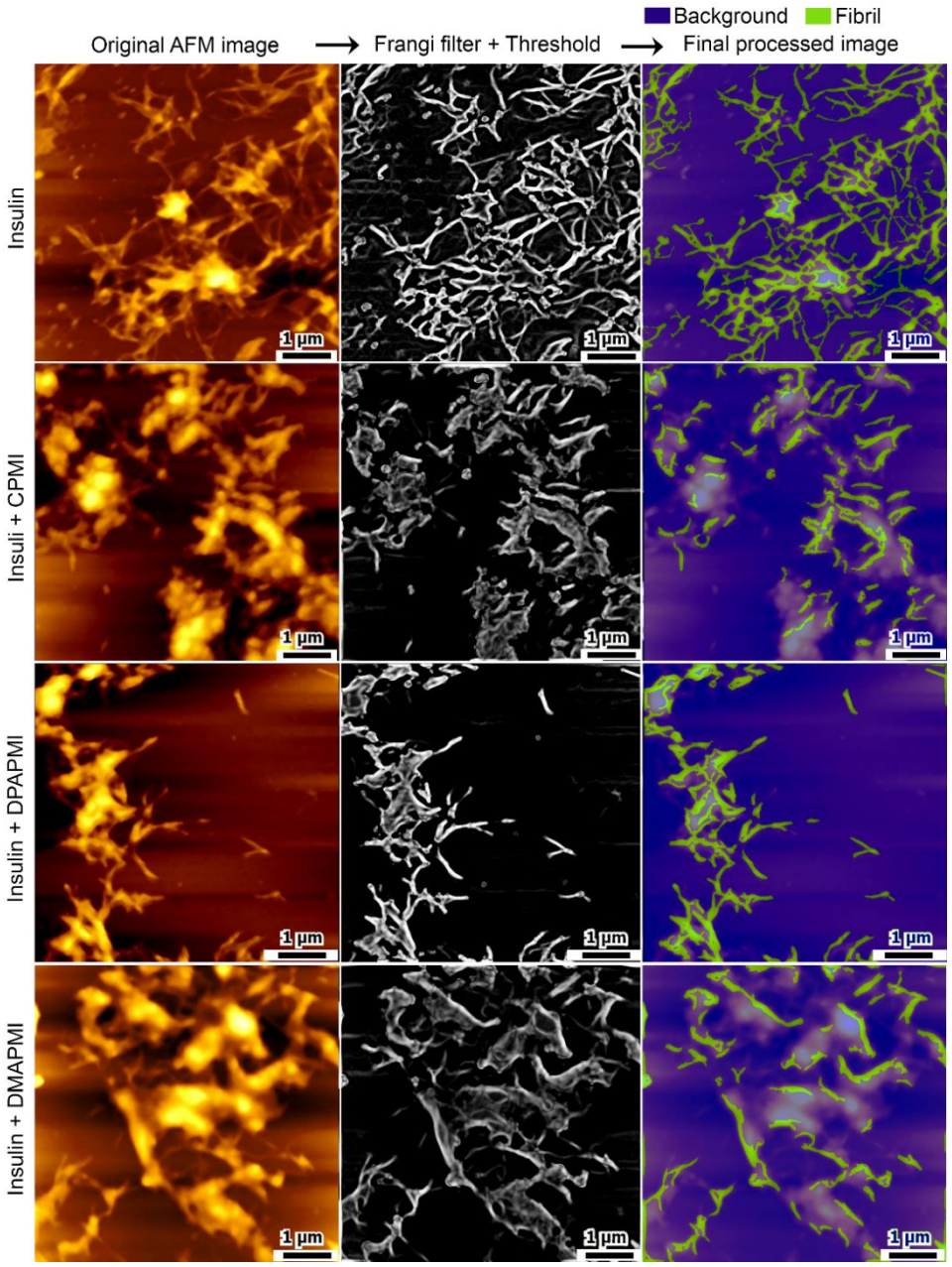

Figure 2.8 Original AFM images of insulin fibrils stained without and with our probe molecules at pH 2 in comparison with corresponding post processed images. Processing steps were shown at the top of each vertical panel and sample ID was shown at the left side of corresponding original images.

Table 2 Feature measurement list at pH 2. [a,b,c, d] Definition are given in SI.

Sample ID	Feature measurement parameters				
	Fibril area fraction	**Mean aspect ratio[a]**	**Mean eccentricity[b]**	**Mean roundness[c]**	**Mean roughness[d]**
Insulin	23.9	2.04 (±1.4)	0.49 (±0.45)	0.89 (±0.35)	1.32 (±0.68)
Insulin + CPMI	9.26	3.3 (±1.4)	0.90 (±0.09)	0.52 (±0.12)	1.58 (±0.41)
Insulin + DMAPMI	10.06	3.05 (±1.42)	0.9 (±0.08)	0.51 (±0.14)	1.84 (±0.9)
Insulin + DPAPMI	10.76	3.99 (±2.5)	0.91 (±0.12)	0.48 (±0.14)	1.66 (±0.7)

Table 3 Feature measurement list at pH 7.4. [a,b,c,d] Definition are given in SI.

Sample ID	Feature measurement parameters				
	Fibril area fraction	**Mean aspect ratio[a]**	**Mean eccentricity[b]**	**Mean roundness[c]**	**Mean roughness[d]**
Insulin	3.89	4.20 (±2.7)	0.93 (±0.06)	0.50 (±0.14)	1.50 (±0.41)
Insulin + CPMI	8.51	4.03 (±1.97)	0.93 (±0.06)	0.43 (±0.09)	1.77 (±0.59)
Insulin + DMAPMI	26.32	3.60 (±2.08)	0.93 (±0.05)	0.44 (±0.09)	1.99 (±0.77)
Insulin + DPAPMI	31.43	3.06 (±1.66)	0.90 (±0.09)	0.45 (±0.10)	2.10 (±0.74)

It has been reported that the insulin fibrils get destabilize upon alteration of pH 2 to 10.[49] The alteration of pH 2 to 7.4 indeed support this fact (Appendix 2.2). Now in order to confirm the impact of organic dots on the stability of insulin fibrils, we first adjust the pH of the solution containing fibrils and organic dots at pH 7.4 and successively incubate the samples at room temperature for one day. After that we monitor the fibrils using CD and AFM. The AFM images were analyzed stepwise (recipe,) in a similar way as we did before for the pH 2 samples. Our results suggest that the organic dots maintain the fibril structure in-spite of changing pH 2 to 7.4. Not only that, the mean eccentricity and roundness factor of the fibrils remain almost unaltered with respect to pure insulin, while the aspect ratio and area fraction increases considerably. These results are tabulated in the table 3. Therefore, we visualize the process as an initial destabilization of the fibril structure at the early stage to a partially-folded intermediate due to the change in pH, leading to higher concentration of the fibril precursors. As a result, adsorption of the organic dots (or partially disintegrated molecules) on the precursors' surface through hydrophobic interactions

which promote both a faster bulk nucleation and enhanced effect of secondary nucleation pathway, leading to thickening and branching of fibrillar structure. The CD data further confirm that our organic dots stabilize the β-sheet structure of the fibrils (Appendix 2.4) which can act as a catalytic site for the secondary nucleation. Overall, the above studies demonstrate that our organic dots have a huge impact on the stability as well as the morphology of insulin amyloid fibrils.

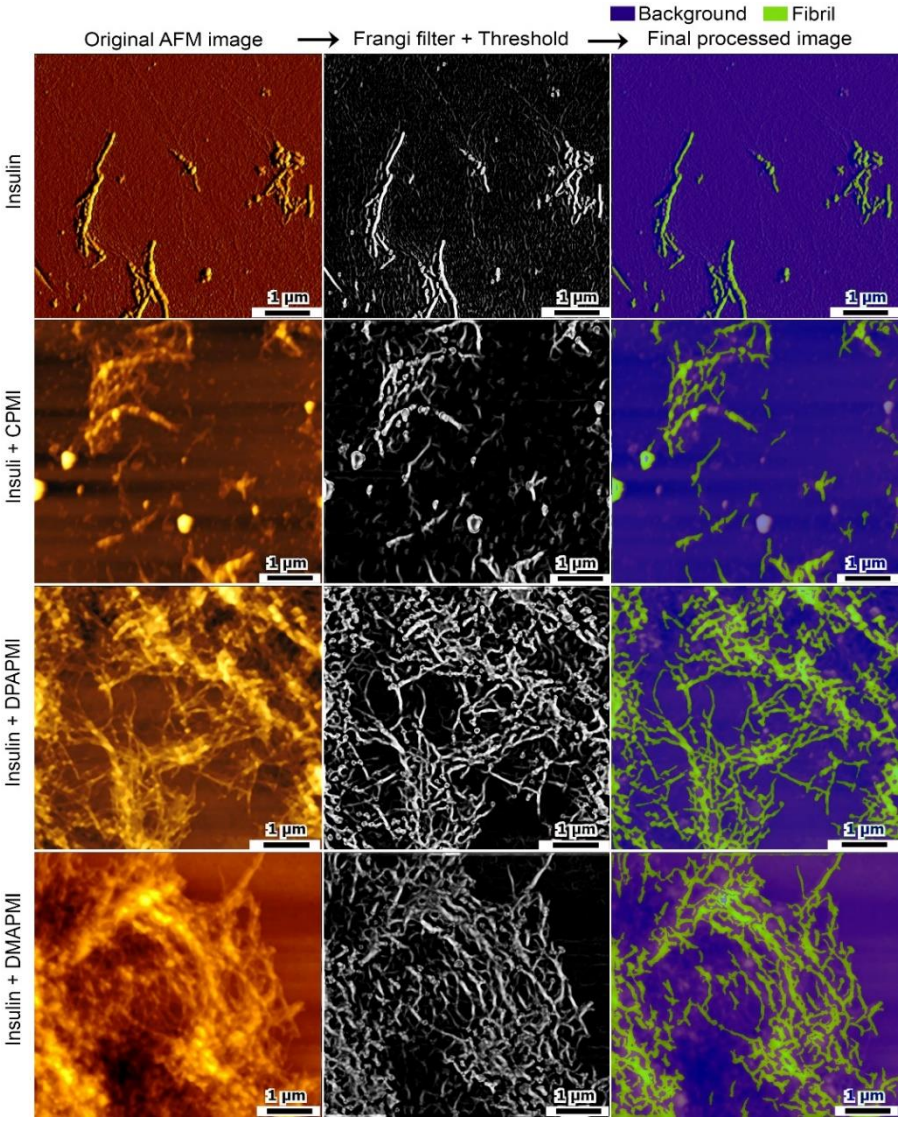

Figure 2.9 Original AFM images of insulin fibrils stained without and with our probe molecules at pH 7.4 in comparison with corresponding post processed images. Processing steps were shown at the top of each vertical panel and sample ID was shown at the left side of corresponding original images

2.2.7 Comparative aggregation kinetic study

In order to investigate whether the probe molecules can detect the monomer aggregation at the early stage, we have incubated the insulin solution in hydrophobic microplates at 37 °C for similar period of time, independently with DPAPMI, CPMI and DMAPMI, and monitored the aggregation kinetics (Figure 2.10). For the comparison purpose, the insulin solution was also incubated with thioflavin T (ThT) under same experimental condition. The changes in the fluorescence of our probe molecules and ThT fluorescence were monitored over time at the same condition for generating aggregation kinetic curve of insulin (Figure 2.10). The curves were fitted individually by sigmoid function (equation 2) which gives $t_{½}$ value (transition midpoint) of the curve. The series of $t_{½}$ values are sequentially given as: 46.5 ±0.08 h for ThT, 40.7±0.1306 h for DMAPMI, 31.46±0.19 h for DPAPMI and 14±3.37 for CPMI. Interestingly, we observe that the $t_{½}$ values of aggregation kinetic of insulin monitored with these organic dots are significantly lower than ThT, which indicates that our organic dots can detect the early-stage aggregates of insulin aggregations.

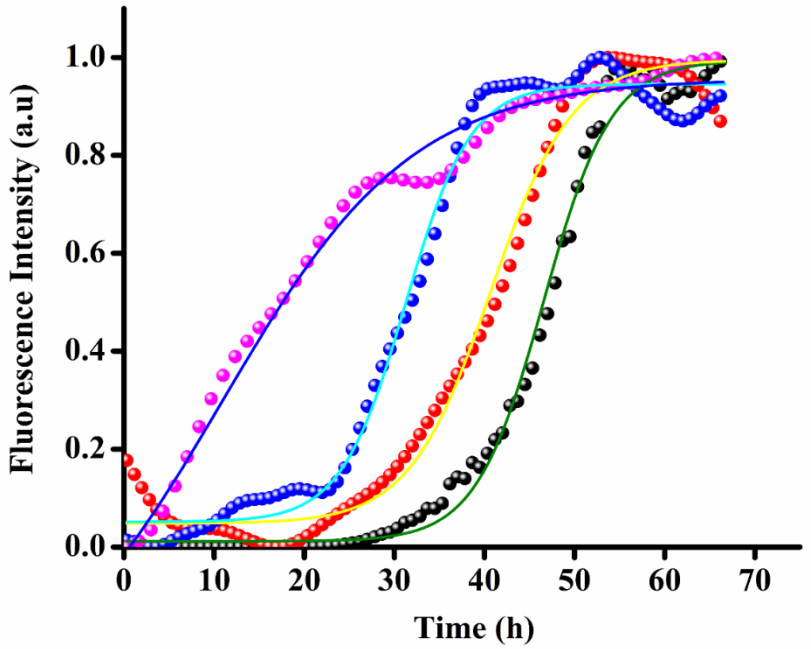

Figure 2.10 Time-course aggregation profiles of insulin amyloid fibril-forming at 37° c as monitored by ThT (black circle) and DPAPMI (blue circle), CPMI (magenta circle), and DMAPMI (red circle) fluorescence. Solid lines indicate the fitting data.

2.2.8 Evaluation of cytotoxic activity of the organic dots

In order to investigate the cytotoxic activity of our organic dots, we have performed cell viability assay of HEK293 cells in the presence of CPMI and DMAPMI. These experiments demonstrate that no significant decrease in cell viability in samples incubated with CPMI up to 50 µM (Figure 2. 11b). In the case of DMAPMI, a significant decrease in cell viability was observed from 32 µM onwards, which is 4-fold higher than the concentration required for the aggregation assay (Figure 2.11a). Overall, cell viability assay indicates that our probes have no toxicity up to concentration of 35 µM (Figure 2.11).

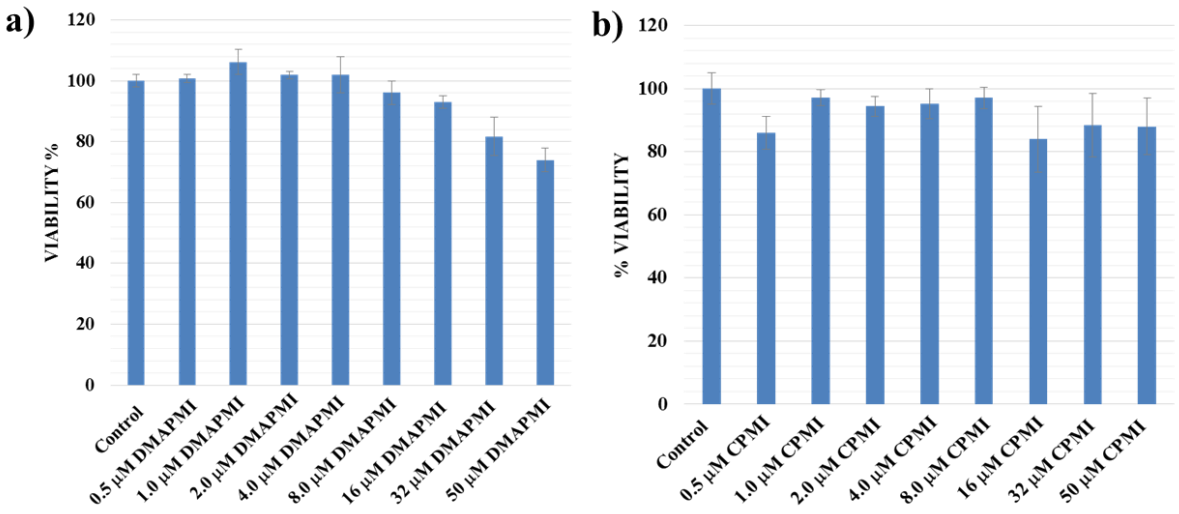

Figure 2.11 Viability HEK293 cells exposed to different concentrations of, a) DMAPMI and b) CPMI for 48 h.

2.3 Conclusive remarks

In this study, we have introduced a series of fluorescent probes, which form aggregation-induced emission (AIE) (DPAPMI, CPMI) and aggregation caused quenching (ACQ) dots (DMAPMI) at charge-transfer (CT) state in buffer medium, and they are able to efficiently sense insulin amyloid fibrils in terms of disaggregation induced fluorescent switching (DPAPMI, CPMI) and enhancement (DMAPMI). Moreover, the comparison of kinetic studies with ThT suggests that our organic dots can sense pre-fibrillar aggregates of insulin during aggregation process, which may

be beneficial for early detection of amyloid fibril. Furthermore, we have probed how these AIE and ACQ dots of our probe molecules modulate the fibrillation pathway. Our results indicate that these organic dots accelerate the aggregation rate of insulin, especially, the oligomer to mature fibrils by speeding up the microscopic processes such as the secondary nucleation (with rate constant k_2) and the elongation process (with rate constant k_+). Notably, our AIE dots have excellent biocompatibility and cell permeability; so, these organic dots may be effective probes for *in-vivo* detection of amyloid fibrils. Thus, we believe that our probe molecules may be assigned as a drug, which can reduce the toxicity of soluble oligomers (suspected to be the main culprits for Alzheimer's and Parkinson's disease) by promoting them into mature fibrils.

2.4 Appendix Section

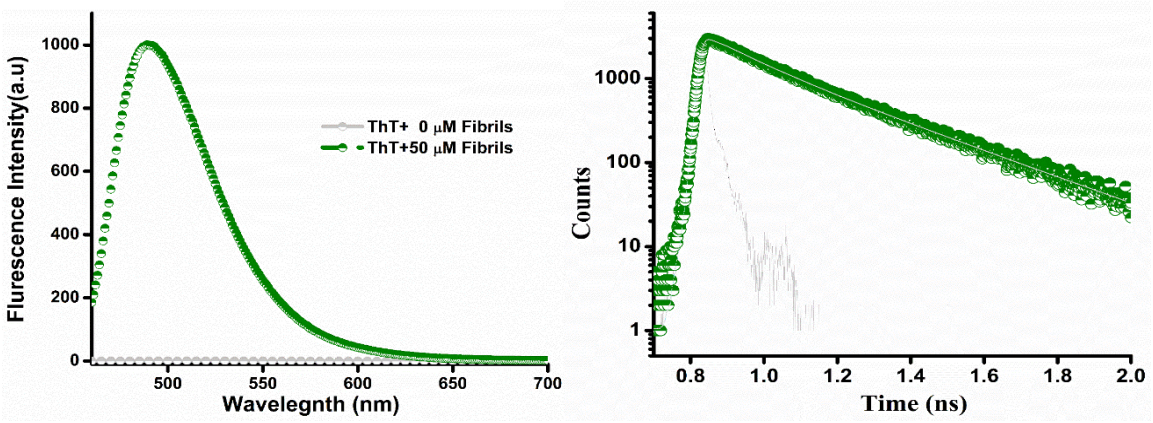

Appendix 2.4.1 Confirmation of fibril formation by Thioflavin-T (ThT).

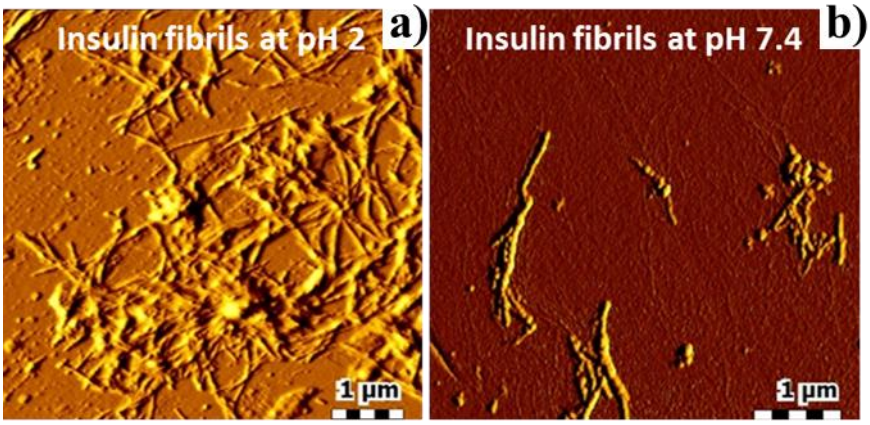

Appendix 2.4.2 AFM topography images of the a) fibrils at pH 2 and b) fibrils at 7.4.

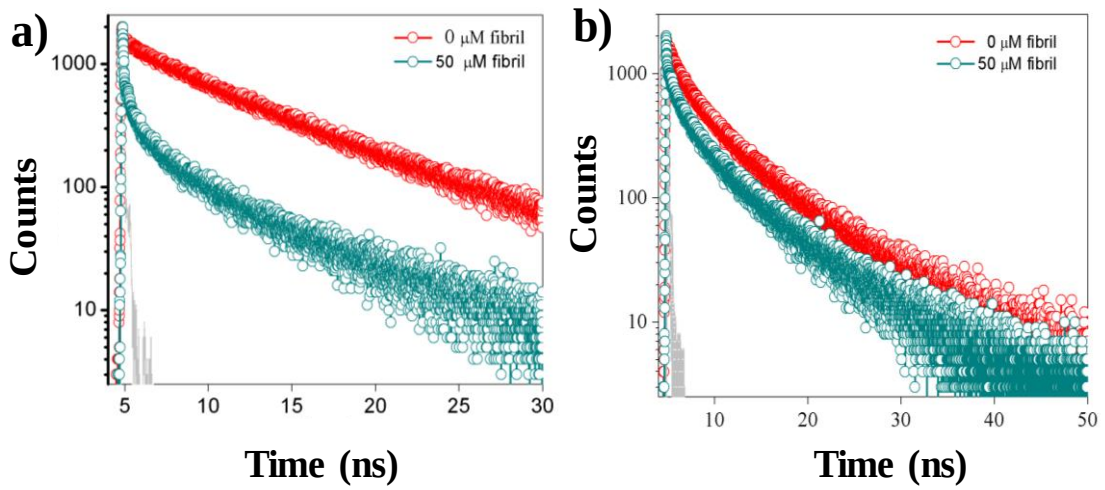

Appendix 2.4.3 Emission transient decay for DPAPMI (a, λ_{col} =550 nm) and CPMI (b, λ_{col} =510 nm) in the presence of 0 and 50 μM of insulin fibrils (λ_{ex} = 375).

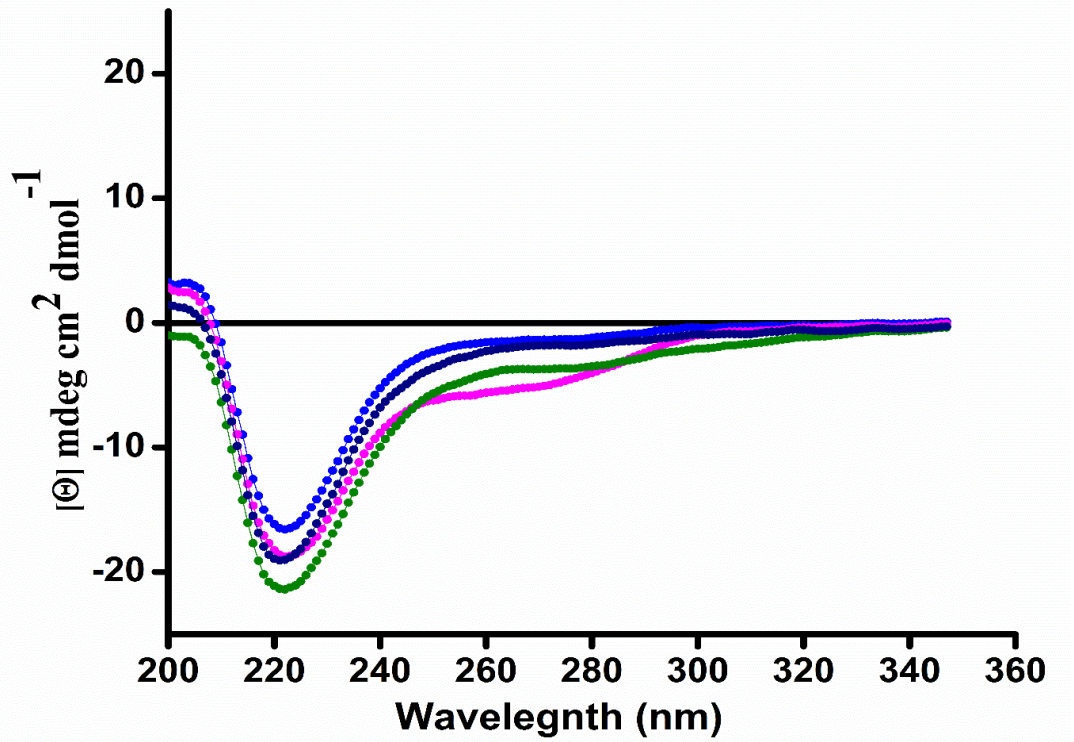

Appendix 2.4.4 CD spectra of 50 μM insulin fibrils (blue), 50 μM insulin fibrils with CPMI (black), 50 μM insulin fibrils with DPAPMI (green), and 50 μM insulin fibrils with DMAPMI (green) at pH 7.4.

Sensing and Modulation of Amyloid Fibrils by Photo switchable Organic Dots

Appendix Table.1 The Life time data plot of DPAPMI, CPMI and DMAPMI with and without fibrils.

Probes	[Fibril] (μM)	λ_{ex}	λ_{col}	A_1	τ_1 (ns)	A_2	τ_2 (ns)	A_3	τ_3 (ns)	$<\tau_{av}>^{\#}$ (ns)
DPAPMI	50	375	435	0.53	0.054	0.28	0.547	0.19	3.15	0.770
CPMI	50	375	420	0.40	0.181	0.35	1.834	0.26	6.54	2.38
DMAPMI	50	375	435	0.55	0.053	0.27	0.703	0.19	3.75	0.913

Appendix Table.2 The Life time data plot of DPAPMI, CPMI and DMAPMI with and without fibrils.

Probes	[Fibril] (μM)	λ_{ex}	λ_{col}	A_1	τ_1 (ns)	A_2	τ_2 (ns)	A_3	τ_3 (ns)	$<\tau_{av}>^{\#}$ (ns)
DPAPMI	0	375	550	0.44	0.220	0.33	2.10	0.24	6.73	2.350
	50	375	550	0.66	0.043	0.20	0.706	0.14	5.10	0. 863
CPMI	0	375	510	0.40	0.181	0.35	1.834	0.26	6.54	2.38
	50	375	510	0.27	0.403	0.34	2.50	0.39	1.03	4.99

$^{\#}\tau_{av} = a_1\tau_1 + a_2\tau_2 + a_3\tau_3$, we have considered the average lifetime values for explanation.

To investigate the generality over other biocompatible peptide/protein of this fluorescence probes, we have tested our designed probes with BSA fibrils. Which show that these probes are good sensors for the detection of BSA amyloid fibrils (Appendix. 2.4.5 a), b), c).

Sensing and Modulation of Amyloid Fibrils by Photo switchable Organic Dots

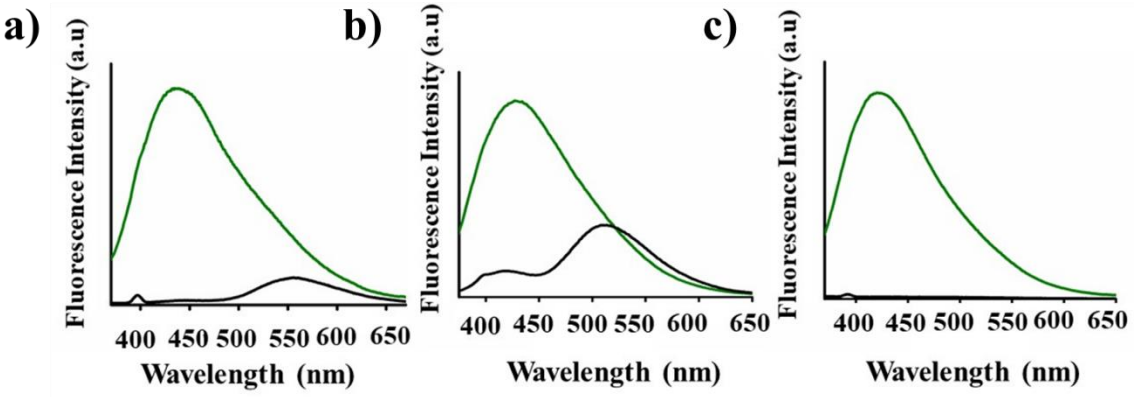

Appendix 2.4.5 a), b), c) Emission spectra (λex=350 nm) of DPAPMI, CPMI and DMAPMI, respectively in the presence of 0 (black) and 50 μM BSA fibrils (green).

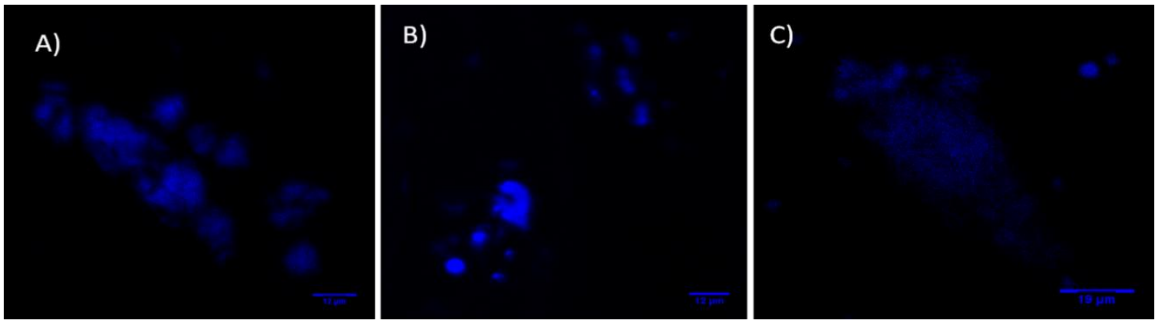

Appendix 2.4.6 Confocal images of fibrils stain with probes (λex = 405 nm) A) fibrils stain with DPAPMI, B) fibrils stain with CPMI, C) fibrils stain with DMAPMI.

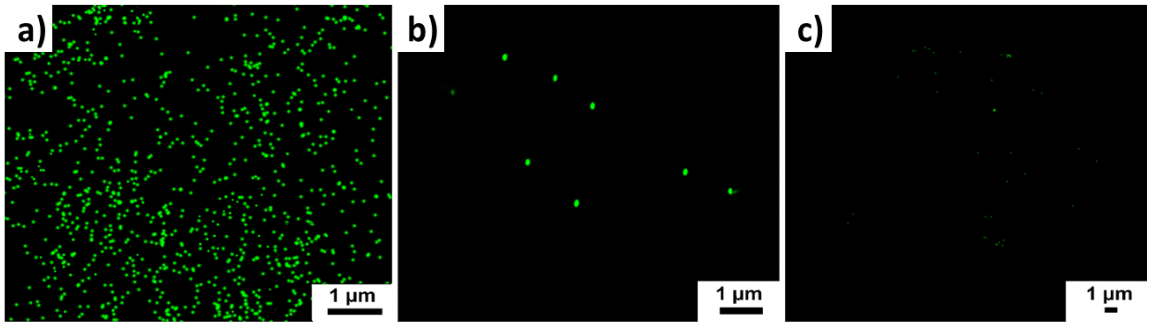

Sensing and Modulation of Amyloid Fibrils by Photo switchable Organic Dots

Appendix 2.4.7 d-STORM super-resolution microscopic images of insulin fibrils stained with our probe molecules. a) 4 μM DPAPMI in buffer, b) 4 μM CPMI in buffer and c) 4 μM DMAPMI in buffer.

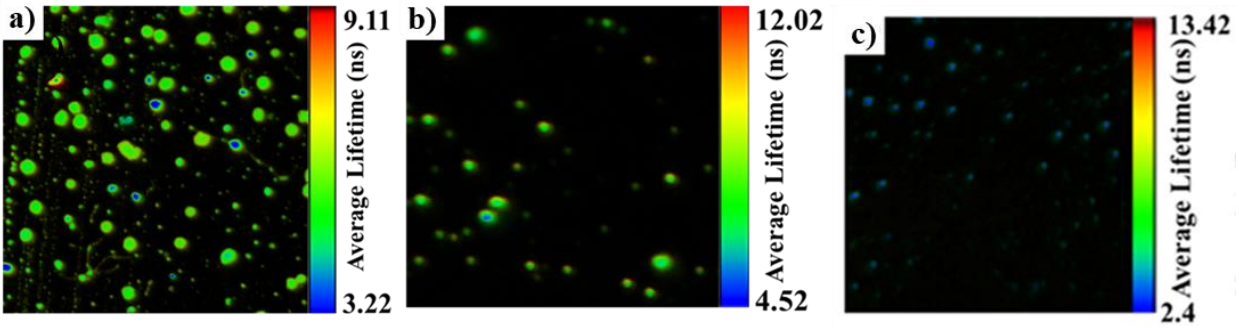

Appendix 2.4.8 FLIM-Z stack (400×400 pixel) images (λ_{ex} = 405 nm, λ_{col} =430-700 nm) of fluorescents probes with and without fibrils; a) DPAPMI in buffer b) CPMI in buffer c) DMAPMI in buffer.

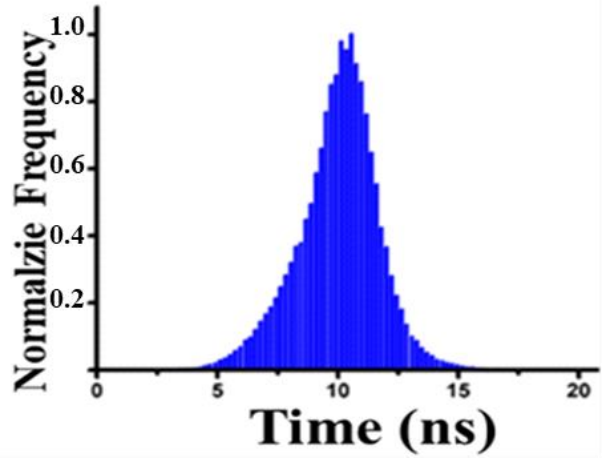

Appendix 2.4.9 Lifetime distributions of DMAPMI in the presence of insulin fibrils.

Appendix 2.4.10 Mipar calculation information: Recipe for image processing

MIPAR calculation is an image processing tool, which is performed in a right order and with the right setting, in order to identify the hiding features inside an image. Below is elaboration of some typical post processing steps that we have used in this study to create our required images.

1. *Scale calibration*: Allows us to calculate the pixel size in units of length rather than pixels.

2. *Highlight Lines*: Uses the Frangi filter to highlight linear-type features in the image. Combine with a threshold afterwards to select certain linear-type features.
3. *Fiber selection*: Balance fiber vs. background selection by selecting pixels based on whether they are above or below a certain pixel value. *Optimization of selection* was performed at this step *by selection matching algorithm.* It is perhaps the most critical yet less explored area of image processing to quantify the accuracy of the image-processing algorithm in question. MIPAR™ has provide with such facility where we can optimize parameter(s) to produce best similarity of the segmentation between the processed and the selected image.
4. *Uniform erosion*: Shrinks selection, if needed, by a specified number of pixels in all directions.
5. *Reject Features*: Which can remove or keep features based on a variety of shape and size metrics.
6. *Background*: Invert fiber selection.

Feature measurements: It allows one to measure a number of feature properties based on the features selected in the image. This includes, size parameters (area, area fraction, caliper diameter, etc.) m and shape parameters (roughness, aspect ratio, eccentricity, roundness, etc.)

Few important definitions:

Eccentricity: First an ellipse with same second moments as the feature was fitted. Then eccentricity is calculated as, $\sqrt{\left(1-\left(\frac{minor\ axis\ length}{major\ axis\ length}\right)^2\right)}$. It describes how elongated or circular each feature is. 0 is a perfect circle, 1 is a straight line.

Major axis length: Calculated as, $2\sqrt{2}\left(\sqrt{U_{xx}+U_{yy}+common}\right)$

Minor axis length: Calculated as, $2\sqrt{2}\left(\sqrt{U_{xx}+U_{yy}-common}\right)$

Common = $\sqrt{((U_{xx}-U_{yy})^2+4U_{xy}^2)}$

The second moments are calculated as: $U_{xx}=\frac{Sum(x^2)}{N}+1/12;\quad U_{yy}=\frac{Sum(y^2)}{N}+1/12;$

$U_{xy} = Sum(xy)/N$, where, x and y are the coordinate of each pixel in the feature, N is the number of pixels in each feature.

Roundness: Ratio of equivalent diameter to caliper diameter.

Aspect ratio: Ratio of major and minor axis length.

Roughness: Ratio of area of convex hull and area of each feature.

Area fraction: Count all the selected pixels in the reconstructed image and divides by the total number of pixels in the entire image.

Caliper diameter: largest line length that fits across each feature.

2.5 Experimental sections

2.5.1 Materials

Bovine insulin and bovine serum albumin purchased from Sigma Aldrich. The probe molecules DPAPMI, CPMI and DMAPMI were synthesized and characterized by our group.[42] HEK293 cells were cultured in DMEM medium supplemented with 10% FBS containing 100 units/mL penicillin, and 100 µg/mL streptomycin in a humidified CO_2 incubator maintained at 5% CO_2 and 37°C.

2.5.2 Preparation of fibrils

Insulin fibrils were prepared following the method reported by Sneideris et al Briefly, 2 mg/ml of insulin was dissolved in pH 1.6 aqueous solution (Using HCl), containing 100 mM NaCl and heated at 65^0 C for ~4 hrs without mechanical agitation.[45] The formation of fibril was confirmed by standard ThT fluorescence assay (Appendix 2.4.1).

2.5.3 Steady-state and time-resolved study

The steady-state absorption and emission spectra were recorded using a UV-Vis spectrophotometer (Shimadzu, UV-2600) and Fluoromax-4 Spectrofluorimeter (Horiba Jobin Yvon) respectively. Emission intensity decays were collected by time-correlated single photon counting (TCSPC) set-up from Horiba Jobin Yvon. Fluorescence signals were collected at the magic angle using MCP-PMT (Hamamatsu, Japan) detector. In time-resolved experiments, samples were excited with 375 nm diode laser and the instrument response function (IRF) of the

TCSPC set-up was ~50 ps. All spectroscopic measurements were performed at 25^0 C. Each study was performed multiple times with high reproducibility.

2.5.4 Far-UV circular dichroism (CD) study

CD spectra were recorded on a JASCO-810 circular dichroism spectrometer under a constant flow of nitrogen at 25 °C. Wavelength scans were recorded from 190 to 300 nm at 1 nm intervals in a 1 cm path length quartz cuvette. The final spectra were the average of three scans. Background spectra were subtracted from the collected data. Kinetic study was performed at 65^0 c in the presence and absence of probe molecules. The concentration of insulin and probe molecules were 50 μM and 8 μM, respectively. The percentage of THF contains in each solution is 0.8 %.

2.5.5 Fluorescence lifetime imaging study

FLIM measurements were Performed using a time-resolved confocal fluorescence microscope setup (Micro Time 200, Pico-Quant) equipped with an inverted microscope (Olympus IX 71) containing a water immersion objective (Olympus UplansApo NA 1.2 60X). A 405 nm pulsed diode laser (with FWHM 176 ps and repetition rate 20 MHz) was used as the excitation source. Fluorescence from the samples was collected by the same objective and passed through the dichroic mirror, filtered by a 430 nm long-pass filter. A 50-micrometer pinhole was placed after the filter. Single-photon avalanche photodiodes (SPADs) was used as a detector. Raster scanning was performed by the piezo controlled sample stage to obtain the images. The data acquisition and analysis were performed using the SymPhoTime software package provided by Pico-Quanta. The concentrations of the probes and fibrils were 4 μM and 50 μM, respectively. For FLIM measurement, 7 μL sample was added on the surface of microscopic cover glass and dried for 15 min. The concentrations of the probes and fibrils were 4 μM and 50 μM, respectively. The percentage of THF contains in each solution is 0.4%. Multiple images have been taken from different region of each sample at different magnifications.

2.5.6 d-STORM study

Super-resolution imaging was performed by ONI-super resolution microscopy. A 405 nm laser with 150 m power was used for photo-switching and to adjust the density of visible fluorophore. Samples (10 μL) of insulin fibrils with probe molecules and probe molecules without fibrils were placed on cover glass slips (18 mm 618 mm, 17±5 mm thickness) for measurements. The

percentage of THF contains in each solution is 0.4%. Multiple images have been taken from different region of each sample at different magnifications.

2.5.7 AFM study

The Atomic Force Microscopy (AFM) imaging was performed on the Key Sight 5500 AFM instrument (Agilent Technologies) under tapping mode with silicon nitride tip. The concentration of fibrils was 50 µM and the concentration of the probe was 8 µM. 7 µl sample was added on a silicon wafer and dried overnight. The dried sample was washed with water to remove the salt from the surface of the silicon wafer before AFM measurements. The percentage of THF contains in each solution is 0.8 %. Multiple images have been taken of each sample at different magnifications.

2.5.8 Cell viability assay

HEK293 cells (10000 cells/well in 200 µL DMEM media) were seeded in a 96 well plate and incubated overnight under cell culture conditions for cell attachment.[58] Subsequently, cells were incubated with varying concentrations of CPMI and DMAPMI (0.5, 1, 2, 4, 8, 16, 32, and 50 µM) containing 0.2% DMSO for 24 h under cell culture conditions. Cells incubated with DMEM media containing 0.2% DMSO were taken as controls. After the incubation, the cell culture media was replaced with 180 µL of DMEM media with 20 µL of MTT (3-[4, 5-dimethylthiazol-2-yl]-2, 5 biphenyl tetrazolium bromide) solution (3 mg/mL in PBS, filtered through 0.22-micron syringe filter), and the cells were further incubated for 3 h under cell culture conditions. Later, the DMEM media containing MTT was removed completely, and formazan crystals formed by the reduction of MTT were solubilized by adding 200 µL of DMSO. The intensity of the purple color generated was measured at 570 nm by using a plate reader (Varioskan Flash, Thermo Scientific). The cell viability graph was plotted from the relative optical density of treated samples to the corresponding control data (which is taken as 100%). Each value on the graph corresponds to the average of 5 technical replicates.

2.5.9 Kinetic data analysis from far-UV CD experiment

Time evolution of total fibrils mass concentration M(t) in the presence and absence of our probe molecules have been described by using integrated rate law.[51]

$$\frac{M(t)}{M(\infty)} = 1 - \alpha\left\{\left(\frac{(B_+ + C_+)}{B_+ + C_+ e^{kt}}\right)\left(\frac{B_- + C_+ e^{kt}}{B_- + C_+}\right)\right\}^{-\frac{k^2_\infty}{\kappa k'_\infty}} e^{-k_\infty t} \qquad (1)$$

Where,

$$B_\pm = (k_\infty \pm k'_\infty/(2\kappa)\ \ k'_\infty = \sqrt{2\kappa^2/[n_2(n_2+1)] + 2\lambda^2/n_c}$$

$$C_\pm = \pm\lambda^2/2\kappa^2 \qquad k'_\infty = \sqrt{{k_\infty}^2 - 4C_+C_-\kappa}$$

$$\kappa = \sqrt{2k_+k_2\, m(0)^{n_2+1}}$$

$$\lambda = \sqrt{2k_+k_n\, m(0)^{n_c}}$$

Where the kinetic parameters $B_\pm$, $C_\pm$, λ, κ and k'_∞ are function of the two-combination rate constants k_+k_n and k_+k_2

k_n = rate constant for primary nucleation

n_c = reaction order for primary nucleation

k_2 = rate constant for secondary nucleation.

n_2 = reaction order for secondary rate nucleation.

k_+ = rate constant for elongation.

m (0) = monomer concentration at time zero.

M (t) = Mass of the fibrils at time t.

M (∞) = Mass of the fibrils at time ∞.

The fits were done using the AmyloFit platform[51], which uses a basin-hopping algorithm to find the best fit to the data.

2.5.10 Image analysis using MIPAR™

The raw images obtained from the AFM/FLIM/d-storm studies were first scaled into similar dimensions (x and y axis) with a proper calibration factor. The images were then processed step-by-step with the help of MIPAR™ image processing tool[R2] which utilizes well trusted-and-tested in-built algorithms (detailed description can be found in the Appendix†) those are very specific to handle a fiber-like object within a 2D image. Briefly, we utilize Frangi filter[R1] (with setting thickness = 1 and strength = 2) combined with a threshold afterwards to highlight the linear-type feature in the image. A typical fibril detection tool was then applied to segment certain fibrous structures, based on whether they are below or above a certain pixel value. An automatic optimization process was run for the threshold pixel value to avoid any manual error. Finally, undesired features were rejected semi-automatically on the basis of their area and roundness factor being below a specified threshold value.

2.5.11 Kinetics study by fluorescence

Assays were conducted in Nunc 96 well polypropylene microplates, sealed with transparency film and incubated at 37 °C. Fluorescence kinetic was monitored using the Enspire Multimode Plate reader. The excitation and emission wavelength were fixed at 350 nm and 450 nm for the organic dots, 440 nm and 480 for the ThT nm. The concentrations of the organic dots and the fibrils were 50 µM and 350 µM. The concentration of ThT and fibrils were 25 and 350 µM. All the solutions were prepared at 50 mM phosphate buffer of pH 2 with 150 mM NaCl.

2.5.12 Analysis of fibril formation kinetics from fluorescence study

All aggregation curved were fitted to a sigmoidal function (equation 2) using origin 6.0 software package;

$$y = \frac{A_1 - A_2}{[1 + e^{t_{0.5}/\tau}]} + A_2 \qquad (2)$$

where t is the time, A_1 and A_2 are the initial and final values of the signal, respectively. The values of the parameters of the sigmoidal curve $t_{0.5}$ (half-time: time required to reach the half of the maximum of the signal A_2) and τ (magnitude of the signal) were determined by fitting the experiment data.

2.6 References

1. J. Hardy and D. J. Selkoe, *Science*, 2002, **297**, 353-356.

2. D. Eisenberg and M. Jucker, *Cell*, 2012, **148**, 1188-1203.

3. A. Åslund, C. J. Sigurdson, T. Klingstedt, S. Grathwohl, T. Bolmont, D. L. Dickstein, E. Glimsdal, S. Prokop, M. Lindgren, P. Konradsson, D. M. Holtzman, P. R. Hof, F. L. Heppner, S. Gandy, M. Jucker, A. Aguzzi, P. Hammarström and K. P. R. Nilsson, *ACS Chemical Biology*, 2009, **4**, 673-684.

4. C. A. Ross and M. A. Poirier, *Nature Medicine*, 2004, **10**, S10-S17.

5. J. R. Silveira, G. J. Raymond, A. G. Hughson, R. E. Race, V. L. Sim, S. F. Hayes and B. Caughey, *Nature*, 2005, **437**, 257-261.

6. M. T. Montojo, M. Aganzo and N. González, *J Huntingtons Dis*, 2017, **6**, 179-188.

7. S. Ogawa, T. M. Lee, A. R. Kay and D. W. Tank, *Proc Natl Acad Sci U S A*, 1990, **87**, 9868-9872.

8. Y.-H. Nai, M. Shidahara, C. Seki and H. Watabe, *Alzheimer's & Dementia: Translational Research & Clinical Interventions*, 2017, **3**, 542-552.

9. M. Ono and H. Saji, *Int J Mol Imaging*, 2011, **2011**, 543267-543267.

10. M. Shimojo, M. Higuchi, T. Suhara and N. Sahara, *Front Neurosci*, 2015, **9**.

11. K. L. De Jong, B. Incledon, C. M. Yip and M. R. DeFelippis, *Biophysical Journal*, 2006, **91**, 1905-1914.

12. Y.-L. Wang, C. Fan, B. Xin, J.-P. Zhang, T. Luo, Z.-Q. Chen, Q.-Y. Zhou, Q. Yu, X.-N. Li, Z.-L. Huang, C. Li, M.-Q. Zhu and B. Z. Tang, *Materials Chemistry Frontiers*, 2018, **2**, 1554-1562.

13. C. Mengchao, *Current Medicinal Chemistry*, 2014, **21**, 82-112.

14. H. Tong, K. Lou and W. Wang, *Acta Pharmaceutica Sinica B*, 2015, **5**, 25-33.

15. C. Peng, X. Wang, Y. Li, H.-W. Li and M. S. Wong, *Journal of Materials Chemistry B*, 2019, **7**, 1986-1995.

16. C. L. Teoh, D. Su, S. Sahu, S.-W. Yun, E. Drummond, F. Prelli, S. Lim, S. Cho, S. Ham, T. Wisniewski and Y.-T. Chang, *Journal of the American Chemical Society*, 2015, **137**, 13503-13509.

17. C. Chen, Z. Liang, B. Zhou, X. Li, C. Lui, N. Y. Ip and J. Y. Qu, *ACS Chemical Neuroscience*, 2018, **9**, 3128-3136.

18. J. Qin, J. S. Park, D. G. Jo, M. Cho and Y. Lee, *Sensors and Actuators B: Chemical*, 2018, **273**, 1593-1599.

19. M. Ono, H. Watanabe, H. Kimura and H. Saji, *ACS chemical neuroscience*, 2012, **3**, 319-324.

20. L. Civitelli, L. Sandin, E. Nelson, S. I. Khattak, A.-C. Brorsson and K. Kågedal, *Journal of Biological Chemistry*, 2016, **291**, 9233-9243.

21. D. A. Yushchenko, J. A. Fauerbach, S. Thirunavukkuarasu, E. A. Jares-Erijman and T. M. Jovin, *Journal of the American Chemical Society*, 2010, **132**, 7860-7861.

22. A. K. Mora, P. K. Singh, B. S. Patro and S. Nath, *Chemical Communications*, 2016, **52**, 12163-12166.

23. M. Ono, H. Watanabe, H. Kimura and H. Saji, *ACS Chemical Neuroscience*, 2012, **3**, 319-324.

25. N. H. Mudliar and P. K. Singh, *Chemical Communications*, 2019, **55**, 3907-3910.

26. N. H. Mudliar, B. Sadhu, A. M. Pettiwala and P. K. Singh, *The Journal of Physical Chemistry B*, 2016, **120**, 10496-10507.

27. W. Fu, C. Yan, Z. Guo, J. Zhang, H. Zhang, H. Tian and W.-H. Zhu, *Journal of the American Chemical Society*, 2019, **141**, 3171-3177.

28. Y. Hong, L. Meng, S. Chen, C. W. T. Leung, L.-T. Da, M. Faisal, D.-A. Silva, J. Liu, J. W. Y. Lam, X. Huang and B. Z. Tang, *Journal of the American Chemical Society*, 2012, **134**, 1680-1689.

29. J. Luo, Z. Xie, J. W. Y. Lam, L. Cheng, H. Chen, C. Qiu, H. S. Kwok, X. Zhan, Y. Liu, D. Zhu and B. Z. Tang, *Chemical Communications*, 2001, DOI: 10.1039/B105159H, 1740-1741.

30. Y. Hong, J. W. Y. Lam and B. Z. Tang, *Chemical Communications*, 2009, DOI: 10.1039/B904665H, 4332-4353.

31. J. Mei, N. L. C. Leung, R. T. K. Kwok, J. W. Y. Lam and B. Z. Tang, *Chemical Reviews*, 2015, **115**, 11718-11940.

32. D. D. La, S. V. Bhosale, L. A. Jones and S. V. Bhosale, *ACS Applied Materials & Interfaces*, 2018, **10**, 12189-12216.

33. F. Hu and B. Liu, *Organic & Biomolecular Chemistry*, 2016, **14**, 9931-9944.

34. T. G. Hwang, J. Y. Kim, J. W. Namgoong, J. M. Lee, S. B. Yuk, S. H. Kim and J. P. Kim, *Photochemical & Photobiological Sciences*, 2019, **18**, 1064-1074.

35. C. Zhang, S. Jin, K. Yang, X. Xue, Z. Li, Y. Jiang, W.-Q. Chen, L. Dai, G. Zou and X.-J. Liang, *ACS Applied Materials & Interfaces*, 2014, **6**, 8971-8975.

36. L. Yan, Y. Zhang, B. Xu and W. Tian, *Nanoscale*, 2016, **8**, 2471-2487.

37. N. Pradhan, D. Jana, B. K. Ghorai and N. R. Jana, *ACS Applied Materials & Interfaces*, 2015, **7**, 25813-25820.

38. W. Fu, C. Yan, Y. Zhang, Y. Ma, Z. Guo and W.-H. Zhu, *Frontiers in Chemistry*, 2019, **7**.

39. H. Shi, R. T. K. Kwok, J. Liu, B. Xing, B. Z. Tang and B. Liu, *Journal of the American Chemical Society*, 2012, **134**, 17972-17981.

40. C. Y. Y. Yu, H. Xu, S. Ji, R. T. K. Kwok, J. W. Y. Lam, X. Li, S. Krishnan, D. Ding and B. Z. Tang, *Advanced Materials*, 2017, **29**, 1606167.

41. T. Gunnlaugsson, *Nature Chemistry*, 2015, **8**, 6.

42. B. Roy, M. C. Reddy and P. Hazra, *Chemical Science*, 2018, **9**, 3592-3606.

43. M. Ahmed, J. Davis, D. Aucoin, T. Sato, S. Ahuja, S. Aimoto, J. I. Elliott, W. E. Van Nostrand and S. O. Smith, *Nature Structural & Molecular Biology*, 2010, **17**, 561-567.

44. J. C. Stroud, C. Liu, P. K. Teng and D. Eisenberg, *Proc Natl Acad Sci U S A*, 2012, **109**, 7717-7722.

45. S. Trikha and A. M. Jeremic, *PLOS ONE*, 2013, **8**, e73080.

46. E. Kachooei, A. A. Moosavi-Movahedi, F. Khodagholi, H. Ramshini, F. Shaerzadeh and N. Sheibani, *PLOS ONE*, 2012, **7**, e41344.

47. T. Sneideris, D. Darguzis, A. Botyriute, M. Grigaliunas, R. Winter and V. Smirnovas, *PLOS ONE*, 2015, **10**, e0136602.

48. J. Pansieri, M. Gerstenmayer, F. Lux, S. Mériaux, O. Tillement, V. Forge, B. Larrat and C. Marquette, *Nanomaterials*, 2018, **8**.

49. C. Yongmin, L. Gang Ho, K. Tae-Jeong and C. Kwon-Seok, *Current Topics in Medicinal Chemistry*, 2013, **13**, 434-445.

50. J. H. Choi, B. C. H. May, H. Wille and F. E. Cohen, *Biophysical Journal*, 2009, **97**, 3187-3195.

51. G. Meisl, J. B. Kirkegaard, P. Arosio, T. C. T. Michaels, M. Vendruscolo, C. M. Dobson, S. Linse and T. P. J. Knowles, *Nature Protocols*, 2016, **11**, 252-272.

52. J. Habchi, P. Arosio, M. Perni, A. R. Costa, M. Yagi-Utsumi, P. Joshi, S. Chia, S. I. A. Cohen, M. B. D. Müller, S. Linse, E. A. A. Nollen, C. M. Dobson, T. P. J. Knowles and M. Vendruscolo, *Science Advances*, 2016, **2**, e1501244.

53. S. I. A. Cohen, S. Linse, L. M. Luheshi, E. Hellstrand, D. A. White, L. Rajah, D. E. Otzen, M. Vendruscolo, C. M. Dobson and T. P. J. Knowles, *Proceedings of the National Academy of Sciences*, 2013, **110**, 9758-9763.

54. T. P. J. Knowles, C. A. Waudby, G. L. Devlin, S. I. A. Cohen, A. Aguzzi, M. Vendruscolo, E. M. Terentjev, M. E. Welland and C. M. Dobson, *Science*, 2009, **326**, 1533.

55. S. I. A. Cohen, M. Vendruscolo, C. M. Dobson and T. P. J. Knowles, *J Chem Phys*, 2011, **135**, 065106-065106.

56. F. A. Ferrone, J. Hofrichter and W. A. Eaton, *Journal of Molecular Biology*, 1985, **183**, 611-631.

57. S. L. Shammas, T. P. J. Knowles, A. J. Baldwin, C. E. Macphee, M. E. Welland, C. M. Dobson and G. L. Devlin, *Biophysical journal*, 2011, **100**, 2783-2791.

58. Y. Porat, A. Abramowitz and E. Gazit, *Chemical Biology & Drug Design*, 2006, **67**, 27-37.

R1. Ian C. Campbell, Baptiste Coudrillier, Johanne Mensah, Richard L. Abel and C. Ross Ethier 2015Automated segmentation of the lamina cribrosa using Frangi's filter: a novel approach for rapid identification of tissue volume fraction and beam orientation in a trabeculated structure in the eye. *J. R. Soc. Interface*. 12, 20141009, 1-9

R2. Sosa, J. M.; Huber, D. E.; Welk, B.; Fraser, H. L. Development and application of MIPAR™: a novel software package for two- and three-dimensional microstructural characterization. *Integr. Mater. Manuf. Innov.* **2014**, *3*, 1−18.

Sensing and Modulation of Amyloid Fibrils by Photo switchable Organic Dots

Chapter 3

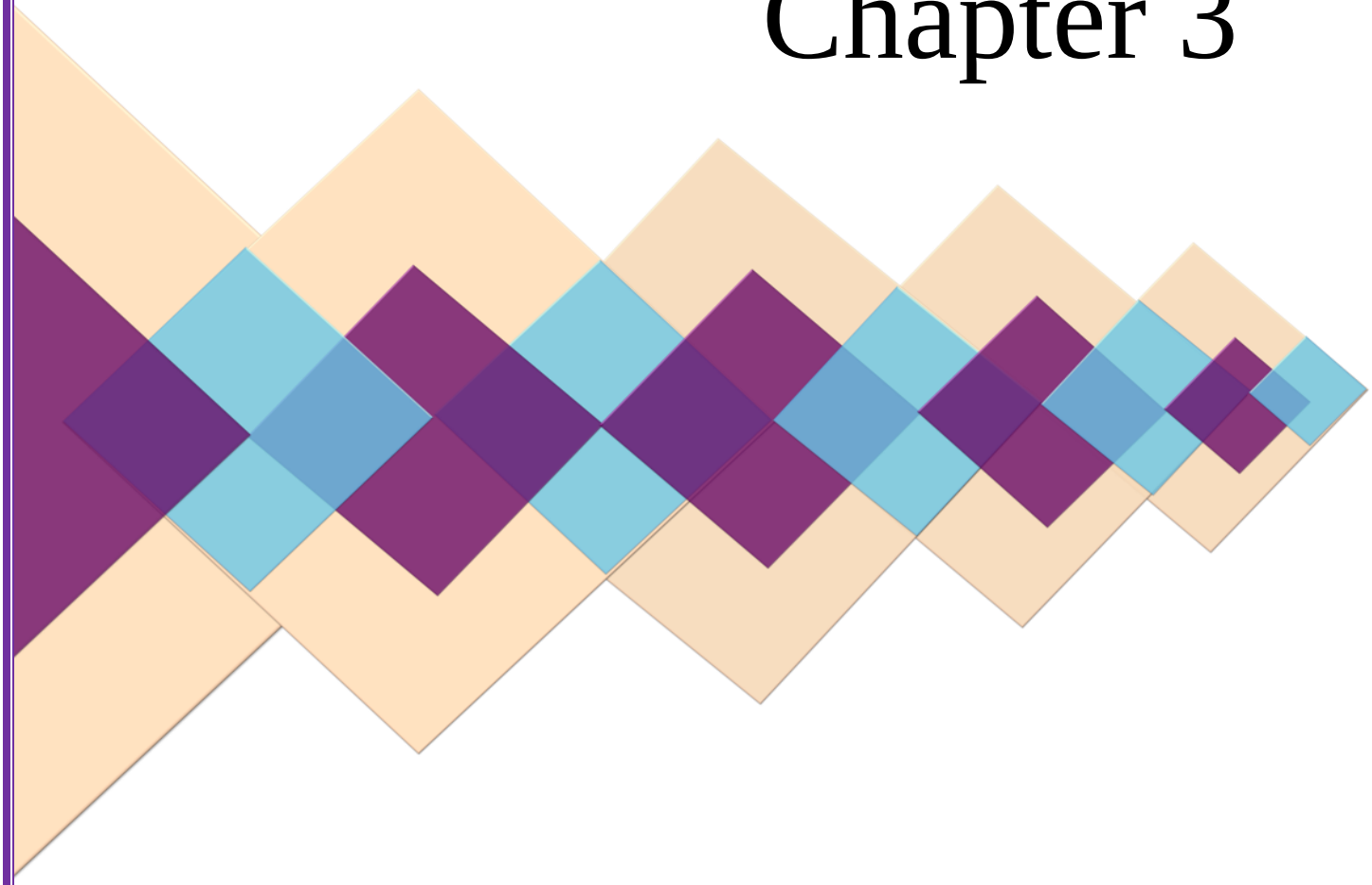

Early Stage Detection of Alpha-Synuclein Aggregation Using Curcumin Based Molecule

Early-Stage Detection of Alpha-Synuclein Aggregation using Curcumin Based Molecule

3.1 Introduction

Understanding the mechanisms of protein misfolding and aggregation is vital to combat the several neurological disorders such as Parkinson's, Alzheimer's and Prion disease etc[1-4]. The conversion of soluble proteins into amyloid deposits known as the main culprits for several neurological disorder which are mainly characterized by a common cross-β core structural motif.[5] Recent past scientist has come across to the conclusion that the transient soluble oligomeric intermediates, which arise during the pathway of fibril's formation process are strongly connected in cytotoxicity and ultimately death of a neuron cell.[6] Due to the heterogeneous size and structure of this oligomers and the rare abundance relative to monomeric protein makes it extremely difficult to characterized it using conventional biophysical tools.[7]

However, intrinsic fluorescence study has been used so far to examine the early-stages of β-amyloid aggregation by combining fluorescence decay measurements of the β-amyloid intrinsic tyrosine and molecular dynamic simulations.[8] Unfortunately, this approach has some serious drawbacks namely need for high aromatic amino acid content in the biomolecules of interest. Therefore, an alternative technique such as fluorescents probes allows us to direct visualization of single aggregates. So far thioflavin-T (ThT) is claimed to be main tools for studying fibrils formation, a benzothiazole salt and molecular rotor dye, extensively used as the gold-standard in the aggregation process from a long time.[9-15] The fluorescence intensity of ThT enhanced by several orders upon binding with the β-sheet structures making it a sensitive and efficient reporter of amyloid.[16] However, because of low molar extinction coefficient and low quantum yield and poor binding affinity of ThT mean it is poorly suitable for the detection of smaller oligomeric species particularly in biological sample.

Therefore, a smart biocompatible probe is urgently needed with improved photophysical and binding properties to detect and characterize the formation of these oligomeric species and their role in the pathogenesis and neurodegenerative disorders. To address this limitation, we have designed a novel derivative of curcumin, that in its binding and optical characteristics switching its fluorescence intensity upon binding to β-sheet contain species.

3.2 Results and Discussion

The main focused of this work to investigate the potential of CR-3 for the detection of the oligomeric phase of α-Synuclein (α-Syn). Given the lack of information about the fluorescence properties of CR-3, we first carried out a photophysical behaviours of CR-3 in different solvent. Then we have checked the photophysical properties of CR-3 in physiologically relevant aqueous conditions. Depending on the characterization of CR-3 in this environment we are going to report a detailed study on its fluorescence response as protein probe by using the fibrils like aggregates of α-synuclein and Aβ.

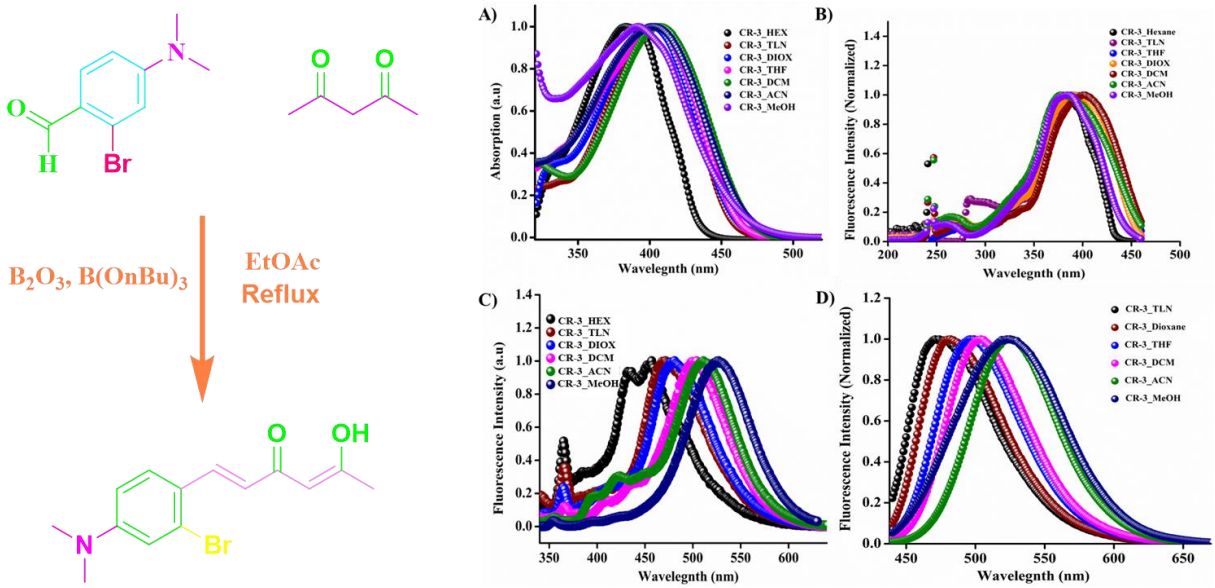

Figure 3.1 Schematic synthesis and optical properties of CR-3. A), B) Absorption, Excitation spectra (λ_{em} =550 nm). C), D) Solvatochromism study of CR-3 excited at different wavelength (λ_{ex}= 330 nm, 405 nm). (TLN: Toluene, DIOX: Dioxane, THF: Tetrahydro furan, DCM: Dichloromethane, ACN: Acetonitrile, MeOH: Methanol).

Early-Stage Detection of Alpha-Synuclein Aggregation using Curcumin Based Molecule

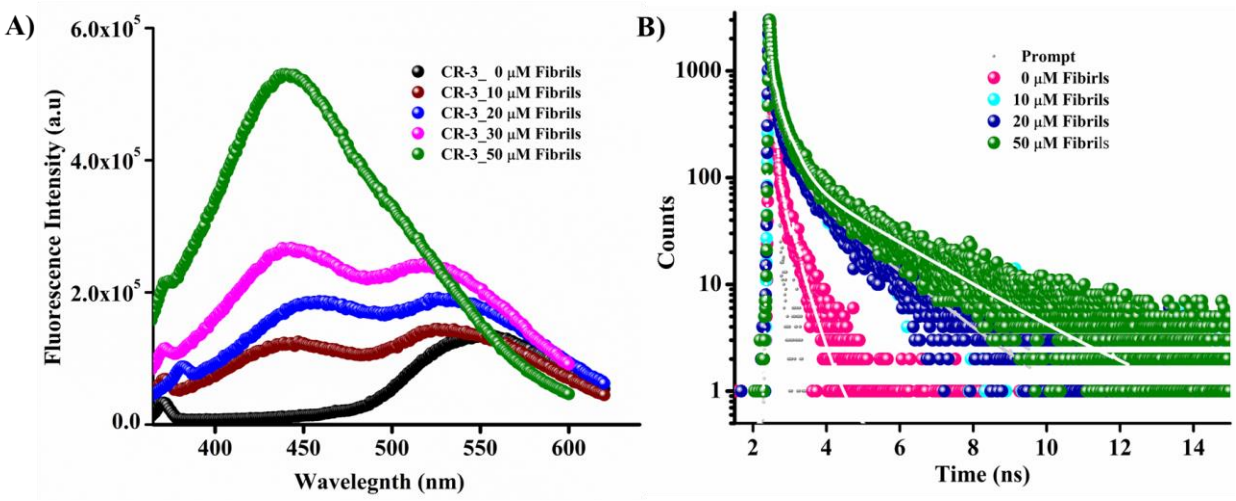

Figure 3.2 A) Emission spectra of 8 μM CR-3 (λ_{ex}= 330 nm) with different α-Syn fibrillar aggregates concentration. B) Transient emission decay (λ_{ex} = 375 nm, λ_{em} = 550 nm) of CR-3 in the presence of different concentration of α-synuclein fibrils.

3.2.1 Photophysical behaviours of CR-3 in physiologically relevant solvent

At first, we have thoroughly studied the photophysical properties of CR-3. The UV-visible absorption peaks of CR-3 recorded in the presence of increasing solvent polarity. The absorption of peak maxima of CR-3 does not alter with the changing polarity of the solvent. Furthermore, we have recorded the emission spectra of this molecule with increasing solvent polarity. The steady state emission spectra of CR-3 exhibit low intensity at ~ 450 nm in nonpolar solvent like hexane and exhibits gradual red-shift and enhancement of fluorescence emission with the increment of solvent polarity. This extreme red shift in emission maxima arises because of stabilization of charge transfer state (CT**).** Surprisingly in the acetonitrile solvent medium we have observed a peak ~440 nm (λ_{ex} = 350 nm), but in the case of MeOH we have not observed any peak around there. Therefore, we have speculated that some excited state phenomenon like intramolecular proton transfer is happening in the presence of acetonitrile solvent medium. In order to confirm that, we have performed time-resolved study (Appendix 3.2). The analysis of the lifetime decay profile in the presence of different solvent like ACN, MeOH and water which gives two lifetime components but there was no growth component, suggesting that there was no excited state dynamic.

3.2.2 Steady-state emission and Time resolved study

The emission spectrum of CR-3 has been measured with increasing concentration of α-Syn fibrils at two different wavelengths presented in Figure.3.2A It is observed that the emission spectra of CR-3 in absence of fibrils exhibit two peaks one at ~450 nm and another at ~550 nm when excited at 330 nm, however it shows only one peak at ~550 nm when excited at 420 nm (Appendix 3.2). This suggests that the peak appeared at 550 nm is attributed to CT state and the high energy peak at ~450 nm corresponds to LE state. Interestingly, with increasing concentration of alpha synuclein fibrils, the intensity of LE peak is increasing at the cost of CT peak, and at higher concentration of alpha synuclein fibrils, the emission spectra become broad LE peak become sole visible peak. Most importantly, this LE peak position almost remains constant suggests that this state is not sensitive to surrounding environmental polarity. This steady state results indicates that our probe CR-3 is preferentially locating in hydrophobic environment of the fibril, as a result the LE state of the molecule is getting stabilized over CT state. Overall, the steady state results suggest that CR-3 can act as an efficient fluorescence sensor for the amyloid fibrils. Specifically, the large shift in the emission maxima is advantageous for the fluorescent imaging application due to the relatively low background signal.

The time-resolved fluorescence measurement was performed to understand the fate of the charge transfer state in presence of fibrillary environment (Figure 3.2B). The average lifetime of the CT state of CR-3 slightly increases upon the addition of increasing concentration of α–syn fibrils switching in fluorescence emission. This increment of the lifetime component suggesting that the fraction of molecule remain in charge transfer state getting stabilized with varying concentration of the α-syn fibrils because of restriction of single molecular rotation around the fibrillar matrix.

We next used CR-3 to monitor aggregation kinetic of α-Syn. As it is well known that purified α-Synuclein aggregates via a three-step process: formation of soluble oligomers, growth of amyloid fibers, and maturation of fibers. Although ThT can only detects growth and maturation of fibers but its fail to detect soluble oligomers that are increasingly speculated to be the toxic species. By contrast, fluorescence of CR-3 started to increase at 1 h (Figure 3.4A). At this time point, formation of oligomers is reported. Moreover, a second phase of fluorescence increase was observed ~20 h and leveled off at these signal changes coincide with the time points of the fiber's growth as

observed by ThT. So, these data suggesting that CR-3 can detect the multiple stages of protein aggregation. This interesting features of this kind of probes coming from its unique environmental sensitivity. The changes of environment polarity around the CR-3 during the course of aggregation is conveniently expressed as the early rise of fluorescence signal.

These signal changes match with the timepoints of fiber growth and plateau phase observed by ThT. Therefore, these data strongly indicate that CR-3 can detect multiple stages of protein aggregation. In addition to α–synuclein we also demonstrated CR-3 could detect aggregates formed by Aβ–42 known to be main culprit for Alzheimer's disease.

After that we monitor the aggregation kinetic of α-synuclein using time resolved fluorescence manually to map the evolution of the heterogeneity of the system. Therefore, the average fluorescence lifetime of CR-3 with α–synuclein recorded with different time intervals, (λ_{ex} = 375 nm, λ_{col} = 450 nm, 550 nm).

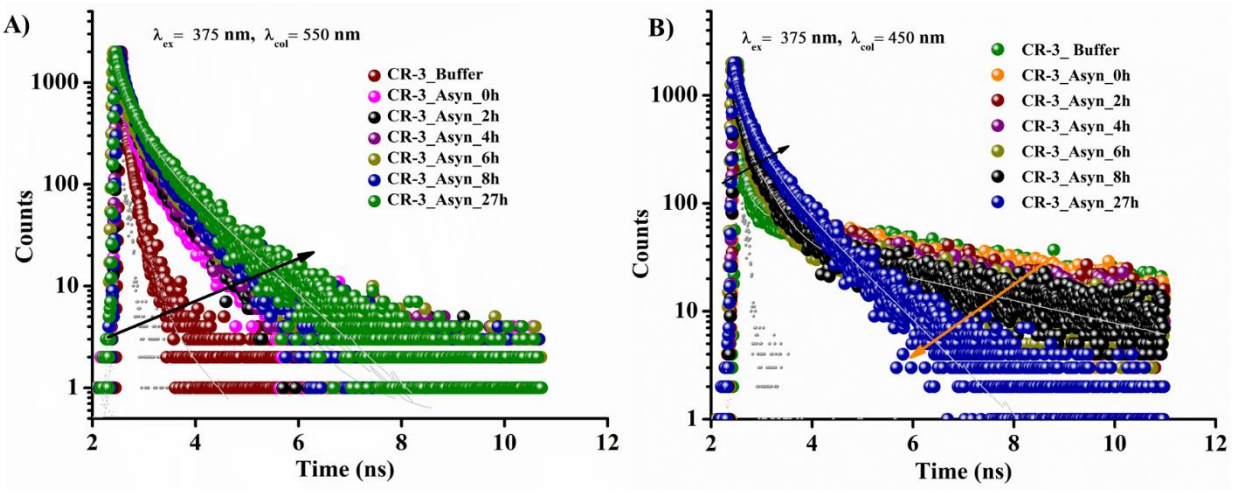

Figure 3.3 Lifetime decay traces of CR-3 monitor at different timepoint collected at two different wavelengths (λ_{ex}= 450 nm, 550 nm).

At the onset of incubation, the sample displayed fluorescence emission from CR-3 with native α-synuclein (λ_{ex} = 375 nm, λ_{col} = 450 nm) and the recorded decay trace fits to a tri-exponential decay function having an ~75% fast component (<50 ps) with ~3% of the slower ~8.9 ns

component and 22 % moderate component ~0.78 ns. After 2h of incubation, the contribution of medium component increased slightly ~5% along with slight decreased of fast component ~ 4%. Beyond 4h we observed the significant heterogeneity on the lifetime distribution. Gradually, the contributions of the faster components decreased slowly with time, whereas the contributions from the faster components decreased, overall, the average lifetime of CR-3 decreased from 500 ps to 405 ps.

On the other hand, the fluorescence emission from CR-3 with native α-synuclein (λ_{ex} = 375 nm, λ_{col} = 550 nm) and the fitted decay trace to a tri-exponential function having ~86 % fast component (~133 ps) with 2% (~397 ps). But after 2h of incubation, the contribution of fast component decreased abruptly (~44 %) along with significant increments of the contribution of medium component (~32%). Beyond 4h we observed significant heterogeneity on the lifetime distribution. Gradually, the contribution of the faster components decreased slowly with time and overall, the average lifetime of CR-3 increased significantly.

It is indicated that transformation of the random coil to β-sheet rich protofibril/fibrillar structure do pass through various structural rearrangement by which it gradually gets richer in β-sheet content and increases the internal order in protein structure. Thus, the subtle changes seen lifetime patterns at a much earlier certainly would indicate presence of precursors, even to the protofibrils, having a rigid micro-environment for binding CR-3.

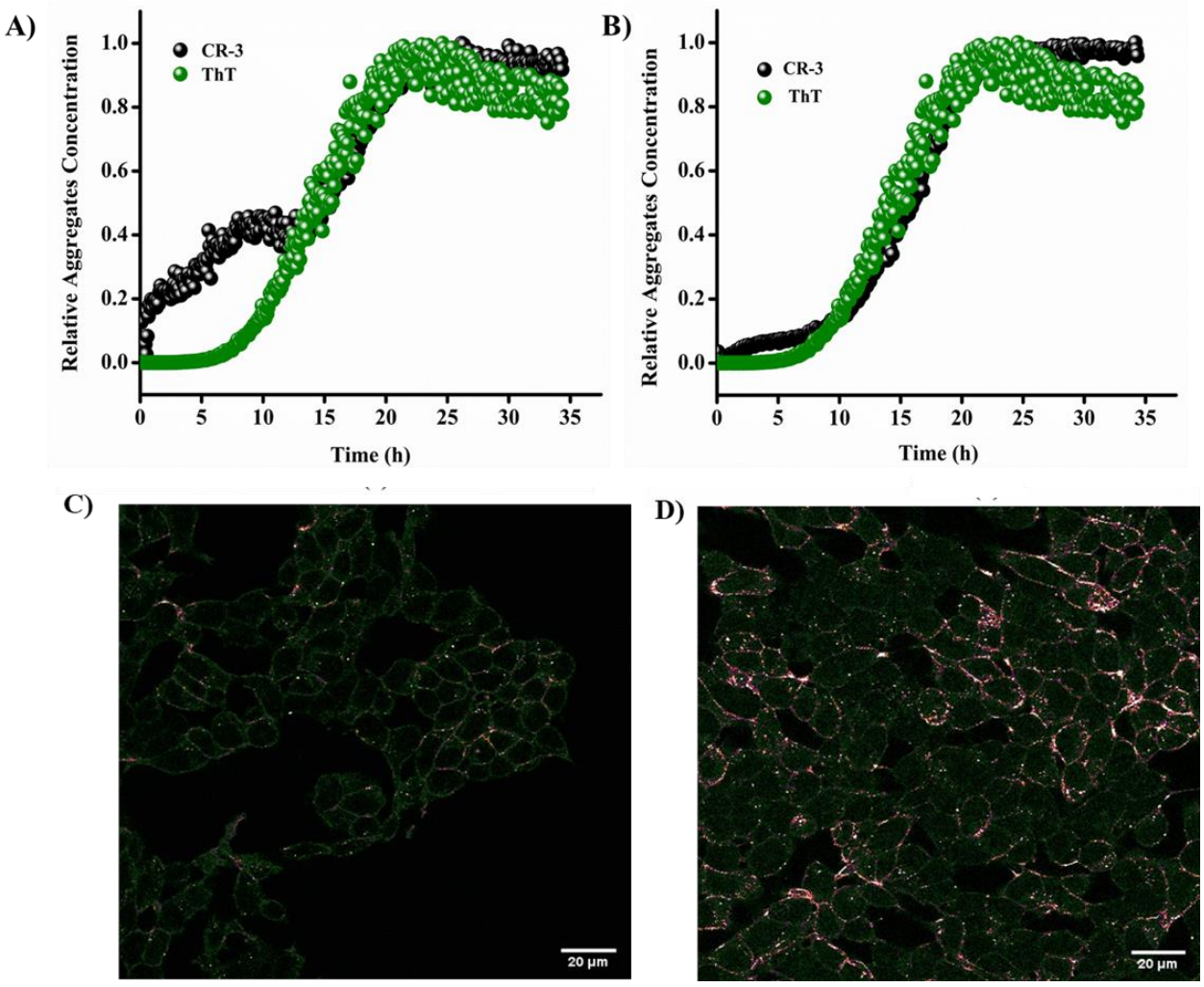

Figure 3.4 A) Kinetics of α-Syn amyloid fibril formation monitored by CR-3 (λ_{ex}=350) nm and ThT (λ_{ex}=440 nm). B) Kinetics of α-Syn amyloid fibril formation monitored by CR-3 (λ_{ex}= 440 nm) and ThT (λ_{ex}= 440 nm). C) α-Syn Oligomers detection on the surface of neuro-blastoma (SH-SY5Y) cell lines in the presence of ThT. D) α-Syn oligomers detection on the surface of neuro-blastoma (SH-SY5Y) cell lines in the presence of CR-3.

Similarly, the emission intensity recorded at 550 nm with respect to time displayed a sigmoidal increase with a long lapse of time. In other words, from the present perspective of an early stage of fibrils detection, the low response of CR-3 emission in the initial region is much disappointing. On the other hand, as the rigidity of the micro-environment around the dye radically changes on

the course of fibrils formation, we expected the dynamic changes of photo physics of CR-3, which will get reflected in its fluorescence lifetime.

3.2.3 In-vivo detection of oligomers in neuro-blastoma cell lines

We then investigated whether our synthesized probe can detect the α-synuclein oligomers on the surface of human SH-SY5Y neuroblastoma cells. In order to that we mixed oligomers with our probe molecule and ThT and incubate with human SH-SY5Y neuroblastoma cell lines separately. After that we record the image using confocal microscopy. The images were scanned at apical planes to detect oligomers (Red channel) interacting with cellular surface (Green channel). Overall, we observed that the oligomers are more prominently visible in the presence of our probe compare to Thioflavin-t. In short, we can conclude that our probe molecules can be useful for in-vivo detection of oligomers in cell.

3.2.4 Docking Study

The knowledge of binding sites of the probes is very important to understand their sensory activity and for future sensor development. Therefore, we performed the blind molecular docking studies to find out the location of CR-3 in α-synuclein fibrils. The docking study suggesting that only hydrogen bonding interaction operating between CR-3 and the amino acids of α-synuclein amyloid fibrils. It was found that the binding of CR-3 in the amyloid fibrils was mainly dominated by hydrogen bond interaction between the carbonyl group of CR-3 and the nearby threonine group and hydroxyl group of CR-3 and nearby carboxylic group of glutamic acid.

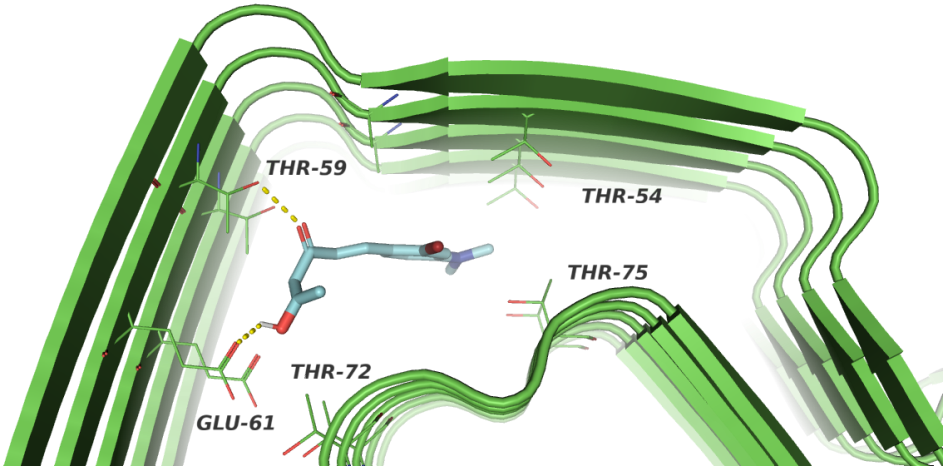

Figure 3.5 Binding of CR-3 with α-synuclein fibrils.

3.3 Conclusion

We have synthesized and evaluated CR-3, a novel probe with unique photophysical and binding properties that may prove superior to ThT in future applications. CR-3 can detect early-stage species in the aggregation of α-synuclein proteins at bulk and aggregates levels and the binding properties. Apart from this the evaluation of multiple lifetime component of CR-3 in course aggregation of α-synuclein can map the heterogeneity of the system. Additionally, CR-3 exhibits good compatibility towards oligomers detection in cells. Overall, the diverse quality of CR-3 pointing towards better quality probe compare to ThT in future application.

3.4 Appendix Section

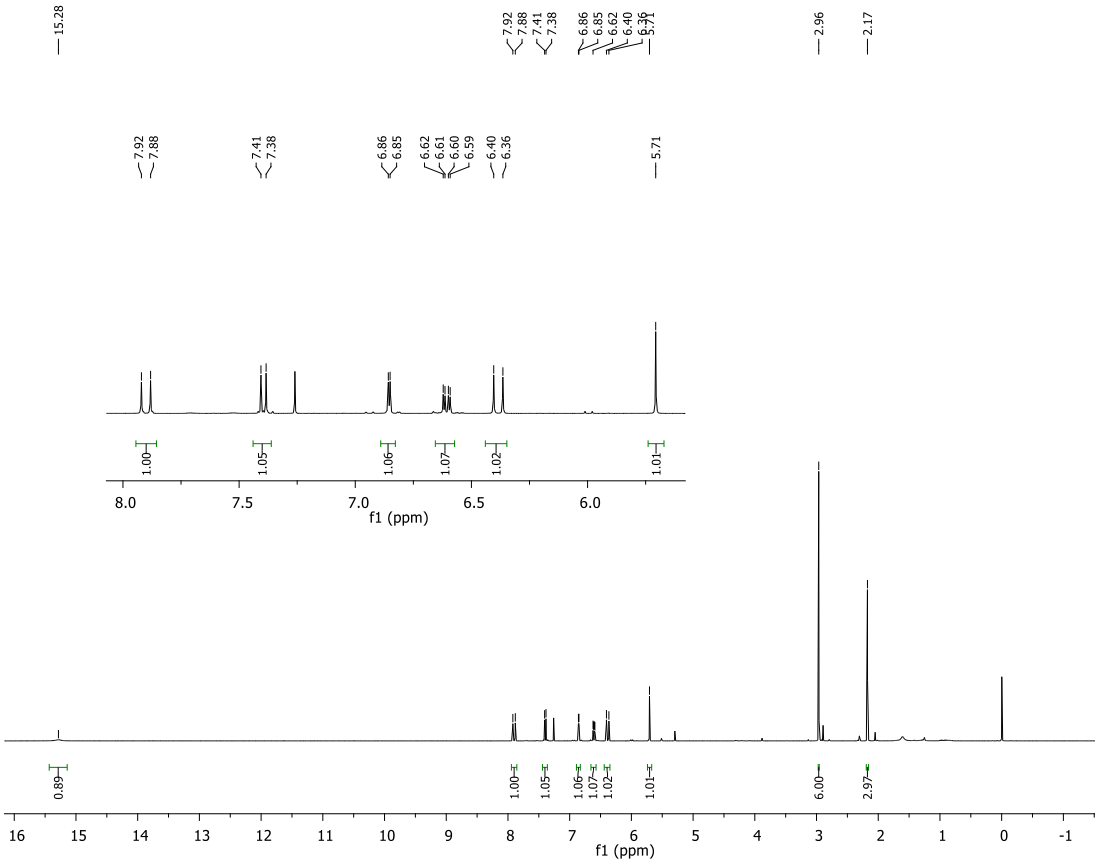

Appendix 3.1. N.M.R Spectra of CR-3.

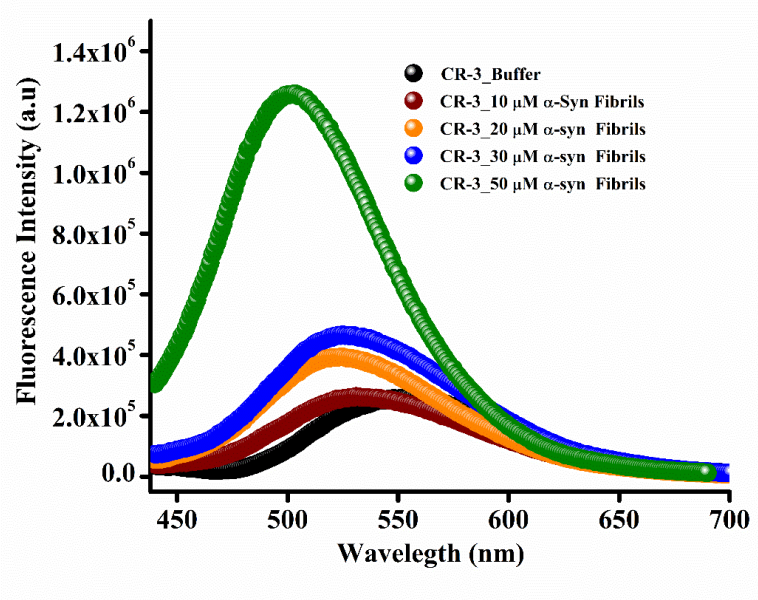

Appendix 3.2 Emission spectra of 8 μM CR-3 ((λ_{ex}=420 nm) with different concentration of α-synuclein.

Appendix Table 1. Lifetime decay parameter of CR-3 (λ_{ex} = 375 nm, (λ_{col} = 550 nm) in the presence 80 μM of α-Synuclein at different time point of aggregation.

Sample	α_1	τ_1 (ps)	α_2	τ_2 (ps)	α_3	τ_3 (ps)	τ_{avg}
Buffer	0.04	487	0.01	9440	0.95	41	
80 μM a-Syn_0h	0.22	782	0.03	8900	0.75	82	513
80 μM a-Syn_2h	0.27	715	0.03	7150	0.71	121	512
80 μM a-Syn_4h	0.30	718	0.03	6530	0.67	125	517
80 μM a-Syn_6h	0.30	578	0.04	4460	0.61	94	421
80 μM a-Syn_8h	0.33	635	0.04	4100	0.63	123	441
80 μM a-Syn_22h	0.30	579	0.03	3870	0.67	134	368
80 μM a-Syn_27h	0.29	644	0.03	4720	0.68	134	405

Early-Stage Detection of Alpha-Synuclein Aggregation using Curcumin Based Molecule

Appendix Table 2. Lifetime decay parameter of CR-3 (λ_{ex} = 375 nm, (λ_{col} = 450 nm) in the presence 80 μM of α-Synuclein at different time point of aggregation.

Sample	α_1	τ_1 **(ps)**	α_2	τ_2 **(ps)**	α_3	τ_3 **(ps)**	τ_{avg}
Buffer	0.25	311	0.01	935	0.75	57	34
80 μM a-Syn_0h	0.12	364	0.02	1580	0.86	84	133
80 μM a-Syn_2h	0.46	397	0.10	1630	0.44	109	459
80 μM a-Syn_4h	0.40	487	0.13	1730	0.47	169	502
80 μM a-Syn_6h	0.44	520	0.15	1850	0.41	158	572
80 μM a-Syn_8h	0.48	470	0.15	1730	0.37	144	544
80 μM a-Syn_22h	0.41	553	0.17	1830	0.42	146	600
80 mM a-Syn_27h	0.32	659	0.20	1840	0.48	235	692

Appendix Table 3. Lifetime decay parameter of CR-3 (λ_{ex} = 375 nm, (λ_{col} = 450 nm) in the presence of different concentration α-synuclein.

Sample	α_1	$\tau_{1\ (ps)}$	α_2	τ_2	α_3	$\tau_{3\ (ps)}$	τ_{av}	χ
0 μM	---	---	---	---	---	---		1.03
50 μM	0.89	68 ps	0.09	685 ps	0.01	4.48 ns	194	1.37
20 μM	0.90	57 ps	0.09	658 ps	0.01	3.71 ns	154	1.44
10 μM	0.94	49 ps	0.04	676 ps	0.02	3.27 ns		1.46

Early-Stage Detection of Alpha-Synuclein Aggregation using Curcumin Based Molecule

3.5 Experimental Section

3.5.1 Protein Expression and Purification

The protein was expressed and purified as reported earlier with few modifications.[17]. *Escherichia coli BL21*(DE3) codon plus (Stratagene) cells transformed with pRK 172 were grown overnight at 37 °C in Luria Bertani broth (LB) medium containing 100 µg/mL ampicillin and then sub cultured into 1000 mL of LB containing 100 µg/mL ampicilline. At an OD600 of 0.8-1.0, the cells were induced by adding 10 µg/mL isopropyl-β-galactosidase (IPTG) at 25 °C and pelleted down after 5 h. The cells were resuspended in osmotic shock buffer (30 mM tris-HCl, 40 % w/v sucrose, 2 mM EDTA, pH 7.2), incubated at 25 °C for 15 min, and centrifuged to remove supernatant. The pellet was resuspended in Milli-Q water containing 1mM $MgCl_2$, and the supernatant was separated by centrifugation at 4000 RPM. This supernatant was dialyzed twice against 20 mM tris HCl buffer, pH 8.0 at 4 °C. The protein was denatured by adding 8M urea solution loaded onto DEAE FF ion-exchange column (15 mL, Hitrap, GE Healthcare). The loaded protein was washed and then eluted out using gradient of 100-300 mM NaCl. The eluted protein was concentrated by ultrafiltration (Millipore), flash-frozen in liquid N_2, and stored at -80 °C.

3.5.2 ThT (Thioflavin-t) Fluorescence Assay

Assays were initiated by placing the 96-well plate at 37 ºC under quiescent conditions in a plate reader (Fluoroskan Ascent, Thermo Scientific). The ThT fluorescence was measured through the bottom of the plate using a 440 nm excitation filter and a 480 nm emission filter. The ThT fluorescence was followed for two repeats of each sample. Similarly, CR-3 fluorescence was measured through the bottom of the plate using two excitation filter 350 nm and 450 nm emission filter.

3.5.3 Steady-state and time-resolved study

The steady-state absorption and emission spectra were recorded using a UV-Vis spectrophotometer (Shimadzu, UV-2600) and Fluoromax-4 Spectrofluorometer (Horiba Jobin Yvon), respectively. Emission intensity decays were collected by a time-correlated single photon counting (TCSPC) set-up from Horiba Jobin Yvon. Fluorescence signals were collected at the magic angle using MCP-PMT (Hamamatsu, Japan) detector. In the time-resolved experiments, samples were excited with a 375 nm diode laser and the instrument response function (IRF) of the

TCSPC set-up was ~50 ps. All spectroscopic measurements were performed at 25 °C. Each study was performed multiple times with high reproducibility.

3.5.5 Atomic Force Microscopy (AFM) study

Atomic Force Microscopy (AFM) imaging was performed on the Key Sight 5500 AFM instrument (Agilent Technologies) under tapping mode with silicon nitride tip. The concentration of fibrils was 50 µM and the concentration of the probe was 8 µM. 7 µl sample was added on a silicon wafer and dried overnight. The dried sample was washed with water to remove the salt from the surface of the silicon wafer before AFM measurements. The percentage of THF contained in each solution is 0.8%. Multiple images were taken of each sample at different magnifications.

3.5.6 Synthesis and Characterization of CR-3

Acetyl acetone (2 ml, 20 mmol) was dissolved in ethyle acetate (4ml). Boric anhydride was added and the mixture was stirred at 70^0 C for 40 min. 2-bromo- 4-dimethyle amino benzaldehyde (0.99 gm, 6.7 mmol) and the tributyl borate was added to this solution. The resulting mixture was stirred at 70^0 C for 30 min. Butyl amine was added dropwise over a period of 20 min and the solution was stirred at 50^0 C for 30 min. The solution was extracted with EtoAc and the resulting crude product was purified by chromatography (1E,4Z)-1-(2-bromo-4-(dimethylamino) phenyl)-5-hudroxyhexa-1,4-dien-3-one (60 % yield). ^{1}H NMR (400 MHz, $CDCl_3$) δ 15.28 (bs, 1H), 7.90 (d, *J* = 15.8 Hz, 1H), 7.39 (d, *J* = 8.9 Hz, 1H), 6.85 (d, *J* = 3.1 Hz, 1H), 6.61 (dd, *J* = 8.9, 3.1 Hz, 1H), 6.38 (d, *J* = 15.8 Hz, 1H), 5.71 (s, 1H), 2.96 (s, 6H), 2.17 (s, 3H) (Appendix 3.1).

3.5.6 The details of the Docking Study

The docking was performed blindly. The whole protein was taken to dock the compounds as we did not know where exactly the compounds would bind.
The box size and the docking parameters are: enter_x = 2.14446559039
center_y = -17.4340713818
center_z = 9.14415896485
size_x = 89.0750840071
size_y = 66.6537616541
size_z = 49.6060257183

exhaustiveness = 8

Early-Stage Detection of Alpha-Synuclein Aggregation using Curcumin Based Molecule

3.6 References

1. Hardy, J.; Selkoe, D. J., The amyloid hypothesis of Alzheimer's disease: progress and problems on the road to therapeutics. *Science* **2002,** *297* (5580), 353-6.
2. Eisenberg, D.; Jucker, M., The amyloid state of proteins in human diseases. *Cell* **2012,** *148* (6), 1188-1203.
3. Aslund, A.; Sigurdson, C. J.; Klingstedt, T.; Grathwohl, S.; Bolmont, T.; Dickstein, D. L.; Glimsdal, E.; Prokop, S.; Lindgren, M.; Konradsson, P.; Holtzman, D. M.; Hof, P. R.; Heppner, F. L.; Gandy, S.; Jucker, M.; Aguzzi, A.; Hammarström, P.; Nilsson, K. P., Novel pentameric thiophene derivatives for in vitro and in vivo optical imaging of a plethora of protein aggregates in cerebral amyloidoses. *ACS Chem Biol* **2009,** *4* (8), 673-84.
4. Ross, C. A.; Poirier, M. A., Protein aggregation and neurodegenerative disease. *Nature medicine* **2004,** *10* (Suppl 7), S10-S17.
5. Chiti, F.; Dobson, C. M., Protein Misfolding, Functional Amyloid, and Human Disease. *Annual review of biochemistry* **2006,** *75* (1), 333-366.
6. Kumar, V.; Sami, N.; Kashav, T.; Islam, A.; Ahmad, F.; Hassan, M. I., Protein aggregation and neurodegenerative diseases: From theory to therapy. *European journal of medicinal chemistry* **2016,** *124*, 1105-1120.
7. Chen, S. W.; Drakulic, S.; Deas, E.; Ouberai, M.; Aprile, F. A.; Arranz, R.; Ness, S.; Roodveldt, C.; Guilliams, T.; De-Genst, E. J.; Klenerman, D.; Wood, N. W.; Knowles, T. P. J.; Alfonso, C.; Rivas, G.; Abramov, A. Y.; Valpuesta, J. M.; Dobson, C. M.; Cremades, N., Structural characterization of toxic oligomers that are kinetically trapped during α-synuclein fibril formation. *Proceedings of the National Academy of Sciences* **2015,** *112* (16), E1994-E2003.
8. Amaro, M.; Kubiak-Ossowska, K.; Birch, D. J.; Rolinski, O. J., Initial stages of beta-amyloid Aβ1− 40 and Aβ1− 42 oligomerization observed using fluorescence decay and molecular dynamics analyses of tyrosine. *Methods and applications in fluorescence* **2013,** *1* (1), 015006.
9. Campioni, S.; Mannini, B.; Zampagni, M.; Pensalfini, A.; Parrini, C.; Evangelisti, E.; Relini, A.; Stefani, M.; Dobson, C. M.; Cecchi, C., A causative link between the structure of aberrant protein oligomers and their toxicity. *Nature chemical biology* **2010,** *6* (2), 140-147.
10. Chiti, F.; Dobson, C. M., Amyloid formation by globular proteins under native conditions. *Nature chemical biology* **2009,** *5* (1), 15-22.
11. Xing, R.; Yuan, C.; Li, S.; Song, J.; Li, J.; Yan, X., Charge-Induced Secondary Structure Transformation of Amyloid-Derived Dipeptide Assemblies from β-Sheet to α-Helix. *Angewandte Chemie International Edition* **2018,** *57* (6), 1537-1542.
12. Hamada, D.; Tanaka, T.; Tartaglia, G. G.; Pawar, A.; Vendruscolo, M.; Kawamura, M.; Tamura, A.; Tanaka, N.; Dobson, C. M., Competition between Folding, Native-State Dimerisation and Amyloid Aggregation in β-Lactoglobulin. *Journal of Molecular Biology* **2009,** *386* (3), 878-890.
13. Cremades, N.; Cohen, S. I.; Deas, E.; Abramov, A. Y.; Chen, A. Y.; Orte, A.; Sandal, M.; Clarke, R. W.; Dunne, P.; Aprile, F. A.; Bertoncini, C. W.; Wood, N. W.; Knowles, T. P.; Dobson, C. M.; Klenerman, D., Direct observation of the interconversion of normal and toxic forms of α-synuclein. *Cell* **2012,** *149* (5), 1048-59.
14. Winner, B.; Jappelli, R.; Maji, S. K.; Desplats, P. A.; Boyer, L.; Aigner, S.; Hetzer, C.; Loher, T.; Vilar, M.; Campioni, S., In vivo demonstration that α-synuclein oligomers are toxic. *Proceedings of the National Academy of Sciences* **2011,** *108* (10), 4194-4199.

15. Linse, S., Monomer-dependent secondary nucleation in amyloid formation. *Biophys Rev* **2017,** *9* (4), 329-338.
16. Biancalana, M.; Makabe, K.; Koide, A.; Koide, S., Molecular mechanism of thioflavin-T binding to the surface of beta-rich peptide self-assemblies. *J Mol Biol* **2009,** *385* (4), 1052-63.
17. Huang, C.; Ren, G.; Zhou, H.; Wang, C.-c., A new method for purification of recombinant human α-synuclein in Escherichia coli. *Protein Expression and Purification* **2005,** *42* (1), 173-177.

Chapter 4

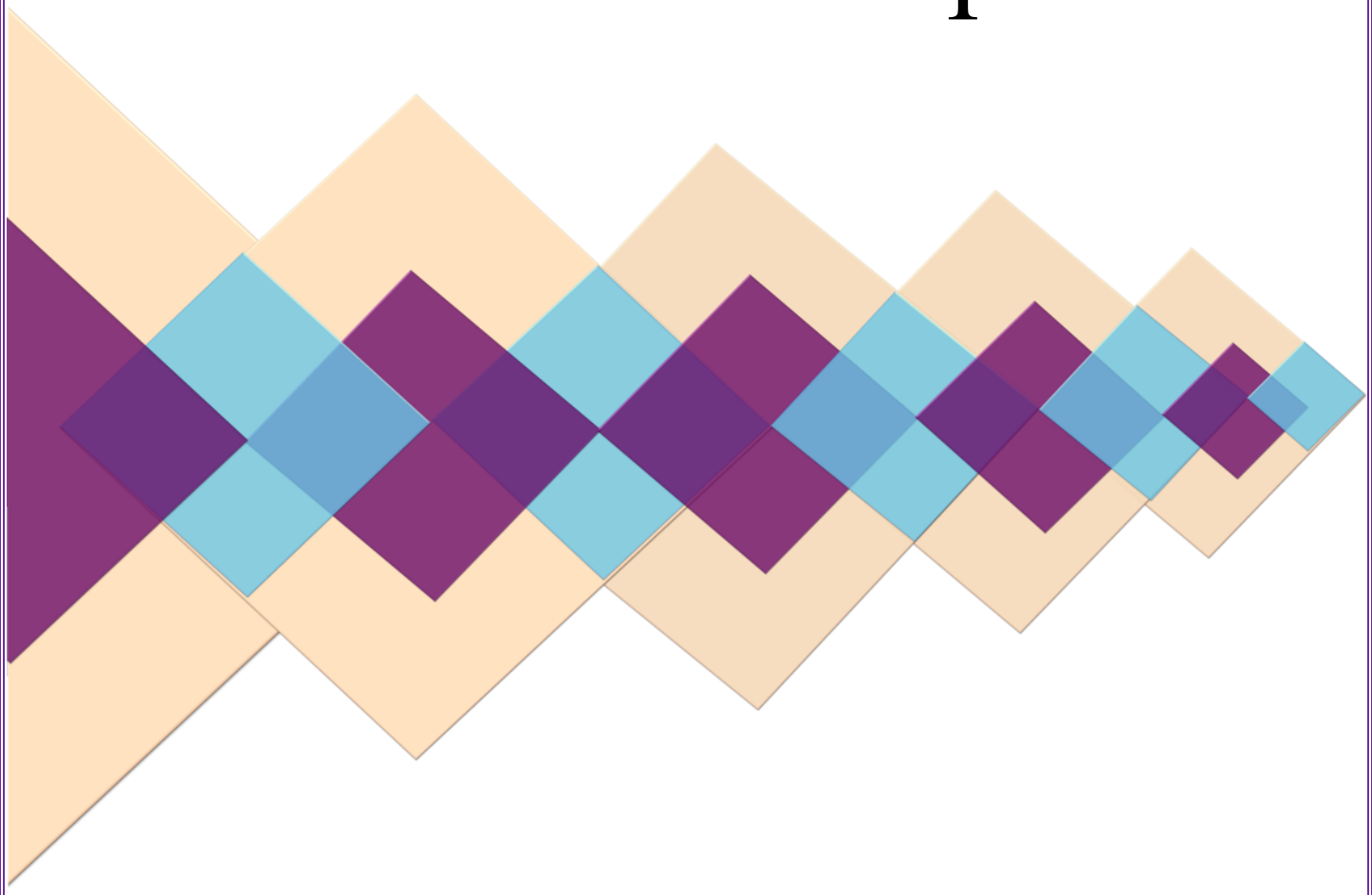

Development of a Systematic Strategy Towards Promotion of α-Synuclein Aggregation By 2-Hydroxyisophalamide Based System

Development of a Systematic Strategy Towards Promotion of Alpha-Synuclein using 2-hydroxy isophthalamide Based System

4.1 Introduction

Parkinson's disease (PD) is known as the second most familiar neuro-degenerative disorder after Alzheimer's disease[1-4]. Movement disorder resulting from degeneration of dopaminergic neurons in substantia nigra is the major symptom of PD[5-7]. The source of the disease is enigmatic, but significant verification has pointed towards multifactorial etiology involving genetic susceptibility and environmental factors[8-10]. Over the last two decades, PD has been illuminated as a serious global burden due to the increased ratio of the aged population[11-12]. As an estimate, more than 6.1 % of individuals have PD globally[13]. Therefore, scientists have devoted much more effort for devising different methods to coherently inspect the causality of the haze of this disease[14-16].

Involvement of the aggregation of α-synuclein, a small (~14.4 kDa), abundant, and highly conserved presynaptic protein, is found to play a vital role in the PD[4,15, 17-21]. The aggregation process of α-synuclein is associated with highly complicated interactive transient species[5, 23-30], due to which developing a suitable approach to suppress the formation of α-synuclein aggregates and their associated toxicity becomes very difficult. The literature shows evidences of many efforts to understand the mechanism of aggregation of α-synuclein to prevent it. It has been reported that trodusquemine can displace α-synuclein and its oligomers from the membrane, inhibiting both the lipid-induced initiation of the aggregation process and the ability of the oligomers to disrupt the integrity of membranes[22-23]. Similarly, squalamine inhibits the initiation of α-synuclein aggregation and suppresses the α-synuclein oligomers mediated toxicity in human neuroblastoma cells[24]. Very recently, a high-throughput screening methodology has been exploited to identify a small molecule (SynuClean-D) able to inhibit α-synuclein aggregation[25]. However, direct control over effective strategy for the oligomerization and fibrillization processes of α-synuclein for PD and related neurodegenerative diseases is lacking.

The chemical kinetics approach is believed to be suitable for the detailed interpretation of the molecular events leading to protein aggregation at a microscopic level[26-30]. These kinetic measurements guide to resolve the complicated reaction network accountable for generating different aggregated forms of α-synuclein and to assist the quantitative measurement of the reactive fluxes associated with the various microscopic events during the overall aggregation process[31-33]. Therefore, an extensive work has been done in the field of protein aggregation using the chemical kinetic platform[26-27, 34-35]. Additionally, this approach has also shown its potency in the field of drug

discovery[30, 36-41], which helps in the quantitative measurement of reactive fluxes associated with various microscopic events in the absence and presence of the drug molecules (Figure 4.1a). However, the association between different aggregation step makes it extremely challenging to evaluate the overall effects of interfering focused at influencing the population balance of specific species. Therefore, a potent strategy of inhibition or promotion is essential which associate with detailed mechanistic understanding based on the influence of drug on the aggregation reaction network. Despite this importance, the challenging part is to established a quantitative relation between drug binding to aggregating species and the resulting inhibiting or promoting effect**.** However, people have successfully developed a quantitative relationship between drug binding to aggregating species and resulting inhibiting effect, but for the promotion is so far lacking. Therefore, In this study, we focused to established a potent method for the promotion of a-synuclein aggregation. In order to address this limitation, we are going introduce a general theory of promotion of amyloid formation. Therefore, we devise the problem in respects of master equation for aggregation kinetics in the presence of promoters that bind one or more species of the aggregating species. We obtain precise integrated rate laws to such effective equations for compounds that preserve the structure of the aggregation-reaction network. In an effort to check we have used completely new molecules in this field, namely, N^1, N^3-dihexyl-2-hydroxyisophthalamide (MAX-1), 2-hydroxy-N^1, N^3-dioctylisophthalamide (MAX-2) and 2-hydroxy-N^1, N^3-di-p-tolylisophthalamide (MAX-3) (Figure 4.1b), whose core structures consist with isophthalamide, but side chains have different structural features. These molecules were recently reported along with other structural analogues as synthetic ion transport systems for anticancer therapy[42-43]. We anticipate the different modifications in the chemical structure of the compounds may systematically modulate the reactive flux towards oligomer and fibril formation. In this study, we developed a quantitative relationship between the molecule binding event with aggregating species and the resulting modulation of the overall aggregation process. In addition, we also explored the effects of these molecules on inhibiting the cytotoxicity of preformed oligomers of α-synuclein towards neural cell line (SH-SY5Y) and tried to map an *in-vitro* mechanism by which these molecules significantly regulate the aggregation process of α-synuclein *in-cellulo*.

Development of a Systematic Strategy Towards Promotion of Alpha-Synuclein using 2-hydroxy isophthalamide Based System

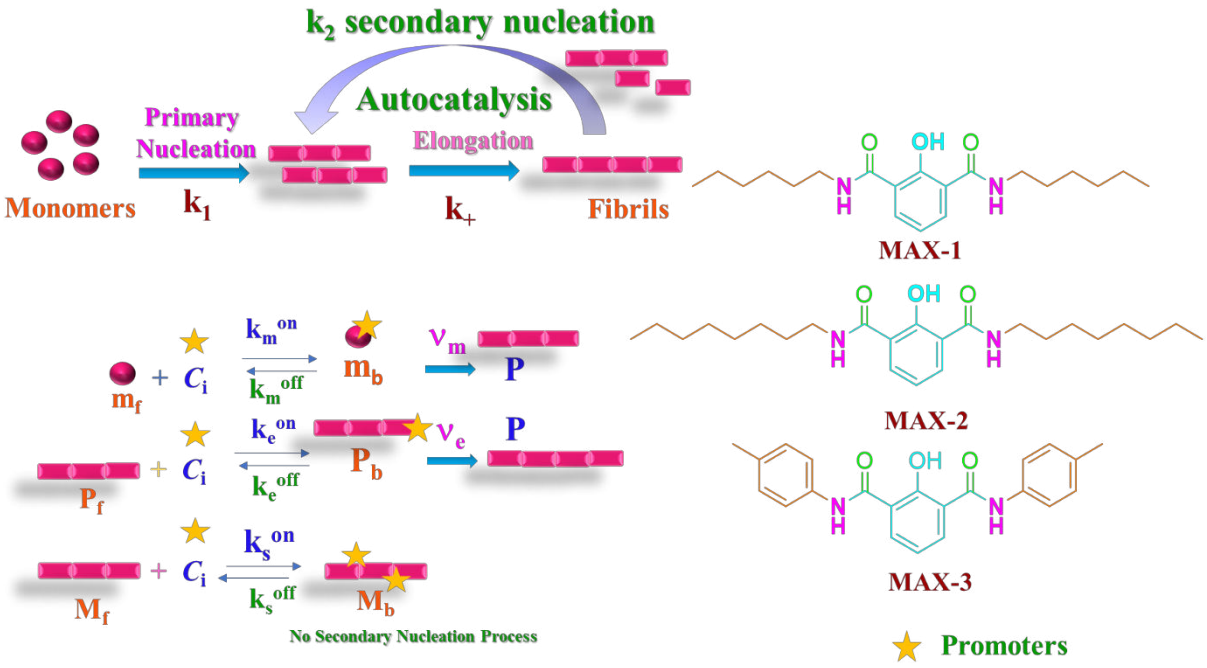

Figure 4.1 a) Schematic representation of the microscopic mechanism of protein aggregation in the absence and presence of MAX molecules. b) Chemical structures of MAX-1, MAX-2, and MAX-3.

4.2 RESULTS AND DISCUSSION

4.2.1 Microscopic Mechanisms from Macroscopic Kinetic Profiles

The aggregation process of α-synuclein involves complex nonlinear kinetics in which aggregating species concomitantly act as the reactants, products, intermediates, and catalysts of the reaction[32, 44] (Figure 4.1a). The combined nature of the aggregation steps makes it extremely challenging to estimate the effects of interfering events that point at influencing the population balance of specific species[31]. To dissect this complex network, the master equation has been developed (equation 1), which can map the series of microscopic events, including primary nucleation, fibril elongation, and secondary nucleation process, in a quantitative manner[26]. This process is associated with reaction rate constants k_n, k_+ and k_2, respectively. The time evolution of the total fibrils mass concentration $M(t)$ derived from self-consistent solutions of the master equation[27, 45].

$$\frac{M(t)}{M(\infty)} = 1 - \alpha\left\{\left(\frac{(B_+ + C_+)}{B_+ + C_+ e^{kt}}\right)\left(\frac{B_- + C_+ e^{kt}}{B_- + C_+}\right)\right\}^{-\frac{k^2{}_\infty}{\kappa k'_\infty}} e^{-k_\infty t} \qquad (1)$$

Where,

$B_\pm = (k_\infty \pm k'_\infty/(2\kappa)$ $k'_\infty = \sqrt{2\kappa^2/[n_2(n_2+1)] + 2\lambda^2/n_c}$

$C_\pm = \pm\lambda^2/2\kappa^2$ $k'_\infty = \sqrt{k_\infty{}^2 - 4C_+C_-\kappa}$

$\kappa = \sqrt{2k_+k_2\, m(0)^{n_2+1}}$

$\lambda = \sqrt{2k_+k_n\, m(0)^{n_c}}$

where the kinetic parameters $B_\pm, C_\pm$, λ, κ and k'_∞ are functions of the two-combination rate constants k_+k_n and k_+k_2.

k_n= rate constant for primary nucleation

n_c = reaction order for primary nucleation

k_2 = rate constant for secondary nucleation.

$n_{2=}$ reaction order for secondary rate nucleation.

k_+ = rate constant for elongation.

$m(0)$ = monomer concentration at time zero.

$M(t)$ = mass of the fibrils at time t.

Development of a Systematic Strategy Towards Promotion of Alpha-Synuclein using 2-hydroxy isophthalamide Based System

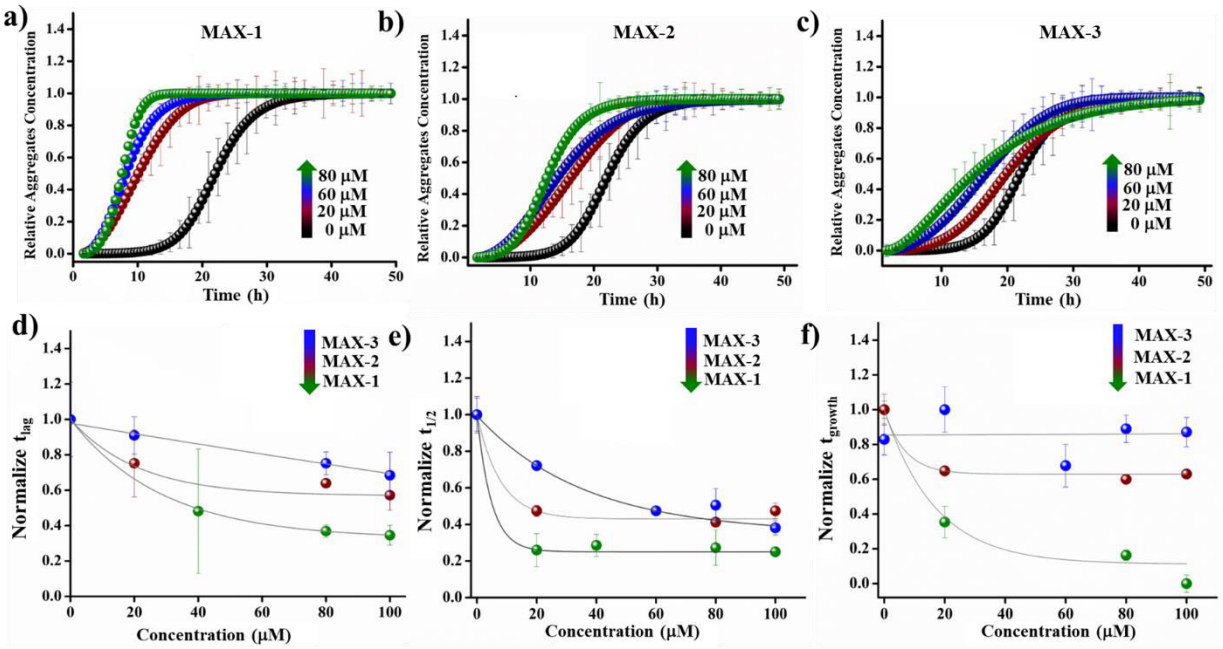

Figure 4.2 a), b), c) Comparison ThT fluorescence monitored aggregation kinetics of 80 µM α-synuclein sample in the presence of different concentrations of MAX-1, MAX-2, and MAX-3**.** d) Evolution of normalized $t_{10\%}$ value in the presence of MAX-1, MAX-2, MAX-3. e) Evolution of normalized $t_{1/2}$ value in the presence of MAX-1, MAX-2, MAX-3. f) Evolution of normalized $t_{90\%}$ value in the presence of MAX-1, MAX-2, MAX-3.

In this study, we monitored aggregation kinetics of α-synuclein in the absence and presence of MAX-1, MAX-2 and MAX-3. Interestingly, in the presence of MAX molecules, the aggregation kinetics of α-synuclein is promoted as a result of the interactions between the molecule and one or more protein species present in the system, which eventually leads to fundamental changes in the microscopic rates involved in the aggregation process (Figure 4.2a, b, c). The order of the accelerating ability of these molecules is MAX-1 > MAX-2 > MAX-3, which is also clearly evident from the $t_{1/2}$ plot in a dose-dependent manner (Figure 4.2f). The decreasing rate of $t_{1/2}$ follows the order of MAX-1 > MAX-2 > MAX-3, respectively. To unveil this trend, at first, it is necessary to understand the binding affinity of these molecules to the monomeric α-synuclein. The analysis of bio-layer interferometric (BLI) measurements (Figure 4.3) provides an idea about the binding rate of the molecules with α-synuclein (k_{on} in Table 1), which is in the order of MAX-1 >

MAX-2 > MAX-3, respectively. Thus, the results imply that macroscopic aggregation kinetics of α-synuclein is following the order of binding affinity of the molecules with monomeric α-synuclein, which suggests that the higher molecular binding affinity can increase the rate of the aggregation process.

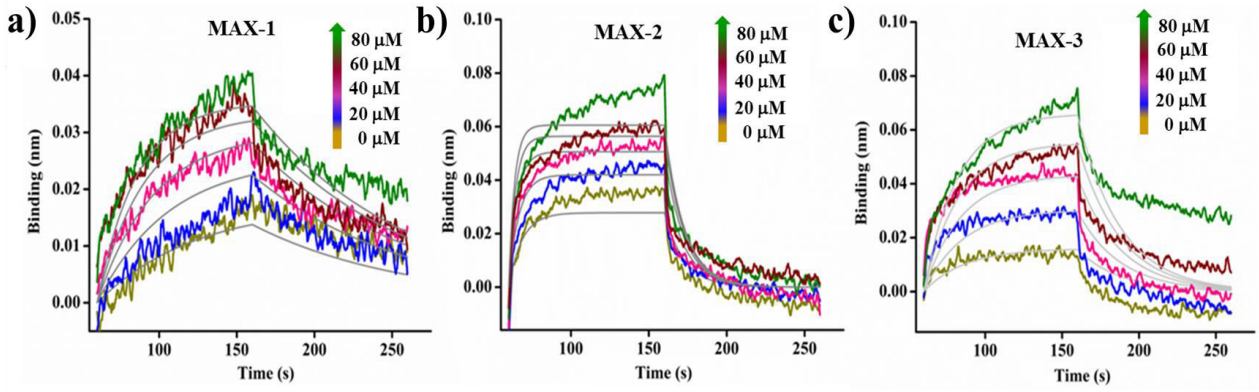

Figure 4.3 a), b), c) Biolayer interferometric study (BLI) of α-synuclein in the presence of MAX-1, MAX-2, and MAX-3, respectively.

Table 1. Analysis of binding rate (k_{on}), dissociation rate (k_{ids}) and binding constant (K_D) with monomeric α-synuclein acquired from bio-layer interferometric study.

[Molecules]	K_D (M)	k_{on} (1/M. s)	k_{dis} (1/s)
MAX-1	3×10^{-5}	4.98×10^{3}	1.28×10^{-1}
MAX-2	2.29×10^{-5}	5.83×10^{2}	1.13×10^{-2}
MAX-3	1.35×10^{-2}	9.60×10^{1}	6.55×10^{-2}

We have further performed a quantitative analysis of α-synuclein aggregation in the presence of MAX molecules to determine the rate constants governing each microscopic step. The investigation of t_{lag} (time required to reach ThT fluorescence intensity to 10% of its final value) of α-synuclein aggregation shows that these molecules have concentration dependent effects on t_{lag} (Figure 4.2d). This observation suggests that the primary nucleation pathway is perturbed by these molecules, and the order of the modulating ability on the primary pathway of aggregation is MAX-1 > MAX-2 > MAX-3. Similarly, the analysis of t_{growth} (time required to reach ThT fluorescence intensity to 90% of its final value) exhibits that MAX-1, and MAX-2 have concentration

dependent effects. However, no significant effect has been observed in the case of MAX-3 (Figure 4.2f). This observation suggests that MAX-3 has a suppressing effect on the secondary pathway of nucleation. The order of suppressing ability of the molecules is on the basis of the order MAX-3 > MAX-2 > MAX-1.

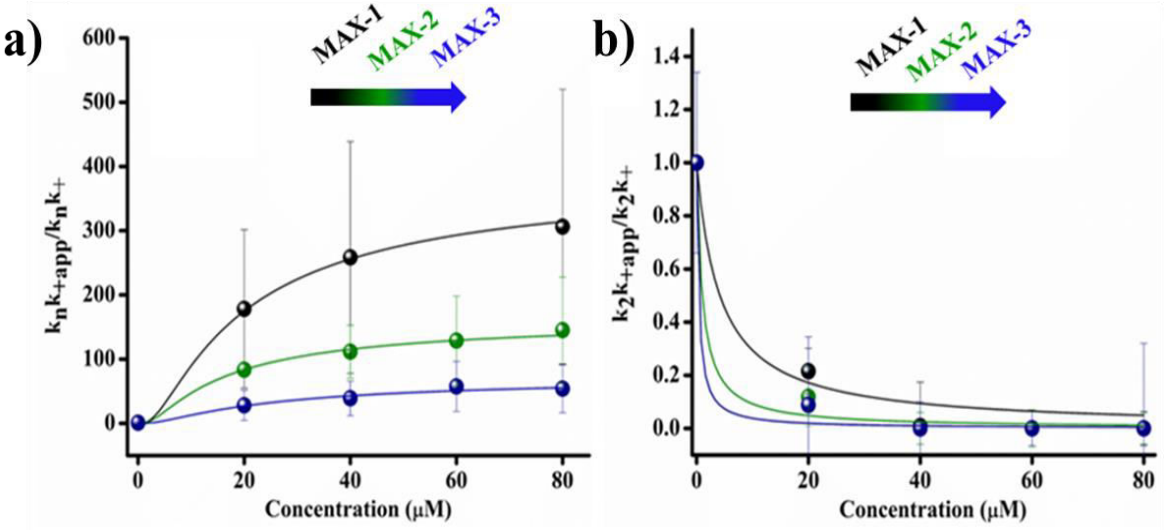

Figure 4.4 a) The dependence of the apparent reaction rate constants of primary pathways ($\mathbf{k_+k_n}$) shown with increasing concentrations of different small molecules (MAX-1, MAX-2, MAX-3). b) Dependence of the apparent reaction rate constants of secondary pathways ($\mathbf{k_+k_2}$) shown with increasing concentrations of different small molecules (MAX-1, MAX-2, MAX-3).

To inspect the mechanism, we performed the semi-empirical quantitative analysis for the effects of all three compounds (MAX-1, MAX-2, MAX-3) promoting α-synuclein aggregation by fitting the aggregation profiles to a single rate law using web-based AmyloFit platform[26-27, 34]. From the fitting, we estimated the combined microscopic rate constants $k_n k_+$, which define the overall rate constants of primary pathways of aggregation, and $k_n k_2$, which represents the overall rate constants of secondary pathways. These aggregation profiles in the presence of all the compounds were compared with corresponding values estimated in the absence of the compounds, to elucidate the systematic disturbance of the microscopic rate constants in the rate law. The results revealed that the rate of $k_n k_+$ (primary pathways), increased as a function of the concentration of the above molecules (Figure 4 4a), indicating that these molecules are involved in enhancing the primary

pathway of aggregation. To estimate how much these molecules catalyzed the primary pathway of aggregation, an equation has been developed (S1.53), which provides us k_m^{on} (binding rate with monomer), k_e^{on} (binding rate at the end of the fibrils), v_m (catalytic rate for primary nucleation), v_e (catalytic rate for elongation). Consequently, the data points were fitted using the above equation (Figure 4.4a). After fitting the data points, we extracted the catalytic rate of primary nucleation and elongation process for each molecule (Table 2). The results indicate that these molecules are mainly involved in catalyzing the primary nucleation process. Moreover, we observed that the catalytic ability of the primary pathway of these molecules follows the order of MAX-1 > MAX-2 > MAX-3. The reason behind the promotion of the primary pathway of aggregation because of strong binding affinity of these molecules with monomeric α-synuclein leading to catalyzing the primary pathway of aggregation.

Table 2. Analysis of binding rate k_m^{on} with monomeric α-synuclein and fibrils end k_e^{on} and elongation process v_e.

[Molecules]	k_m^{on} ($M^{-1}s^{-1}$)	v_m (s^{-1})	k_e^{on} ($M^{-1}s^{-1}$)	v_e (s^{-1})
MAX-1	4.98×10^3	2.17×10^4	6.64	29.06
MAX-2	5.83×10^2	2.42×10^3	82.43	188.90
MAX-3	9.6×10^1	7.53×10^2	100.80	15.33

Now, to explore the influence of these molecules on the secondary pathway of aggregation, the rate of k_2k_+ (secondary pathway) was determined at different concentrations of the compound. Interestingly the rate of the secondary pathway was found to decrease as a function of the concentration of the above molecules (Figure 4.4b). After that, the data were fitted by using an equation (S1.54) developed by Dobson and co-workers in the limit of the fast binding of the drug molecules to the fibril surface[31]. The binding constant of each compound on the surface of the aggregates was determined by fitting the data points using this equation. The result indicates that MAX-3 has the highest binding affinity compared to MAX-1, and MAX-2 (Appendix Table2), therefore, it has a higher inhibiting ability towards the secondary pathway of aggregation. This result is consistent with our previous observation, explained in Figure 4.2f. To further confirmed

this study, we performed aggregation kinetic of α-synuclein with 10% preform seeds in the presence of different concentrations of MAX-1, MAX-2 and, MAX-3 (Appendix 4.12). The data were fitted using single rate law using AmyloFit platform in order to get the individual rate constants (k_2, k_n, k_+)[26, 46]. The fitted data provide us the rate of secondary nucleation (k_2) which decreases on the basis of the order of MAX-1 > MAX-2 > MAX-3 (Table 3). The decrease of the secondary nucleation process is because of the binding of these molecules along the surface of the fibrils, which suppresses the surface catalyzed secondary nucleation through blocking the incoming monomers on the surface of the fibrils. Overall, we have examined the secondary pathway of aggregation is getting inhibited by these molecules, probably because of the binding of these molecules on the surface of the fibrils suppressing the secondary nucleation.

Table 3. Microscopic rate constants from fitting.

[Molecules]	k_n ($M^{-1}s^{-1}$)	k_+ ($M^{-1}s^{-1}$)	k_2 ($M^{-2}s^{-1}$)
0 μM Molecule	6.14×10^{-5}	2.06×10^{6}	1.18×10^{10}
80 μM MAX-1	64.3	3.43×10^{3}	7.57×10^{7}
80 μM MAX-2	15.5	4.25×10^{5}	1.08×10^{7}
80 μM MAX-3	0.175	2.93×10^{5}	1.28×10^{6}

Next, we also calculated the reactive flux (using equation 2) towards the formation of oligomers in the absence and presence of increasing concentrations of these compounds (Figure 4.5a)). Generally, we have found that the time taken to form the maximum number of oligomers is reduced by these molecules in the order MAX-1 > MAX-2 > MAX-3 (Figure 4.5a). After that, we calculated the production of oligomers in the absence and presence of these molecules. The result indicates that in the presence of these molecules, the production of oligomers reduced in the order of MAX-3 > MAX-2 > MAX-1 (Figure 4.5b).

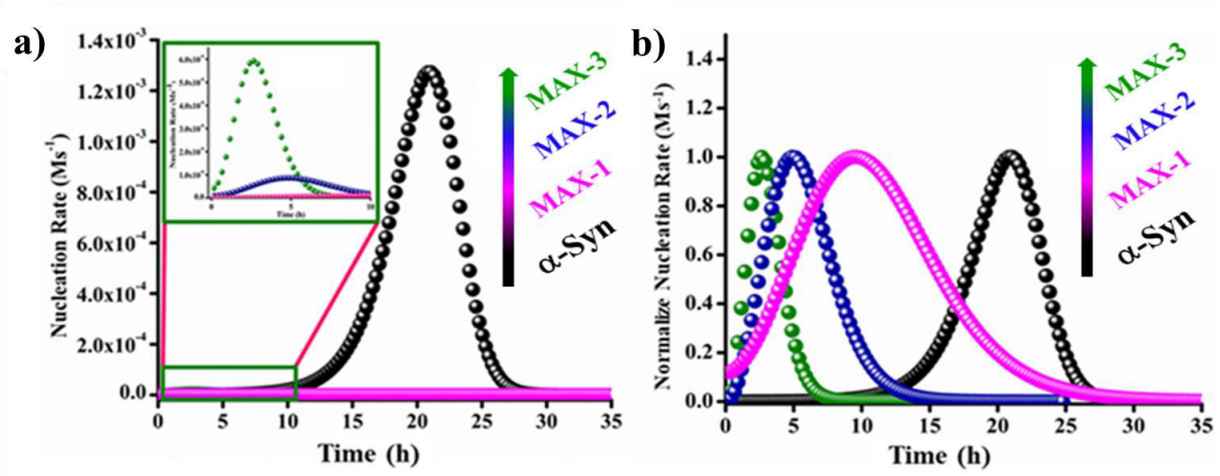

Figure 4.5 a) Time evolution of nucleation rate calculated from kinetic analysis in presence and absence of MAX-1, MAX-2, and MAX-3 b) Normalized time evolution of nucleation rate calculated from kinetic analysis in the presence and absence of MAX-1, MAX-2, and MAX-3.

4.2.2 Transmission Electron Microscopy (TEM) Image analysis

To understand how these compounds affect the morphology of fibrils formed by α-synuclein, TEM was performed in the absence and presence of these compounds at the saturation of aggregation reaction (Figure 4.6). The main images are then treated with several image processing steps using MIPAR^{TM} software to get useful information from the analysis. The comparison of the original image with that of the final processed results are shown in (Figure 4.6). The initial analysis of original TEM images of α–synuclein fibrils demonstrates that the fibrils formed by α-synuclein in the presence of these molecules (MAX-1, MAX-2, MAX-3) were shorter than the fibrils formed in their absence. After processing the images, we observed that the mean eccentricity and aspect ratio of the fibrils, which dictate the shape and lengths of the fibrils, in the presence of the MAX-1, MAX-2, and MAX-3 decreases concomitantly than the fibrils formed by α-synuclein in the absence of these (Appendix 4.9). The shortening of the fibrils occurred possibly due to high-frequency primary nucleation events caused by a lesser number of availabilities of monomeric protein for the elongation of fibrils.

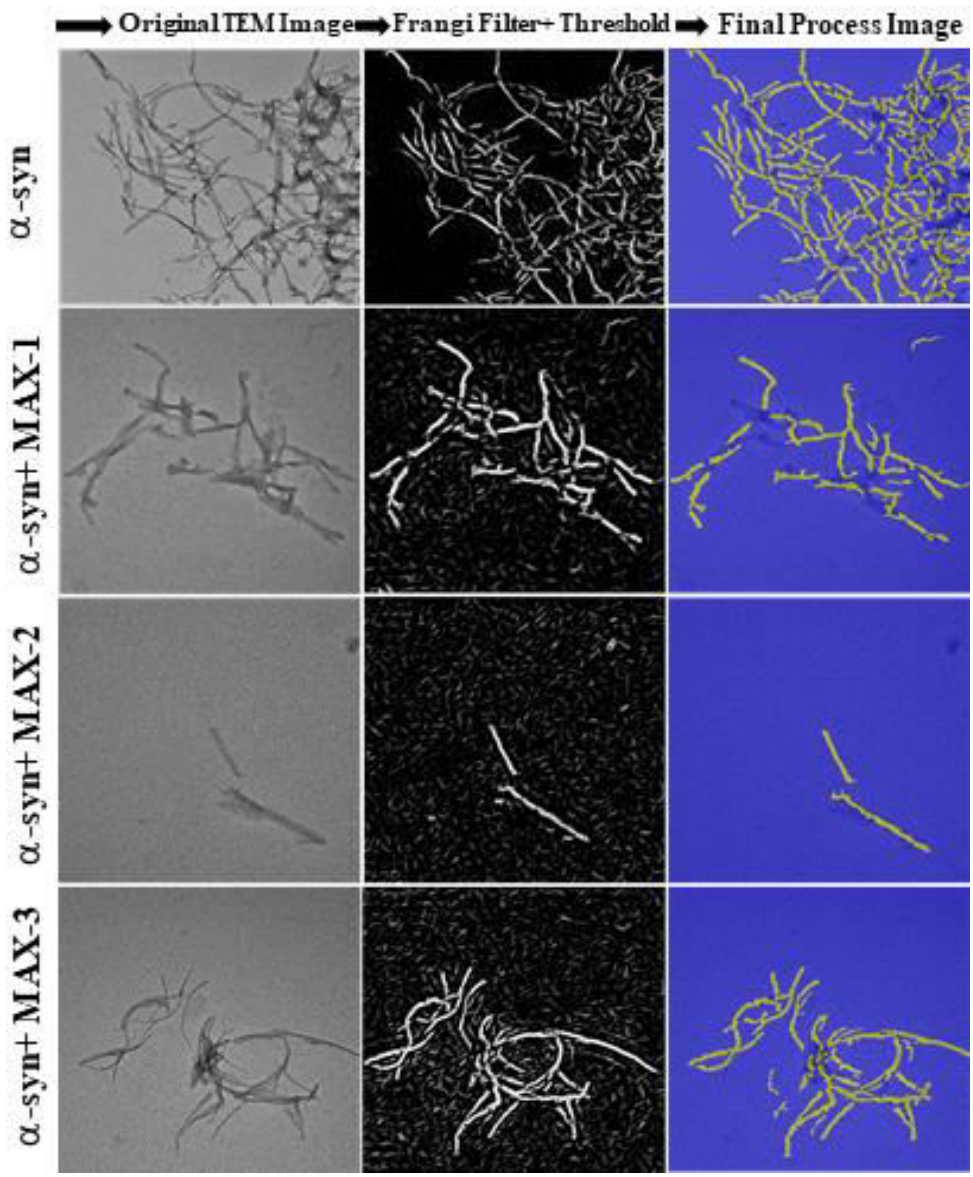

Figure 4.6 Original TEM images of α-synuclein fibrils formed in the absence and presence of MAX-1, MAX-2, and MAX-3, in comparison with post-processed images. Processing steps are shown at the top of each vertical panel and the sample ID is shown on the left side of the corresponding original images.

4.2.3 Characterization of the Oligomers and Cell Viability Assay

To investigate the toxicity of α-synuclein oligomers, we prepared (see Materials and method section in experimental section) α-synuclein oligomers and further characterized them using atomic force microscopy (AFM). The raw AFM images were then analyzed stepwise (recipe) to get an idea

about the mean eccentricity and aspect ratio of the oligomer (Appendix 4.11). The mean value of eccentricity (0.70 ± 0.14) and aspect ratio (1.56 ± 0.52) define the shape of the oligomers, which is elliptical in nature (Figure 4.7a, b, c).

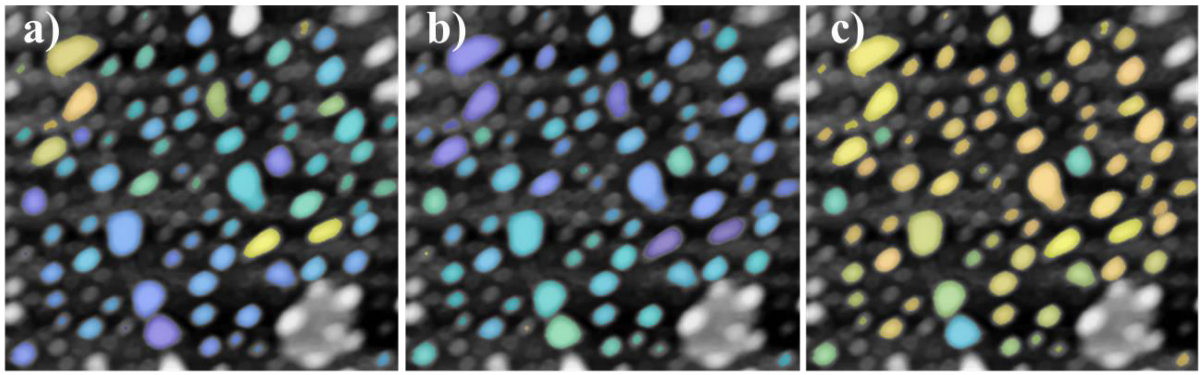

Figure 4.7 a), b), c) Processed (Using MIPAR™) AFM image of α-synuclein oligomer. To check the cytotoxicity, different concentrations of α–synuclein oligomers were added to the cell culture medium with neuroblastoma SH-SY5Y cell line. The WST-1 assay kit (Roche) was used to measure the viability of the cells.

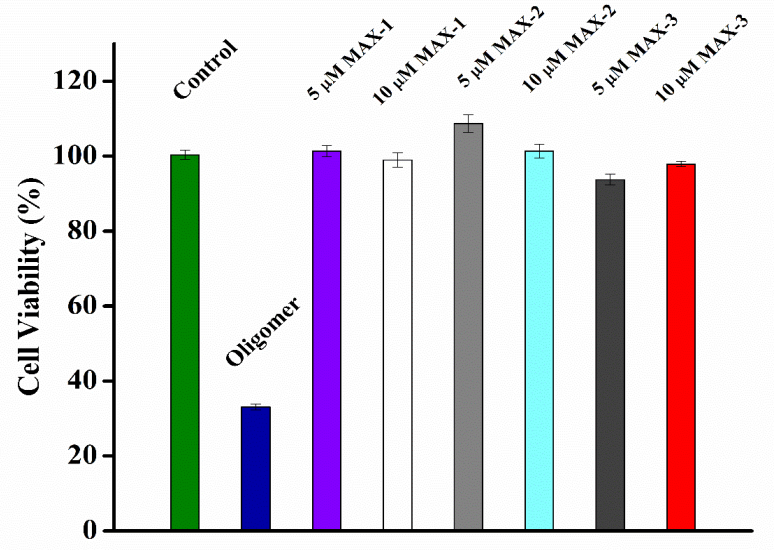

Figure 4.8. Effects of MAX-1, MAX-2, and MAX-3 on alpha-synuclein oligomer toxicity in the neuroblastoma cell line (SH-SY5Y).

The viability of neuroblastoma SH-SY5Y was found to reduce in concentration-dependent manner as measured by their ability to reduce WST-1 fluorescence (Figure 4.8). In order to check the viability of cells by these molecules, the α-synuclein oligomers 5 μM (monomer equivalents) were incubated for 1 h at 37 °C under shaking conditions in the absence and presence of different concentrations of MAX-1, MAX-2**,** and MAX-3, and added to cell culture medium with cells seeded in 96 well plates for 24 h, and then 10 μL of WST-1 reagent was added into each well. The cell viability study depicted that the presence of MAX-1, MAX-2, and MAX-3 decreased the toxicity of oligomers when used in a 1:1 ratio of α-synuclein to these molecules. The cell viability was increased by 60.5 ± 1.3 (MAX-3), 69.11 ± 2.54 (MAX-2) and 75.52 ± 0.22 (MAX-1) relative to the untreated cells, a value approximately equal to that of cell treated with 5 μM oligomers (Figure 4.8).

4.2.4 Displacing α-synuclein from Lipid Membranes

Many reports have suggested that α-synuclein oligomers perturb the biological membranes and disrupt the cellular function of human neuro-blastoma cells[47-51] . Therefore, to understand the binding mechanism of these molecules with α-synuclein on the membrane surface of the cells, we tried to mimic the membrane by using EYPC (Egg yolk phosphatidylcholine) lipids. We prepared the vesicles using EYPC lipids and incubated them with native monomeric α-synuclein. Next, we titrated α-synuclein bound to EYPC lipid vesicles with MAX-1, MAX-2, and MAX-3 and the titration was probed by circular dichroism (CD) study (Figure 4.9a, b, c). The Changes in CD peak suggest that these molecules change the conformation of EYPC bound α-synuclein from α-helices to strong β-turn, indicating that these molecules have a strong binding affinity towards lipid-bound α-synuclein. To further confirm, whether these molecules can influence the conformation transition of α-synuclein in the absence of lipid or not, we have again performed CD study in the absence of lipid (Figure 4. 9d, e, f)**.** Interestingly, CD study suggests that these molecules can successfully influence the conformation transition of α-synuclein (random coil to β−turn) in the absence of lipid. Thus, the above results confirmed that these molecules strongly interact with α-synuclein on the surface of the lipid. Overall, this study provides an insight into the *in-vitro* mechanism by which these molecules significantly modulate the aggregation of α-synuclein in a real biological membrane environment.

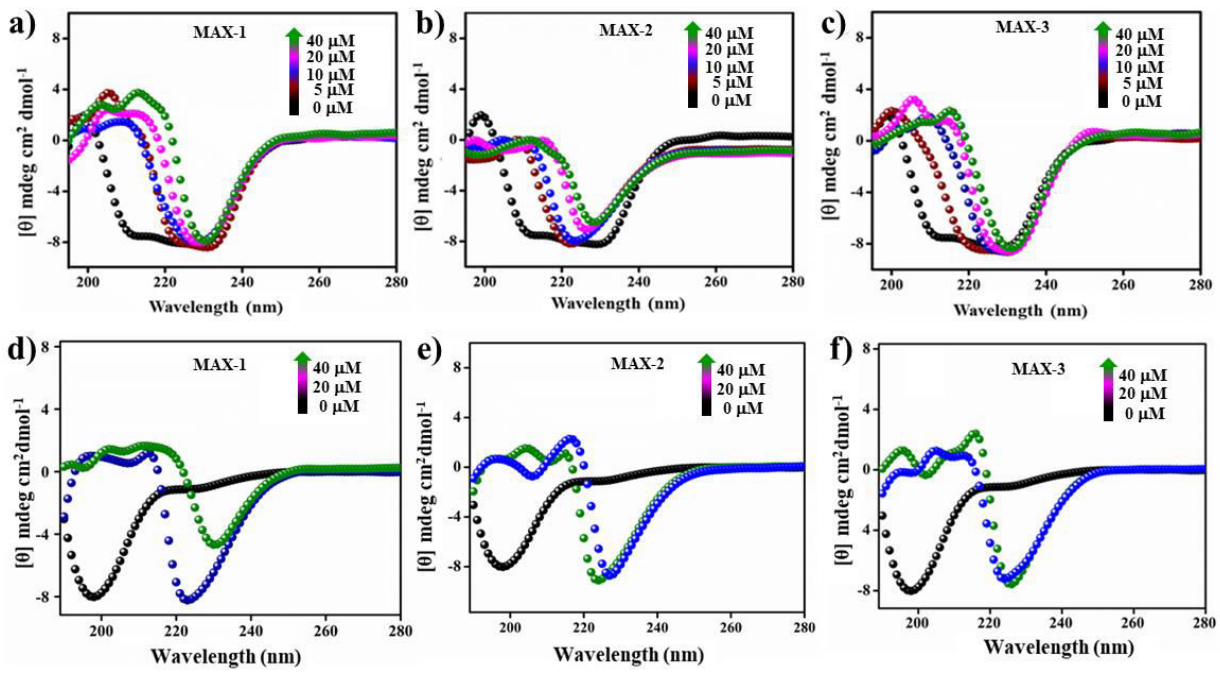

Figure 4.9 a), b), c) Changes in the secondary structure of native α-synuclein monitored using circular dichroism in the presence of 0.80 mM vesicles in the absence (black) and presence (colors) of increasing concentrations of MAX-1, MAX-2, and MAX-3. MAX-1: 5 µM (green) 10 µM (sky blue), 20 µM (maroon), 40 µM (Cyan). MAX-2: 5 µM (green) 10 µM (sky blue), 20 µM (pink), 40 µM (maroon). MAX-3: 5 µM (blue), 10 µM (maroon), 20 µM (pink), 40 µM (green). D), E), F) Changes in the conformation of native α-synuclein monitored in the presence of different concentrations of MAX-1, MAX-2, and MAX-3 and in the absence of lipid.

4.2.5 Amyloid Disintegration Kinetics

To check whether these molecules are able to disintegrate α-synuclein fibrils or not, we monitored changes in the signal of ThT incubated with fibrils in the absence and presence of MAX-1, MAX-2, and MAX-3 (Figure 4.10). Interestingly, we have observed that the falling of ThT signal is proportional to the function of the concentration of these molecules (Figure 4.10). The rapid signal falling was obtained within 2h, and the decrease of falling follows the order MAX-3 > MAX-1 > MAX-2. The falling signal of ThT fluorescence in the presence of our molecules probably suggests the disintegration of α-synuclein fibrils in the presence of these molecules

To further confirm, we have performed AFM study just after the completion of the above kinetic experiment. The AFM study indicates that these molecules can efficiently disintegrate α-synuclein fibrils into smaller aggregates (Figure 4.11). The raw AFM images were processed using MIPAR™ image processing software in order to extract useful information from the images (Appendix 4.9).

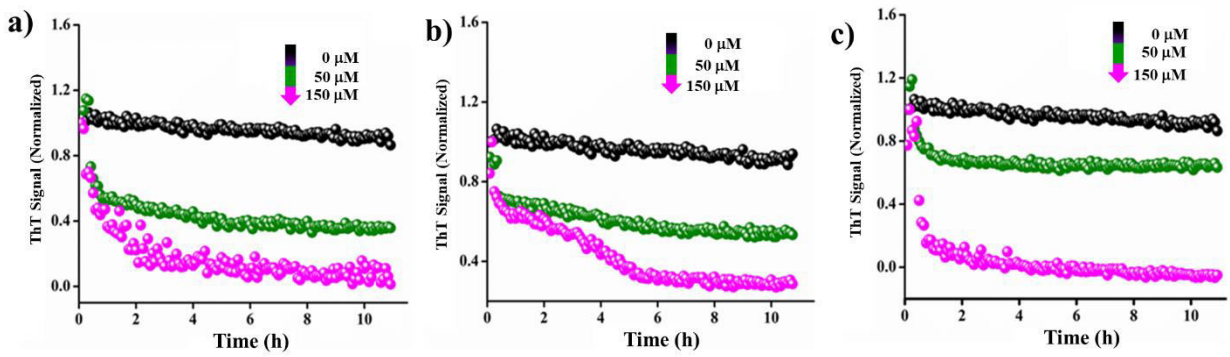

Figure 4.10 a), b), c) Amyloid disintegration kinetics in the presence of MAX-1, MAX-2, and MAX-3.

After processing the original images, we observed a decrease in the mean aspect ratio and eccentricity of the fibrils, indicating that the length of the fibrils is getting shorter in the presence of MAX-1, MAX-2, and MAX-3. Overall, the AFM study confirms that the fibrils got disintegrated in the presence of these molecules.

To inspect the cause behind the disintegration of the fibrils, we performed a circular dichroism study in the absence and presence of MAX-1, MAX-2, and MAX-3 (Figure 4.12a, b, c). The CD signal changes 224 nm to 234 nm, 237 nm, and 235 nm, in the presence of MAX-1, MAX-2, and MAX-3, indicating that these molecules can disturb the conformation of the building block of α-synuclein fibrils, which might be the leading cause of the disintegration of the matured fibrils

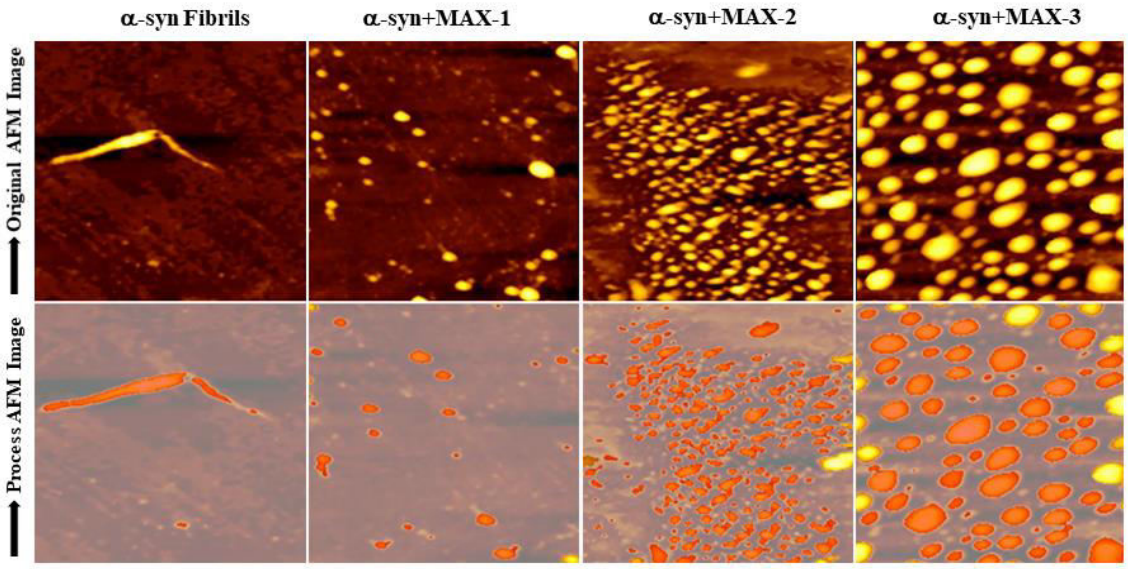

Figure 4.11 Original AFM images of a-synuclein fibrils after 1 day of incubation in the absence and presence of MAX-1, MAX-2, and MAX-3. The lower panel indicates the post-processed images.

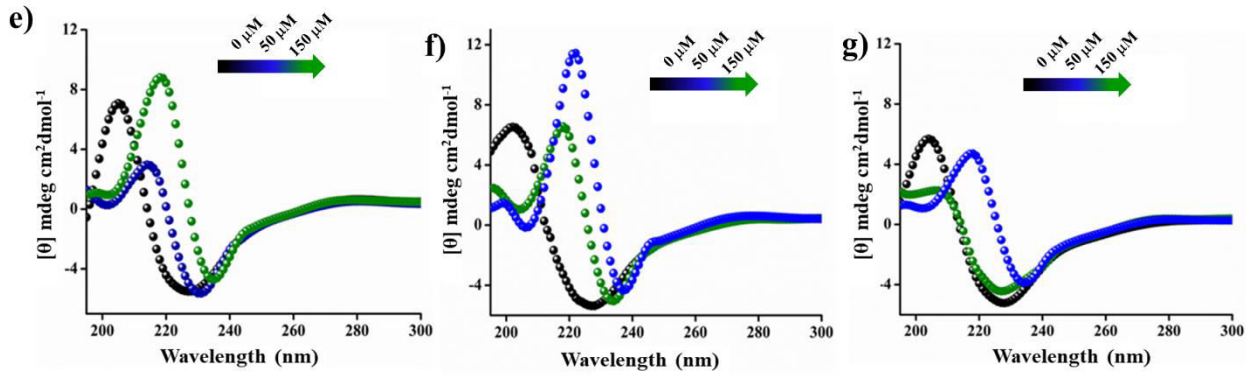

Figure 4.12 a), b), c) Changes in the secondary structure of α-synuclein fibrils monitored using circular dichroism in the absence and presence of MAX-1, MAX-2, and MAX-3, respectively.

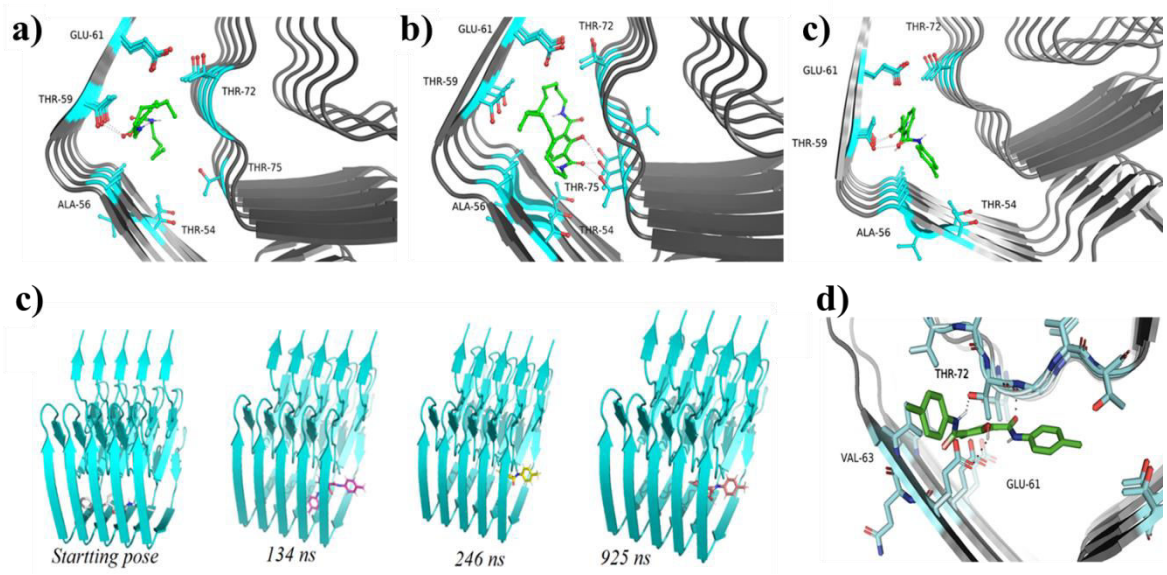

Figure 4.13 a), b), c) Binding mode of MAX-1, MAX-2, and MAX-3 with α-synuclein fibrils d), e), Snapshot images of time-course simulation dynamics of the interaction between MAX-3 side axis view, f) Snapshot images of time-course simulation dynamics of the interaction between MAX-3 view from fibrils axis.

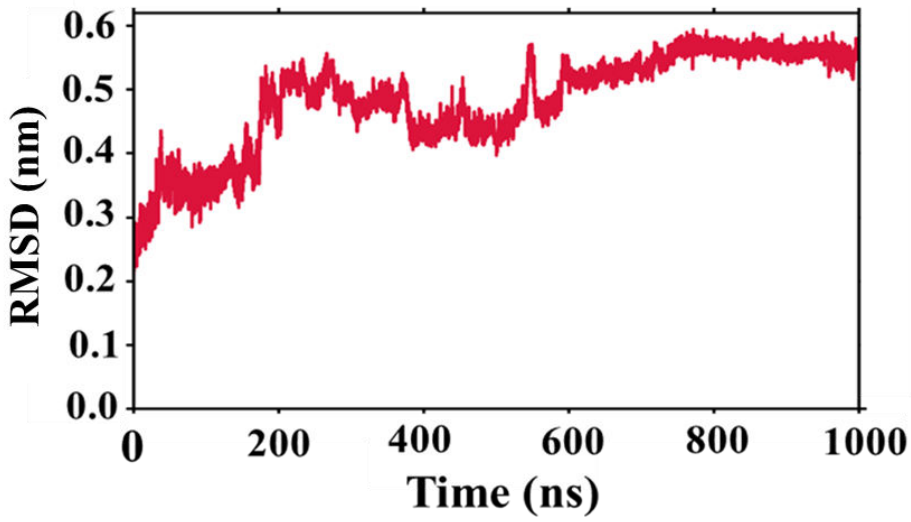

Figure 4.14 Root mean square deviation (RMSD) value of α-syn-MAX-3 complex at 298 K up to 1000 ns of simulation.

4.2.6 Docking and Molecular Dynamic Simulation

To inspect the binding affinity and position of the ligand on the surface of fibrils, molecular docking studies were done using AutoDock vina software[52] with PDB: 6CU7. Blind docking was conducted with box dimensions are as follows: center_x = -1.7108; center_y = 19.0869; center = 12.7178 and size_x = 64.683843441 size_y = 50.7829297304 and size_z = 28.8360336375 (Figure 4. 12a, b, c). Exhaustiveness was set to 8. The binding scores for the ligands MAX-1, MAX-2, and MAX-3, were -5.2 kcal/mol and -5.2 kcal/mol, -7.8 kcal/mol, respectively. Then we performed time-based molecular dynamics (MD) simulation at 1.00 μs using GROMACS[53] on the selected lowest energy MAX-3-complex based on the docking results, to test the durability and overall stability of the docked complexes (Figure 4.12d). Observation from MD simulation results suggest the stable nature of MAX-3-protein complex throughout MD trajectories. The H-bonds resulted in the simulation of molecular dynamics showed that, in most frames, few hydrogen bonds were found between ligand and protein structure. However, the ligand, was found to stabilize in a pose different from the docked pose. The ligand eventually was found to be making stable hydrogen bonds with Glu61, Thr72, and Val63 (Figure 4.12e). Further, we have shown the root mean square deviation (RMSD), which is an important analytical tool for evaluating the stability of α-syn-MAX-3 dock complex during the course of MD simulation. RMSD was calculated by using the trajectory file after equating the least-square fit of backbone atoms of a protein considering the initial structure as a frame of reference by using ‘‘gmx rms’’ tool. The increasing RMSD value of α-syn-MAX-3 complex shown in Figure 4.13 suggests that the structure of α-syn-MAX-3 is getting slightly disturbed. Overall, the docking study indicates that MAX-3 has the highest binding affinity compared to MAX-1 and MAX-2 on the fibrillar surface, which is consistent with our experimental observation, and MD simulation study suggests the stability of the structure of α–syn-MAX-3 complex during the course of the simulation.

4.3 Conclusions

In summary, we have shown a systematic modulation of aggregation kinetics of α-synuclein in the absence and presence of MAX-1, MAX-2, MAX-3 and build up a correlation based on their

promoting ability, which is further confirmed by CD and TEM study. Furthermore, we have estimated a catalytic rate of the primary pathway of aggregation in the presence of MAX-1, MAX-2, and MAX-3 based on their binding affinity with monomeric α-synuclein. Then we have shown that these molecules suppressed the secondary pathway of aggregation upon binding along the fibrils surface of α-synuclein, which eventually stops the surface catalyzed secondary nucleation pathway**.** Moreover, we have demonstrated that these molecules disturbed the conformation of α-synuclein bound on the surface of the lipid membranes, depicted as an *in-vitro* mechanism by which these molecules, significantly reduced the aggregation mediated toxicity of α-synuclein in-cell. Overall, our study depicts the perturbation of a series of molecular events at a microscopic scale involved in α-synuclein aggregation in the presence of MAX-1, MAX-2, and MAX-3. We believe that our results provide detailed insight into the microscopic rates responsible for α-synuclein aggregation, and therefore it will be useful for diagnostics and treatment of PD and similar neurodegenerative disorders.

4.4 Appendix Section

Appendix 4.4.1 Kinetic theory of protein aggregation into amyloid fibrils and its promoter

Based on the distinct chemical characteristics of the drug molecule under contemplation, all or only a subgroup of the various active modes of inhibition briefly described by Michael et al. In the most general scenario, protein aggregation kinetics in the presence of a drug molecule is captured by the following set of coupled differential equations (S1.16 to S1.17). Similarly, in this paper, we are going to illustrate various modes of promotion when a drug-like small molecule is encompassed in the dynamics of aggregation (S1.1 to S1.6).

$$\frac{dP_f(t)}{dt} = k_1 m_f^{n1}(t) + k_2 m_f^{n2}(t) M_f(t) - k_e^{on} C_i(t) P_f(t) + k_e^{off} P_b(t) \qquad \text{S1.1}$$

$$\frac{dM_f(t)}{dt} = 2k_+ m_f(t) P_f(t) - k_s^{on} C_i(t) M_f(t) + k_s^{off} M_b(t) \qquad \text{S1.2}$$

$$\frac{dm_f(t)}{dt} = -2k_+ m_f(t) P_f(t) - k_m^{on} C_i(t) m_f(t) + k_m^{off} m_b(t) \qquad \text{S1.3}$$

$$\frac{dp_b(t)}{dt} = k_e^{on} C_i(t) P_f(t) - k_e^{off} P_b(t) - k_2 P_b(t) \qquad \text{S1.4}$$

$$\frac{dM_b(t)}{dt} = k_s^{on} C_i(t) P_f(t) - k_s^{off} M_b(t) - k_2 M_b(t) \qquad \text{S1.5}$$

$$\frac{dm_b(t)}{dt} = k_m^{on} C_i(t) m_f(t) - k_m^{off} m_b(t) - k_2 m_b(t) \quad \text{S1.6}$$

$$\frac{dC_i(t)}{dt} = -\frac{dP_b(t)}{dt} - \frac{dM_b(t)}{dt} - \frac{dm_b(t)}{dt} \quad \text{S1.7}$$

Where,

$P_f(t), P_b(t)$ = Free/bound aggregates number concentration S1.8

$M_f(t), M_b(t)$ = Free/bound aggregate Mass concentration S1.9

$m_f(t), m_b(t)$ = Free/bound aggregate monomer concentration S1.10

$C_i(t)$ = (Free) inhibitor concentration. S1.11

$$m_{total} = m_f(t) + m_b(t) + M_f(t) + M_b(t) \quad \text{S1.12}$$

Appendix 4.4.2 Total monomer and aggregate concentration-effective kinetic equations

It is necessary to introduce total aggregates number, aggregates mass and monomer concentrations as

$$P(t) = P_f(t) + P_b(t) \quad \text{S1.13}$$

$$M(t) = M_f(t) + M_b(t) \quad \text{S1.14}$$

$$m(t) = m_f(t) + m_b(t) \quad \text{S1.15}$$

Which satisfy the following equations

$$\frac{dP(t)}{dt} = k_1 m_f^{n1}(t) + k_2 m_f^{n2}(t)\, M_f(t) \quad \text{S1.16}$$

$$\frac{dM(t)}{dt} = -2k_+ m_f(t) P_f(t) = -\frac{dm(t)}{dt} \quad \text{S1.17}$$

$$m_f(t) + C_P(t) \underset{k_m^{off}}{\overset{k_m^{on}}{\leftrightharpoons}} m_b(t) \xrightarrow{k_2} P \quad \text{S1.18}$$

$$\frac{dm_b(t)}{dt} = k_m^{on} m_f(t) C_P(t) - k_m^{off} m_b(t) - k_2 m_b(t) \quad \text{S1.19}$$

Using steady state approximation:

$$\frac{dm_b(t)}{dt} \approx 0 \quad \text{S1.20}$$

$$k_m^{on} m_f(t) C_P(t) = k_m^{off} m_b(t) + k_2 m_b(t) \quad \text{S1.21}$$

We know

$$m(t) = m_f(t) + m_b(t) \quad \text{S1.22}$$

$$m_f(t) = m(t) - m_b(t) \quad \text{S1.23}$$

$$k_m^{on}[m(t) - m_b(t)] C_P(t) = k_m^{off} m_b(t) + k_2 m_b(t) \quad \text{S1.24}$$

$$k_m^{on} m(t) C_P(t) = k_m^{on} m_b(t) + k_m^{off} m_b(t) + k_2 m_b(t) \quad \text{S1.25}$$

$$m_b(t) = \frac{k_m^{on} m(t) C_p(t)}{k_m^{on} C_p(t) + k_m^{off} + k_2} \quad \text{S1.26}$$

$$m_b(t) = \frac{k_m^{on} C_p(t)}{k_m^{on} C_p(t) + k_m^{off} + k_2} \quad \text{S1.27}$$

Appendix 4.4.3 Fast promoter binding

Important simplifications unfold in the limit of fast binding of the promoter to monomer and aggregates. In this case, the time variation of bound species can be approximately set equal to zero.

$$\frac{dP_b(t)}{dt} \approx \frac{dM_b(t)}{dt} \approx \frac{dm_b(t)}{dt} \approx 0 \quad \text{S1.28}$$

$$\frac{dC_P(t)}{dt} \approx 0 \quad \text{S1.29}$$

In the case of first binding process

$$k_m^{on} m_f(t) C_P(t) = k_m^{off} m_b(t) + k_2 m_b(t) \quad \text{S1.30}$$

$$m_b(t) = \left(\frac{k_m^{on}}{k_m^{off} + k_2}\right) m_f(t) \quad \text{S1.31}$$

$$\left(\frac{k_m^{on}}{k_m^{off} + k_2}\right) m_f(t) = \frac{k_m^{on} C_p(t)}{k_m^{on} C_p(t) + k_m^{off} + k_2} \quad \text{S1.32}$$

$$m_f(t) = \frac{\left(k_m^{off} + k_2\right) C_p(t)\, m(t)}{(k_m^{on} C_p(t) + k_m^{off} + k_2)} \qquad \text{If} \quad k_2 \gg k_{off} \quad \text{S1.33}$$

$$m_f(t) = \frac{k_2 C_p(t)\, m(t)}{(k_m^{on} C_p(t) + k_m^{off} + k_2)} \quad \text{S1.34}$$

$$P_f(t) + C_P(t) \underset{k_e^{off}}{\overset{k_e^{on}}{\leftrightharpoons}} P_b(t) \xrightarrow{k_2} P \quad \text{S1.35}$$

$$\frac{dP_b(t)}{dt} = k_e^{on} P_f(t) C_P(t) - k_e^{off} P_b(t) - k_2 P_b(t) \quad \text{S1.36}$$

Using steady state approximation

$$\frac{dP_b(t)}{dt} \approx 0 \quad \text{S1.37}$$

$$k_e^{on} P_f(t) C_P(t) = k_e^{off} P_b(t) + k_2 P_b(t) \quad \text{S1.38}$$

$$P(t) = P_f(t) + P_b(t) \quad \text{S1.39}$$

$$P_f(t) = P(t) - P_b(t) \quad \text{S1.40}$$

$$k_e^{on} [P(t) - P_b(t)] C_P(t) = k_e^{off} P_b(t) + k_2 P_b(t) \quad \text{S1.41}$$

$$k_e^{on} P(t) C_P(t) = k_e^{off} P_b(t) + k_2 P_b(t) + k_e^{on} P_b(t) C_P(t) \quad \text{S1.42}$$

$$P_b(t) = \frac{k_e^{on} C_p(t) P(t)}{k_e^{on} C_p(t) + k_m^{off} + k_2} \quad \text{S1.43}$$

In the case for fast binding

$$\frac{dP_b(t)}{dt} \approx 0 \qquad \frac{dC_P(t)}{dt} \approx 0 \quad \text{S1.44}$$

$$k_e^{on} P_f(t) = k_e^{off} P_b(t) + k_2 P_b(t) \quad \text{S1.45}$$

$$P_b(t) = \left(\frac{k_m^{on}}{k_m^{off} + k_2}\right) P_f(t) \quad \text{S1.46}$$

$$\left(\frac{k_e^{on}}{k_e^{off} + k_2}\right) P_f(t) = \frac{k_e^{on} C_p(t) P(t)}{k_e^{on} C_p(t) + k_e^{off} + k_2} \quad \text{S1.47}$$

$$P_f(t) = \frac{(k_e^{off} + k_2) C_p(t) P(t)}{k_e^{on} C_p(t) + k_e^{off} + k_2} \qquad \text{If} \quad k_2 \gg k_{off} \qquad \text{S1.48}$$

$$P_f(t) = \frac{k_2 C_p(t) P(t)}{k_e^{on} C_p(t) + k_e^{off} + k_2} \qquad \text{S1.49}$$

Similarly

$$M_f(t) = \frac{k_2 C_p(t) M(t)}{k_e^{on} C_p(t) + k_e^{off} + k_2} \qquad \text{S1.50}$$

$$\frac{dM(t)}{dt} = 2k_+ \left(\frac{k_2^m C_p(t)\, m(t)}{(k_m^{on} C_p(t) + k_m^{off} + k_2)} \right) \left(\frac{k_2^e C_p(t) P(t)}{k_e^{on} C_p(t) + k_e^{off} + k_2} \right) \qquad \text{S1.51}$$

$$\frac{dP(t)}{dt} = k_1 \left(\frac{k_2^m C_p(t)\, m(t)}{(k_m^{on} C_p(t) + k_m^{off} + k_2)} \right)^{n1} + k_2 \left(\frac{k_2^m C_p(t)\, m(t)}{(k_m^{on} C_p(t) + k_m^{off} + k_2)} \right)^{n2} \frac{k_2^s C_p(t) M(t)}{k_e^{on} C_p(t) + k_e^{off} + k_2} \qquad \text{S1.52}$$

Eq. (S1.51) and Eq. (S1.52) are equivalent to kinetic equations in the absence of promoter, Eq. (S1.16) and (S1.17), but the kinetic parameters are replaced by "effective" rate constant that depend on the promoter concentration.

Where effective combined rate of primary pathway is given by:

$$\frac{(k_n k_+)_{eff}}{k_n k_+} = \left(\frac{k_2^m C_p(t)}{(k_m^{on} C_p(t) + k_m^{off} + k_2)} \right)^{n1+1} \left(\frac{k_2^e C_p(t)}{k_e^{on} C_p(t) + k_e^{off} + k_2} \right) \qquad \text{S1.53}$$

Appendix 4.4.4 Fast binding limit of drug molecule on the surface of the aggregates

In the limit of fast binding of the drug molecule to fibril surfaces, Dobson and co-workers obtained an approximate expression for the roots of the characteristic polynomial using the dominant balance method as follows.

Where the effective combined rate of the secondary pathway is given by:

$$\frac{(k_2 k_+)_{eff}}{k_2 k_+} = \left(\frac{1}{1 + K_s C_i} \right) \qquad \text{S1.54}$$

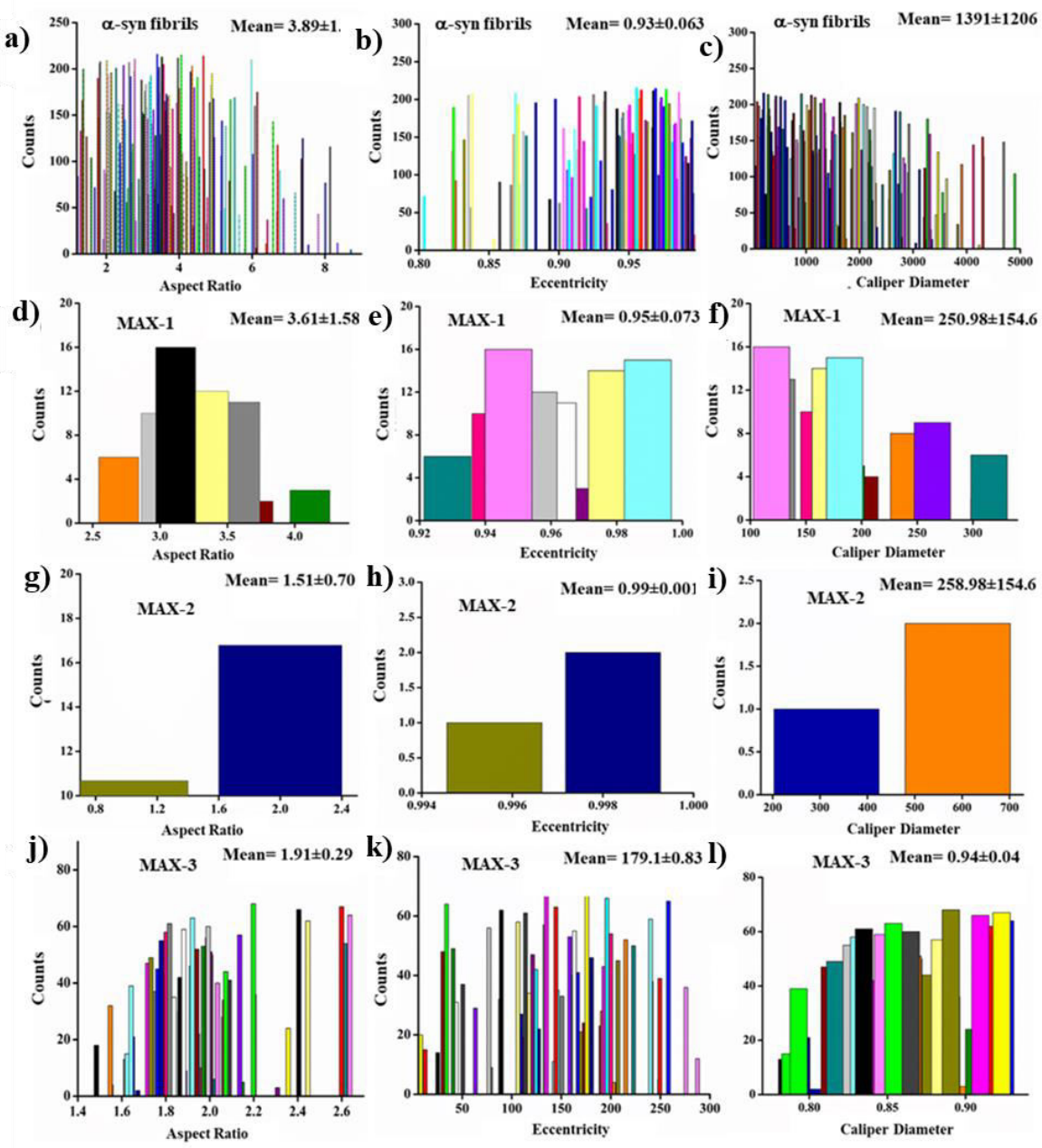

Appendix 4.9 a), b), c) Histogram plot of aspect ratio, caliper diameter and eccentricity of synuclein fibrils. **d to l** Histogram plots of aspect ratio, caliper diameter and eccentricity of α-synuclein fibrils in the presence of MAX-1, MAX-2 and MAX-3.

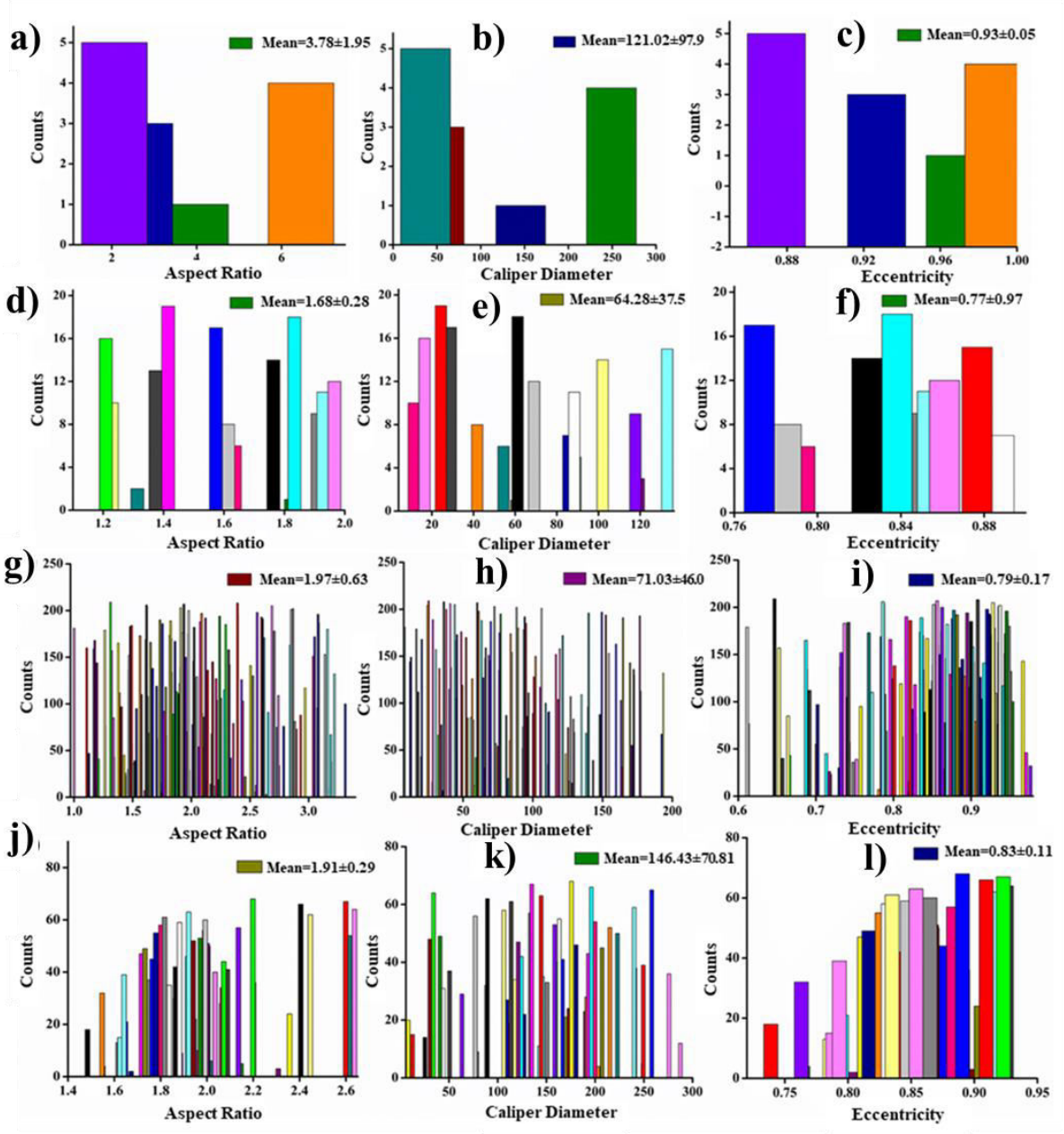

Appendix 4.10 a), b), c) Histogram plot of aspect ratio, caliper diameter and eccentricity of α-synuclein fibrils after 1 day of incubation at 37^0 c. **d to l** Histogram plots of aspect ratio, caliper diameter and eccentricity of α-synuclein fibrils in the presence of MAX-1, MAX-2 and MAX-3 after 1 day of incubation at 37^0 c.

Development of a Systematic Strategy Towards Promotion of Alpha-Synuclein using 2-hydroxy isophthalamide Based System

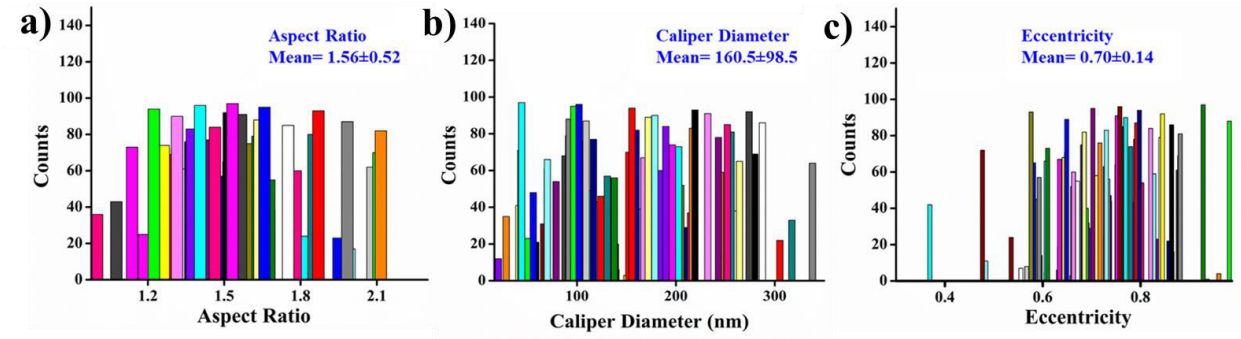

Appendix 4.11 a), b), c) Histogram plot of aspect ratio, caliper diameter and eccentricity of synuclein oligomers.

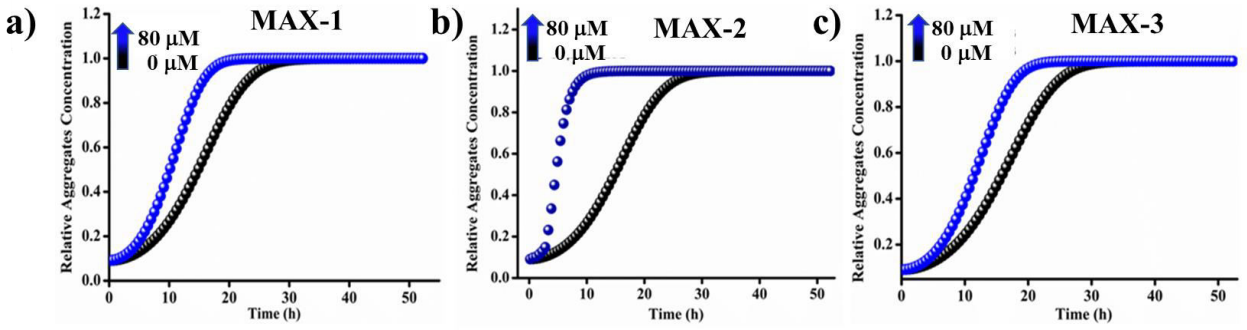

Appendix 4.12 a), b), c) Kinetic profiles of the aggregation of 80 µM a-synuclein with 10% seeds. in the absence or presence, a) 0 and 80 µM MAX-1 b) 0 and 80 µM MAX-2 c) 0 and 80 µM MAX-3.

Appendix Table 1. Analysis of binding constant of MAX-1, MAX-2 and MAX-3 with α-synuclein fibrils surface.

NAME	$K_s\ (M^{-1})$
MAX-1	0.2513 ± 0.073
MAX-2	0.596 ± -0.12
MAX-3	1.561 ± 1.08

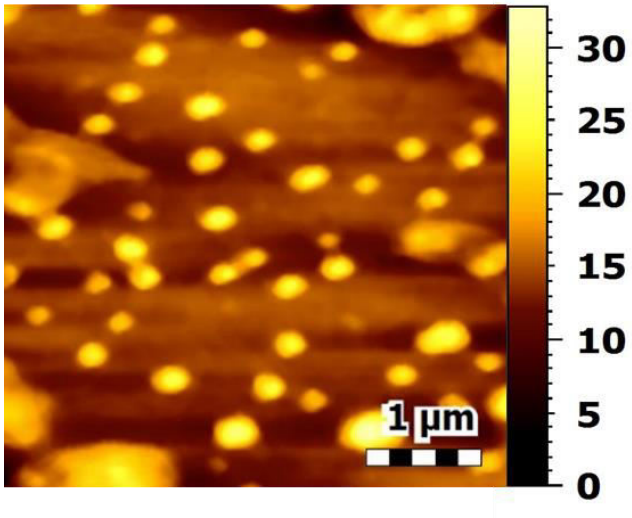

Appendix 4.4.5 AFM data of EYPC Vesicle.

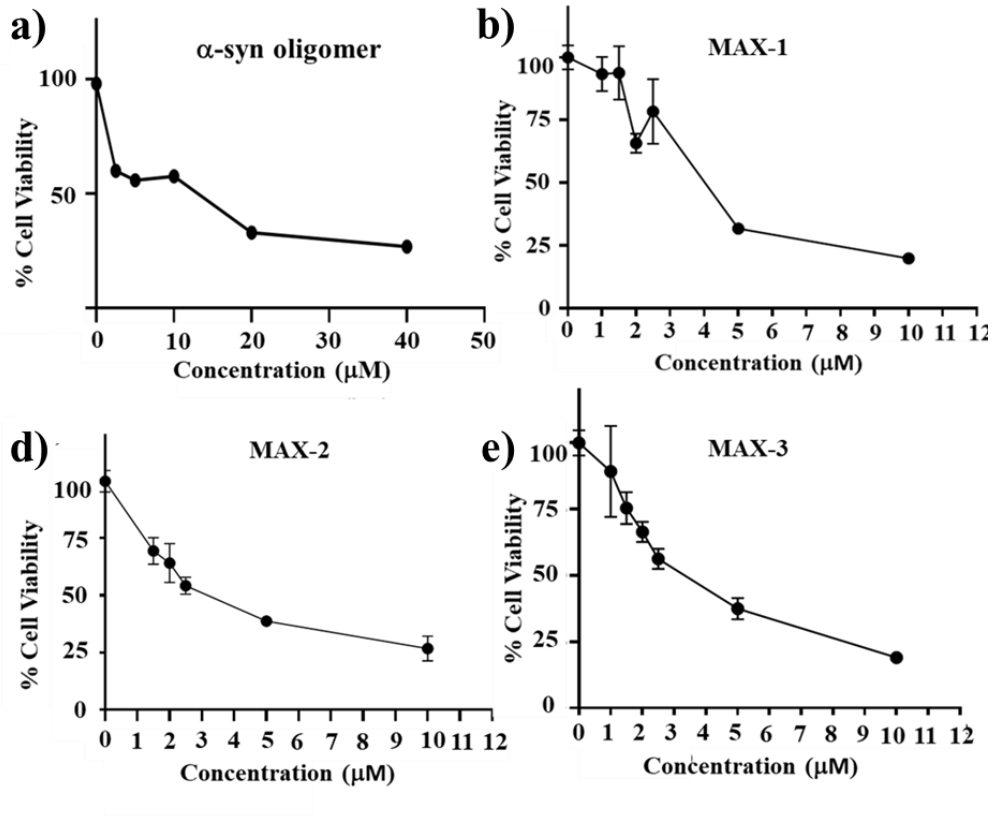

Appendix 4.14 a) Viability of SH-SY5Y cells exposed to different concentrations of α-synuclein oligomer. **b), c), d)** Viability of SH-SY5Y cells in the presence of MAX-1, MAX-2 and MAX-3.

Appendix Table 2. Hydrogen Bonding Interaction with Donor Residue

Donor	Acceptor	Occupancy
TYR39-Side	MAX-3-Side	1.01%
MAX-3-Side	**GLU61**-Side	67.92%
THR59-Side	MAX-3-Side	0.34%
MAX3-Side	THR59-Side	0.01%
MAX3-Side	THR75-Side	0.28%
THR75-Side	MAX3-Side	1.63%
MAX3-Side	THR75-Main	0.61%
MAX3-Side	VAL74-Main	0.86%
THR54-Side	MAX3-Side	1.22%
VAL74-Main	MAX3-Side	0.02%
MAX3-Side	HID50-Main	0.13%
MAX3-Side	VAL52-Main	0.08%
MAX3-Side	GLY51-Main	0.01%
MAX3-Side	THR54-Side	0.04%
GLN62-Side	MAX3-Side	0.01%
MAX3-Side	LYS60-Main	0.23%
GLN62-Main	MAX3-Side	5.50%
THR72-Side	MAX3-Side	0.23%
MAX3-Side	**THR72**-Side	9.45%
GLY73-Main	MAX3-Side	1.65%
LYS58-Side	MAX3-Side	0.40%
LYS60-Side	MAX3-Side	0.01%
MAX3-Side	GLN62-Main	0.05%
MAX3-Side	GLU57-Side	0.02%

Appendix 4.15 MIPAR calculation information: Recipe for image processing

MIPAR calculation is an image processing tool, which is performed in a right order and with the right setting, in order to identify the hiding features inside an image. Below is the elaboration of some typical post-processing steps that we have used in this study to create our required images.

1. Scale calibration: Allows us to calculate the pixel size in units of length rather than pixels.
2. Highlight Lines: Uses the Frangi filter to highlight linear-type features in the image. Combine with a threshold afterwards to select certain linear-type features.
3. Fiber selection: Balance fiber vs. background selection by selecting pixels based on whether they are above or below a certain pixel value. Optimization of selection was performed at this step by selection matching algorithm. It is perhaps the most critical yet less explored area of image processing to quantify the accuracy of the image-processing algorithm in question. MIPAR™ has provided such facility where we can optimize parameter(s) to produce best similarity of the segmentation between the processed and the selected image.

4. Uniform erosion: Shrinks selection, if needed, by a specified number of pixels in all directions.
5. Reject Features: Which can remove or keep features based on a variety of shape and size metrics.
6. Background: Invert fiber selection.

Feature measurements: It allows one to measure a number of feature properties based on the features selected in the image. This includes, size parameters (area, area fraction, caliper diameter, etc.) and shape parameters (roughness, aspect ratio, eccentricity, roundness, etc.)

Few important definitions:

Eccentricity: First an ellipse with same second moments as the feature was fitted. Then eccentricity is calculated as, $\sqrt{\left(1-\left(\frac{minor\ axis\ length}{major\ axis\ length}\right)^2\right)}$. It describes how elongated or circular each feature is. 0 is a perfect circle, 1 is a straight line.

Major axis length: Calculated as, $2\sqrt{2}\left(\sqrt{U_{xx}+U_{yy}+common}\right)$

Minor axis length: Calculated as, $2\sqrt{2}\left(\sqrt{U_{xx}+U_{yy}-common}\right)$

Common = $\sqrt{((U_{xx}-U_{yy})^2+4U_{xy}^2)}$

The second moments are calculated as: $U_{xx} = \frac{Sum(x^2)}{N} + 1/12; \quad U_{yy} = \frac{Sum(y^2)}{N} + 1/12;$

4.5 Experimental Section

4.5.1 Protein Expression and Purification

The protein was expressed and purified as reported earlier with few modifications.[54] *Escherichia coli BL21*(DE3) codon plus (Stratagene) cells transformed with pRK 172 were grown overnight at 37 °C in Luria Bertani broth (LB) medium containing 100 µg/mL ampicillin and then sub cultured into 1000 mL of LB containing 100 µg/mL ampicillin. At an OD600 of 0.8-1.0, the cells were induced by adding 10 µg/mL isopropylthio-β-galactosidase (IPTG) at 25 °C and pelleted down after 5 h. The cells were resuspended in osmotic shock buffer (30 mM tris-HCl, 40 % w/v sucrose, 2 mM EDTA, pH 7.2), incubated at 25 °C for 15 min, and centrifuged to remove supernatant. The pellet was resuspended in Milli-Q water containing 1mM $MgCl_2$, and the supernatant was separated by centrifugation at 4000 RPM. This supernatant was dialyzed twice against 20 mM tris HCl buffer, pH 8.0 at 4 °C. The protein was denatured by adding 8M urea solution loaded onto DEAE FF ion-exchange column (15 mL, Hitrap, GE Healthcare). The loaded protein was washed and then eluted out using gradient of 100-300 mM NaCl. The eluted protein was concentrated by ultrafiltration (Millipore), flash-frozen in liquid N_2, and stored at -80 °C.

4.5.2 ThT (Thioflavin-t) Fluorescence Assay

Assays were initiated by placing the 96-well plate at 37 ℃ under quiescent conditions in a plate reader (Fluoroskan Ascent, Thermo Scientific). The ThT fluorescence was measured through the bottom of the plate using a 440 nm excitation filter and a 480 nm emission filter. The ThT fluorescence was followed for two repeats of each sample.

4.5.3 Calculation of Oligomeric Flux

We have seen that the molecules can affects the aggregation process of α-synuclein to different extent. Using the rate constants ($k_n, k_2,$ or k_+) in the presence of the molecules, we can estimate the reactive flux towards the oligomers ($r(t)$) as[55-57].

$$r(t) = k_n m(t)^2 + k_2 m(t)^2 M(t) \qquad (2)$$

From the plot, we can estimate the generation of oligomer reaches a peak, as well as the total number of oligomers of generated over time. In the presence of the molecules, peak time taken for

oligomer formation speeded up, which consequently promotes the rate of oligomerization. The total number of oligomers formation increases up to a certain concentration of the molecules and then reduce.

4.5.4 Atomic Force Microscopy (AFM)

Atomic Force Microscopy (AFM) imaging was performed on the Keysight 5500 AFM instrument (Agilent Technologies) under tapping mode with a silicon nitride tip. The α-synuclein fibrils in the presence and absence of drug molecules were taken from well after the completion of the aggregation process. The samples were drop casted on the surface of a silicon wafer and dried overnight. The dried samples were washed with water to remove the salt and dried for another 4 h before AFM measurements.

4.5.5 Transmission Electron Microscopy (TEM)

Samples of 8 μM α-synuclein just after finishing aggregation kinetics were adsorb onto glow-discharged 200 mesh carbon film coated copper grids and stained with uranyl acetate (2%). Excess liquid was removed and grids were allowed to dry. The grids prepared in this way were analyzed in JEM2200FS, JEOL (200 keV) transmission electron microscope.

4.5.6 Far-UV Circular Dichroism (CD) Study

CD spectra were recorded on a JASCO-810 circular dichroism spectrometer under a constant flow of nitrogen at 25 °C. Wavelength scans were recorded from 190 nm to 300 nm at 1 nm intervals in a 1 cm path length quartz cuvette. The final spectra were the average of three scans. Background spectra were subtracted from the collected data.

4.5.7 Biolayer Interferometry (BLI)

BLI assays were performed on an Octet Red instrument (forte BIO). The assay was conducted in wells of black polypropylene 96-well microplates. α-Synuclein was immobilized on amine-reactive biosensors (AR2G biosensors) in 10 mM acetate, pH 5.5 buffer, using 1-ethyl-3-(3-dimethylaminopropyl)- carbodiimide (EDC) and N-hydroxy succinimide (NHS).56−58 Binding analysis of MAX-1, MAX-2 and MAX-3 was carried out at 25 °C, 1000 rpm in 10 mM phosphate buffer (pH 7.4) containing 150 mM NaCl, with a 300 s of association followed by a 300 s of dissociation. Sensors were regenerated in NaOH solution. Data were analyzed using Data Analysis (forte BIO), with Savitzky−Golay filtering. Binding was globally fitted to a 1:1 model to obtain the binding kinetic constant (K_D).

References

1. Hamza, T. H.; Chen, H.; Hill-Burns, E. M.; Rhodes, S. L.; Montimurro, J.; Kay, D. M.; Tenesa, A.; Kusel, V. I.; Sheehan, P.; Eaaswarkhanth, M.; Yearout, D.; Samii, A.; Roberts, J. W.; Agarwal, P.; Bordelon, Y.; Park, Y.; Wang, L.; Gao, J.; Vance, J. M.; Kendler, K. S.; Bacanu, S.-A.; Scott, W. K.; Ritz, B.; Nutt, J.; Factor, S. A.; Zabetian, C. P.; Payami, H., Genome-wide gene-environment study identifies glutamate receptor gene GRIN2A as a Parkinson's disease modifier gene via interaction with coffee. *PLoS genetics* **2011,** *7* (8), e1002237-e1002237.

2. Lebouvier, T.; Chaumette, T.; Paillusson, S.; Duyckaerts, C.; Bruley des Varannes, S.; Neunlist, M.; Derkinderen, P., The second brain and Parkinson's disease. *European Journal of Neuroscience* **2009,** *30* (5), 735-741.

3. Błaszczyk, J. W., Parkinson's Disease and Neurodegeneration: GABA-Collapse Hypothesis. *Front Neurosci* **2016,** *10*.

4. Aarsland, D.; Batzu, L.; Halliday, G. M.; Geurtsen, G. J.; Ballard, C.; Ray Chaudhuri, K.; Weintraub, D., Parkinson disease-associated cognitive impairment. *Nature Reviews Disease Primers* **2021,** *7* (1), 47.

5. Pujols, J.; Peña-Díaz, S.; Lázaro, D. F.; Peccati, F.; Pinheiro, F.; González, D.; Carija, A.; Navarro, S.; Conde-Giménez, M.; García, J.; Guardiola, S.; Giralt, E.; Salvatella, X.; Sancho, J.; Sodupe, M.; Outeiro, T. F.; Dalfó, E.; Ventura, S., Small molecule inhibits α-synuclein aggregation, disrupts amyloid fibrils, and prevents degeneration of dopaminergic neurons. *Proc Natl Acad Sci U S A* **2018,** *115* (41), 10481-10486.

6. Mamelak, M., Parkinson's Disease, the Dopaminergic Neuron and Gammahydroxybutyrate. *Neurology and Therapy* **2018,** *7*.

7. Klein, C.; Westenberger, A., Genetics of Parkinson's Disease. *Cold Spring Harbor perspectives in medicine* **2012,** *2*, a008888.

8. Semchuk, K. M.; Love, E. J.; Lee, R. G., Parkinson's disease. *Neurology* **1993,** *43* (6), 1173.

9. Iarkov, A.; Barreto, G. E.; Grizzell, J. A.; Echeverria, V., Strategies for the Treatment of Parkinson's Disease: Beyond Dopamine. *Frontiers in Aging Neuroscience* **2020,** *12*.

10. Pang, S. Y.-Y.; Ho, P. W.-L.; Liu, H.-F.; Leung, C.-T.; Li, L.; Chang, E. E. S.; Ramsden, D. B.; Ho, S.-L., The interplay of aging, genetics and environmental factors in the pathogenesis of Parkinson's disease. *Translational Neurodegeneration* **2019,** *8* (1), 23.

11. Rocca, W. A., The burden of Parkinson's disease: a worldwide perspective. *The Lancet Neurology* **2018,** *17* (11), 928-929.

12. Dorsey, E. R.; Elbaz, A.; Nichols, E.; Abbasi, N.; Abd-Allah, F.; Abdelalim, A.; Adsuar, J. C.; Ansha, M. G.; Brayne, C.; Choi, J.-Y. J.; Collado-Mateo, D.; Dahodwala, N.; Do, H. P.; Edessa, D.; Endres, M.; Fereshtehnejad, S.-M.; Foreman, K. J.; Gankpe, F. G.; Gupta, R.; Hamidi, S.; Hankey, G. J.; Hay, S. I.; Hegazy, M. I.; Hibstu, D. T.; Kasaeian, A.; Khader, Y.; Khalil, I.; Khang, Y.-H.; Kim, Y. J.; Kokubo, Y.; Logroscino, G.; Massano, J.; Mohamed Ibrahim, N.; Mohammed, M. A.; Mohammadi, A.; Moradi-Lakeh, M.; Naghavi, M.; Nguyen, B. T.; Nirayo, Y. L.; Ogbo, F. A.; Owolabi, M. O.; Pereira, D. M.; Postma, M. J.; Qorbani, M.; Rahman, M. A.; Roba, K. T.; Safari, H.; Safiri, S.; Satpathy, M.; Sawhney, M.; Shafieesabet, A.; Shiferaw, M. S.; Smith, M.; Szoeke, C. E. I.; Tabarés-Seisdedos, R.; Truong, N. T.; Ukwaja, K. N.; Venketasubramanian, N.; Villafaina, S.; weldegwergs, K. g.; Westerman, R.; Wijeratne, T.; Winkler, A. S.; Xuan, B. T.; Yonemoto, N.; Feigin, V. L.; Vos, T.; Murray, C. J. L., Global, regional, and national burden of Parkinson's disease, 1990–2016: a systematic analysis for the Global Burden of Disease Study 2016. *The Lancet Neurology* **2018,** *17* (11), 939-953.

13. Armstrong, M. J.; Okun, M. S., Time for a New Image of Parkinson Disease. *JAMA Neurology* **2020,** *77* (11), 1345-1346.

14. Nilashi, M.; Ibrahim, O.; Ahani, A., Accuracy Improvement for Predicting Parkinson's Disease Progression. *Scientific Reports* **2016,** *6* (1), 34181.

15. Maries, E.; Dass, B.; Collier, T. J.; Kordower, J. H.; Steece-Collier, K., The role of α-synuclein in Parkinson's disease: insights from animal models. *Nature Reviews Neuroscience* **2003,** *4* (9), 727-738.

16. Ahmadi Rastegar, D.; Ho, N.; Halliday, G. M.; Dzamko, N., Parkinson's progression prediction using machine learning and serum cytokines. *npj Parkinson's Disease* **2019,** *5* (1), 14.

17. Meade, R. M.; Fairlie, D. P.; Mason, J. M., Alpha-synuclein structure and Parkinson's disease – lessons and emerging principles. *Molecular Neurodegeneration* **2019,** *14* (1), 29.

18. Sulzer, D.; Edwards, R. H., The physiological role of α-synuclein and its relationship to Parkinson's Disease. *Journal of Neurochemistry* **2019,** *150* (5), 475-486.

19. Perni, M.; van der Goot, A.; Limbocker, R.; van Ham, T. J.; Aprile, F. A.; Xu, C. K.; Flagmeier, P.; Thijssen, K.; Sormanni, P.; Fusco, G.; Chen, S. W.; Challa, P. K.; Kirkegaard, J. B.; Laine, R. F.; Ma, K. Y.; Müller, M. B. D.; Sinnige, T.; Kumita, J. R.; Cohen, S. I. A.; Seinstra, R.; Kaminski Schierle, G. S.; Kaminski, C. F.; Barbut, D.; De Simone, A.; Knowles, T. P. J.; Zasloff, M.; Nollen, E. A. A.; Vendruscolo, M.; Dobson, C. M., Comparative Studies in the A30P and A53T α-Synuclein C. elegans Strains to Investigate the Molecular Origins of Parkinson's Disease. *Frontiers in Cell and Developmental Biology* **2021,** *9*.

20. Sacino, A. N.; Brooks, M.; McKinney, A. B.; Thomas, M. A.; Shaw, G.; Golde, T. E.; Giasson, B. I., Brain injection of α-synuclein induces multiple proteinopathies, gliosis, and a neuronal injury marker. *J Neurosci* **2014,** *34* (37), 12368-12378.

21. Stefanis, L., α-Synuclein in Parkinson's disease. *Cold Spring Harbor perspectives in medicine* **2012,** *2* (2), a009399-a009399.

22. Limbocker, R.; Mannini, B.; Ruggeri, F. S.; Cascella, R.; Xu, C. K.; Perni, M.; Chia, S.; Chen, S. W.; Habchi, J.; Bigi, A.; Kreiser, R. P.; Wright, A. K.; Albright, J. A.; Kartanas, T.; Kumita, J. R.; Cremades, N.; Zasloff, M.; Cecchi, C.; Knowles, T. P. J.; Chiti, F.; Vendruscolo, M.; Dobson, C. M., Trodusquemine displaces protein misfolded oligomers from cell membranes and abrogates their cytotoxicity through a generic mechanism. *Communications Biology* **2020,** *3* (1), 435.

23. Perni, M.; Flagmeier, P.; Limbocker, R.; Cascella, R.; Aprile, F. A.; Galvagnion, C.; Heller, G. T.; Meisl, G.; Chen, S. W.; Kumita, J. R.; Challa, P. K.; Kirkegaard, J. B.; Cohen, S. I. A.; Mannini, B.; Barbut, D.; Nollen, E. A. A.; Cecchi, C.; Cremades, N.; Knowles, T. P. J.; Chiti, F.; Zasloff, M.; Vendruscolo, M.; Dobson, C. M., Multistep Inhibition of α-Synuclein Aggregation and Toxicity in Vitro and in Vivo by Trodusquemine. *ACS Chemical Biology* **2018,** *13* (8), 2308-2319.

24. Perni, M.; Galvagnion, C.; Maltsev, A.; Meisl, G.; Müller Martin, B. D.; Challa Pavan, K.; Kirkegaard Julius, B.; Flagmeier, P.; Cohen Samuel, I. A.; Cascella, R.; Chen Serene, W.; Limbocker, R.; Sormanni, P.; Heller Gabriella, T.; Aprile Francesco, A.; Cremades, N.; Cecchi, C.; Chiti, F.; Nollen Ellen, A. A.; Knowles Tuomas, P. J.; Vendruscolo, M.; Bax, A.; Zasloff, M.; Dobson Christopher, M., A natural product inhibits the initiation of α-synuclein aggregation and suppresses its toxicity. *Proceedings of the National Academy of Sciences* **2017,** *114* (6), E1009-E1017.

25. Pujols, J.; Peña-Díaz, S.; Lázaro Diana, F.; Peccati, F.; Pinheiro, F.; González, D.; Carija, A.; Navarro, S.; Conde-Giménez, M.; García, J.; Guardiola, S.; Giralt, E.; Salvatella, X.; Sancho, J.; Sodupe, M.; Outeiro Tiago, F.; Dalfó, E.; Ventura, S., Small molecule inhibits α-synuclein aggregation, disrupts amyloid fibrils, and prevents degeneration of dopaminergic neurons. *Proceedings of the National Academy of Sciences* **2018,** *115* (41), 10481-10486.

26. Meisl, G.; Kirkegaard, J. B.; Arosio, P.; Michaels, T. C. T.; Vendruscolo, M.; Dobson, C. M.; Linse, S.; Knowles, T. P. J., Molecular mechanisms of protein aggregation from global fitting of kinetic models. *Nature Protocols* **2016,** *11* (2), 252-272.

27. Meisl, G.; Yang, X.; Hellstrand, E.; Frohm, B.; Kirkegaard Julius, B.; Cohen Samuel, I. A.; Dobson Christopher, M.; Linse, S.; Knowles Tuomas, P. J., Differences in nucleation behavior underlie the contrasting aggregation kinetics of the Aβ40 and Aβ42 peptides. *Proceedings of the National Academy of Sciences* **2014,** *111* (26), 9384-9389.

28. Cohen, S. I. A.; Vendruscolo, M.; Welland, M. E.; Dobson, C. M.; Terentjev, E. M.; Knowles, T. P. J., Nucleated polymerization with secondary pathways. I. Time evolution of the principal moments. *J Chem Phys* **2011,** *135* (6), 065105.

29. Cohen, S. I. A.; Vendruscolo, M.; Dobson, C. M.; Knowles, T. P. J., Nucleated polymerization with secondary pathways. II. Determination of self-consistent solutions to growth processes described by non-linear master equations. *J Chem Phys* **2011,** *135* (6), 065106-065106.

30. Arosio, P.; Vendruscolo, M.; Dobson, C. M.; Knowles, T. P. J., Chemical kinetics for drug discovery to combat protein aggregation diseases. *Trends in Pharmacological Sciences* **2014,** *35* (3), 127-135.

31. Michaels Thomas, C. T.; Šarić, A.; Meisl, G.; Heller Gabriella, T.; Curk, S.; Arosio, P.; Linse, S.; Dobson Christopher, M.; Vendruscolo, M.; Knowles Tuomas, P. J., Thermodynamic and kinetic design principles for amyloid-aggregation inhibitors. *Proceedings of the National Academy of Sciences* **2020,** *117* (39), 24251-24257.

32. Michaels, T. C. T.; Šarić, A.; Habchi, J.; Chia, S.; Meisl, G.; Vendruscolo, M.; Dobson, C. M.; Knowles, T. P. J., Chemical Kinetics for Bridging Molecular Mechanisms and Macroscopic Measurements of Amyloid Fibril Formation. *Annual review of physical chemistry* **2018,** *69* (1), 273-298.

33. Langman, R. E., Protein Structure and Evolution. J. Lawrence Fox , Zdeněk Deyl , Anton Blažej. *The Quarterly Review of Biology* **1977,** *52* (4), 398-399.

34. Cohen Samuel, I. A.; Linse, S.; Luheshi Leila, M.; Hellstrand, E.; White Duncan, A.; Rajah, L.; Otzen Daniel, E.; Vendruscolo, M.; Dobson Christopher, M.; Knowles Tuomas, P. J., Proliferation of amyloid-β42 aggregates occurs through a secondary nucleation mechanism. *Proceedings of the National Academy of Sciences* **2013,** *110* (24), 9758-9763.

35. Arosio, P.; Michaels, T. C. T.; Linse, S.; Månsson, C.; Emanuelsson, C.; Presto, J.; Johansson, J.; Vendruscolo, M.; Dobson, C. M.; Knowles, T. P. J., Kinetic analysis reveals the diversity of microscopic mechanisms through which molecular chaperones suppress amyloid formation. *Nature Communications* **2016,** *7* (1), 10948.

36. Habchi, J.; Arosio, P.; Perni, M.; Costa Ana, R.; Yagi-Utsumi, M.; Joshi, P.; Chia, S.; Cohen Samuel, I. A.; Müller Martin, B. D.; Linse, S.; Nollen Ellen, A. A.; Dobson Christopher, M.; Knowles Tuomas, P. J.; Vendruscolo, M., An anticancer drug suppresses the primary nucleation reaction that initiates the production of the toxic Aβ42 aggregates linked with Alzheimer's disease. *Science Advances 2* (2), e1501244.

37. Chia, S.; Flagmeier, P.; Habchi, J.; Lattanzi, V.; Linse, S.; Dobson Christopher, M.; Knowles Tuomas, P. J.; Vendruscolo, M., Monomeric and fibrillar α-synuclein exert opposite effects on the catalytic cycle that promotes the proliferation of Aβ42 aggregates. *Proceedings of the National Academy of Sciences* **2017,** *114* (30), 8005-8010.

38. Limbocker, R.; Chia, S.; Ruggeri, F. S.; Perni, M.; Cascella, R.; Heller, G. T.; Meisl, G.; Mannini, B.; Habchi, J.; Michaels, T. C. T.; Challa, P. K.; Ahn, M.; Casford, S. T.; Fernando, N.; Xu, C. K.; Kloss, N. D.; Cohen, S. I. A.; Kumita, J. R.; Cecchi, C.; Zasloff, M.; Linse, S.; Knowles, T. P. J.; Chiti, F.; Vendruscolo, M.; Dobson, C. M., Trodusquemine enhances Aβ42 aggregation but suppresses its toxicity by displacing oligomers from cell membranes. *Nature Communications* **2019,** *10* (1), 225.

39. Scheidt, T.; Łapińska, U.; Kumita Janet, R.; Whiten Daniel, R.; Klenerman, D.; Wilson Mark, R.; Cohen Samuel, I. A.; Linse, S.; Vendruscolo, M.; Dobson Christopher, M.; Knowles Tuomas, P. J.; Arosio, P., Secondary nucleation and elongation occur at different sites on Alzheimer's amyloid-β aggregates. *Science Advances 5* (4), eaau3112.

40. Heller Gabriella, T.; Aprile Francesco, A.; Michaels Thomas, C. T.; Limbocker, R.; Perni, M.; Ruggeri Francesco, S.; Mannini, B.; Löhr, T.; Bonomi, M.; Camilloni, C.; De Simone, A.; Felli Isabella, C.; Pierattelli, R.; Knowles Tuomas, P. J.; Dobson Christopher, M.; Vendruscolo, M.,

Small-molecule sequestration of amyloid-β as a drug discovery strategy for Alzheimer's disease. *Science Advances 6* (45), eabb5924.

41. Habchi, J.; Chia, S.; Limbocker, R.; Mannini, B.; Ahn, M.; Perni, M.; Hansson, O.; Arosio, P.; Kumita Janet, R.; Challa Pavan, K.; Cohen Samuel, I. A.; Linse, S.; Dobson Christopher, M.; Knowles Tuomas, P. J.; Vendruscolo, M., Systematic development of small molecules to inhibit specific microscopic steps of Aβ42 aggregation in Alzheimer's disease. *Proceedings of the National Academy of Sciences* **2017,** *114* (2), E200-E208.

42. Malla, J. A.; Umesh, R. M.; Yousf, S.; Mane, S.; Sharma, S.; Lahiri, M.; Talukdar, P., A Glutathione Activatable Ion Channel Induces Apoptosis in Cancer Cells by Depleting Intracellular Glutathione Levels. *Angewandte Chemie International Edition* **2020,** *59* (20), 7944-7952.

43. Malla, J. A.; Umesh, R. M.; Vijay, A.; Mukherjee, A.; Lahiri, M.; Talukdar, P., Apoptosis-inducing activity of a fluorescent barrel-rosette M+/Cl− channel. *Chemical Science* **2020,** *11* (9), 2420-2428.

44. Oosawa, F., *Thermodynamics of the polymerization of protein / Fumio Oosawa and Sho Asakura*. Academic Press: London ; New York, 1975.

45. Cohen, S. I. A.; Vendruscolo, M.; Welland, M. E.; Dobson, C. M.; Terentjev, E. M.; Knowles, T. P. J., Nucleated polymerization with secondary pathways. I. Time evolution of the principal moments. *J Chem Phys* **2011,** *135* (6), 065105-065105.

46. Habchi, J.; Chia, S.; Galvagnion, C.; Michaels, T. C. T.; Bellaiche, M. M. J.; Ruggeri, F. S.; Sanguanini, M.; Idini, I.; Kumita, J. R.; Sparr, E.; Linse, S.; Dobson, C. M.; Knowles, T. P. J.; Vendruscolo, M., Cholesterol catalyses Aβ42 aggregation through a heterogeneous nucleation pathway in the presence of lipid membranes. *Nature Chemistry* **2018,** *10* (6), 673-683.

47. Musteikytė, G.; Jayaram, A. K.; Xu, C. K.; Vendruscolo, M.; Krainer, G.; Knowles, T. P. J., Interactions of α-synuclein oligomers with lipid membranes. *Biochimica et Biophysica Acta (BBA) - Biomembranes* **2021,** *1863* (4), 183536.

48. Fusco, G.; Chen Serene, W.; Williamson Philip, T. F.; Cascella, R.; Perni, M.; Jarvis James, A.; Cecchi, C.; Vendruscolo, M.; Chiti, F.; Cremades, N.; Ying, L.; Dobson Christopher, M.; De Simone, A., Structural basis of membrane disruption and cellular toxicity by α-synuclein oligomers. *Science* **2017,** *358* (6369), 1440-1443.

49. Du, X.-y.; Xie, X.-x.; Liu, R.-t., The Role of α-Synuclein Oligomers in Parkinson's Disease. *International Journal of Molecular Sciences* **2020,** *21* (22).

50. Winner, B.; Jappelli, R.; Maji Samir, K.; Desplats Paula, A.; Boyer, L.; Aigner, S.; Hetzer, C.; Loher, T.; Vilar, M.; Campioni, S.; Tzitzilonis, C.; Soragni, A.; Jessberger, S.; Mira, H.; Consiglio, A.; Pham, E.; Masliah, E.; Gage Fred, H.; Riek, R., In vivo demonstration that α-synuclein oligomers are toxic. *Proceedings of the National Academy of Sciences* **2011,** *108* (10), 4194-4199.

51. van Rooijen, B. D.; Claessens, M. M. A. E.; Subramaniam, V., Lipid bilayer disruption by oligomeric α-synuclein depends on bilayer charge and accessibility of the hydrophobic core. *Biochimica et Biophysica Acta (BBA) - Biomembranes* **2009,** *1788* (6), 1271-1278.

52. Forli, S.; Huey, R.; Pique, M. E.; Sanner, M. F.; Goodsell, D. S.; Olson, A. J., Computational protein–ligand docking and virtual drug screening with the AutoDock suite. *Nature Protocols* **2016,** *11* (5), 905-919.

53. Lemkul, J. A., From Proteins to Perturbed Hamiltonians: A Suite of Tutorials for the GROMACS-2018 Molecular Simulation Package [Article v1.0]. *Living Journal of Computational Molecular Science* **2018,** *1* (1), 5068.

54. Huang, C.; Ren, G.; Zhou, H.; Wang, C.-c., A new method for purification of recombinant human α-synuclein in Escherichia coli. *Protein Expression and Purification* **2005,** *42* (1), 173-177.

55. Chia, S.; Habchi, J.; Michaels Thomas, C. T.; Cohen Samuel, I. A.; Linse, S.; Dobson Christopher, M.; Knowles Tuomas, P. J.; Vendruscolo, M., SAR by kinetics for drug discovery in protein misfolding diseases. *Proceedings of the National Academy of Sciences* **2018,** *115* (41), 10245-10250.

56. Cohen, S. I. A.; Arosio, P.; Presto, J.; Kurudenkandy, F. R.; Biverstål, H.; Dolfe, L.; Dunning, C.; Yang, X.; Frohm, B.; Vendruscolo, M.; Johansson, J.; Dobson, C. M.; Fisahn, A.; Knowles, T. P. J.; Linse, S., A molecular chaperone breaks the catalytic cycle that generates toxic Aβ oligomers. *Nature Structural & Molecular Biology* **2015,** *22* (3), 207-213.

57. Michaels, T. C. T.; Lazell, H. W.; Arosio, P.; Knowles, T. P. J., Dynamics of protein aggregation and oligomer formation governed by secondary nucleation. *J Chem Phys* **2015,** *143* (5), 054901.

Development of a Systematic Strategy Towards Promotion of Alpha-Synuclein using 2-hydroxy isophthalamide Based System